SuperDARN Electrostatic Potential Function Estimation of Field-Aligned Currents

A Thesis Submitted to the

College of Graduate and Postdoctoral Studies

in Partial Fulfillment of the Requirements

for the Degree of Master of Science

in the Department of Physics and Engineering Physics

University of Saskatchewan

Saskatoon

By

Matthew Richard Wessel

PERMISSION TO USE

In presenting this thesis in partial fulfilment of the requirements for a Postgraduate degree from the University of Saskatchewan, I agree that the Libraries of this University may make it freely available for inspection. I further agree that permission for copying of this thesis in any manner, in whole or in part, for scholarly purposes may be granted by the professors who supervised my thesis work or, in their absence, by the Head of the Department or the Dean of the College in which my thesis work was done. It is understood that any copying or publication or use of this thesis or parts thereof for financial gain shall not be allowed without my written permission. It is also understood that due recognition shall be given to me and to the University of Saskatchewan in any scholarly use which may be made of any material in my thesis.

Requests for permission to copy or to make other use of material in this thesis in whole or part should be addressed to:

Head of the Department of Physics and Engineering Physics
116 Science Place, Rm 163
University of Saskatchewan
Saskatoon, SK S7N 5E2
CANADA

ABSTRACT

Magnetic field-aligned currents (FACs) flow between the Earth's ionosphere and magnetosphere. The connection afforded by FACs means that magnetospheric dynamics may be discerned in ground-based observations of the ionosphere, observations such as the ionospheric plasma velocity measurements made by the Super Dual Auroral Radar Network (SuperDARN). Signatures of FACs are present in the radar data as vorticity in the ionospheric plasma flow.

In this thesis, a new method of estimating FACs on a hemispheric scale from ground-based radar observations is presented. The method produces maps of estimated FAC density divided by height-integrated ionospheric Pedersen conductivity through direct calculation from electrostatic potential (voltage) functions that are generated from SuperDARN plasma velocity measurements. Comparisons of the maps to FAC estimates obtained from ground- and satellite-based observations using established methods show good qualitative agreement. A short case study of a geomagnetic event that occurred between the evening of 31 May 2013 and the morning of 1 June 2013 is presented to demonstrate the utility of the new potential function-based method. Future applications of the new method are suggested, such as to multi-instrument studies including SuperDARN. The new method is especially useful in that it is easily automated, easily adaptable to new SuperDARN data analysis software, and provides hemisphere-scale FAC maps with the one- or two-minute cadence of the underlying SuperDARN potential functions.

ACKNOWLEDGEMENTS

This thesis would not have been finished without the help of a lot of people over a lot of years. My supervisors George Sofko and Kathryn McWilliams went above and beyond their responsibilities to instruct, guide, proofread, and encourage. (I have the distinction of being George's last graduate student. Probably.) The same could be said of much of the rest of the faculty at the Institute of Space and Atmospheric Studies. I shared offices and good discussions with many fellow graduate students, of whom Ashton Reimer and Gareth Perry deserve special mention and thanks. Lindis Bjoland, Xiangcai Chen, Yaqi Jin, Ashton, Åsmund Skjæveland, and our advisors Johnathan Burchill, Lasse Clausen, Stein Haaland, and Kathryn were the group at Kananaskis who gave me the opportunity both to be published and to share a lot of learning (and a lot of coffee). Dwain Stensrud, Terry Rohrke, Ron Osterried, and Denis Sirois, my project leads and project managers at SED Systems, kindly allowed me to take time off to finish this thesis in the midst of busy work schedules, without which help there could not have been enough time. The Natural Sciences and Engineering Research Council and the University of Saskatchewan helped fund this grand adventure. (*Deo et Patriæ!*) My parents Les and Donna have been a constant source of love and support from my earliest days and all through this thesis. My God gave me strength and endurance to finish this race, and this world of His to explore. Finally, I cannot thank enough my gentle, patient wife Christa, who first met me not long after I started this master's program but, for some reason, still decided to marry me. Despite being neck-deep in her own second degree, she has always found time to build me up when I thought I couldn't finish this project. To her I owe everything.

To Christa

CONTENTS

LIST OF TABLES

LIST OF FIGURES

LIST OF ABBREVIATIONS

AACGM	Altitude-Adjusted Corrected GeoMagnetic (coordinate system)
ACE	Advanced Composition Explorer
ACF	AutoCorrelation Function
AMPERE	Active Magnetosphere and Planetary Electrodynamics Response Experiment
AU	Astronomical Unit (1.5×10^8 km)
DMSP	Defense Meteorological Satellite Program
FAC	Field-Aligned Current
GSFC	Goddard Space Flight Center
GSM	Geocentric Solar Magnetospheric (coordinate system)
HF	High Frequency
HMB	Heppner–Maynard Boundary
IMF	Interplanetary Magnetic Field
Kp	*planetarische Kennziffer*, Planetary Index
l-o-s	Line-of-Sight
MLAT	Magnetic invariant LATitude
MLT	Magnetic Local Time
NASA	(United States) National Aeronautics and Space Administration
OCFLB	Open–Closed Field Line Boundary
PolarDARN	Polar Dual Auroral Radar Network
RADAR, radar	RAdio Detection And Ranging
RST	Radar Software Toolkit
SuperDARN	Super Dual Auroral Radar Network
SYM-H	SYMmetric disturbance—Horizontal
UT	Universal Time

CHAPTER 1

INTRODUCTION

The Sun's influence on the Earth is not limited to gravity and sunlight. The solar atmosphere expands at supersonic speed [*Parker*, 1958], a fluid that flows around the obstacles in its path. In the case of a magnetised planet such as Earth, the obstacle presented is the planetary magnetosphere, which is significantly larger than the planet itself [*Dungey*, 1961].

The expanding solar atmosphere, or solar wind, carries the Sun's magnetic field with it as the interplanetary magnetic field (IMF), so the interaction of the IMF and the Earth's geomagnetic field is governed as much by Maxwell's equations of electromagnetism as by the laws of fluid dynamics. The geomagnetic field resists the pressure of the onrushing solar wind flow, forming a cavity called the magnetosphere in the solar wind. The Earth and its magnetosphere are shown in Figure 1.1 from *Russell* [1995]. The solar wind transfers energy and momentum into the magnetosphere both through viscous fluid processes and, more importantly for this thesis, magnetic reconnection [*Hughes*, 1995].

Reconnection is a process by which the magnetic fields of two regions of magnetised plasma become linked across their mutual boundary. The IMF becomes linked with the geomagnetic field across the magnetosphere's outer boundary, called the magnetopause. As the solar wind and the IMF continue to move away from the Sun, the connected geomagnetic field moves as well. Through combinations of reconnection, magnetic tension, and pressure, large-scale patterns of plasma motion are set up in the magnetosphere [*Dungey*, 1961].

Magnetically controlled plasma motion is readily observed in the magnetosphere and in the ionised upper layers of Earth's atmosphere, which are called the ionosphere. Because of the mapping of the geomagnetic field, as seen in Figure 1.1, the dynamics of a vast section of the mag-

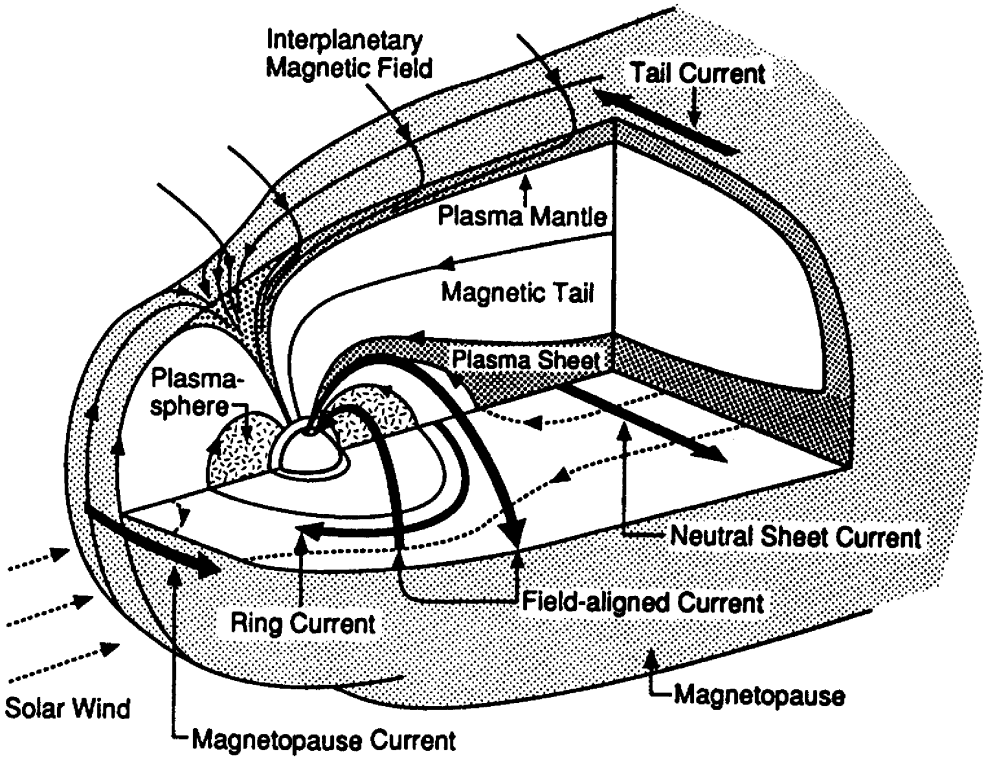

Figure 1.1: Schematic drawing of Earth's magnetosphere. The Earth is at the centre with its ionosphere shown as a thin layer, and the Sun is to the left. From *Russell* [1995].

netosphere are projected on the high-latitude ionosphere. Detecting the motion of the ionospheric plasma particles with radars on the ground provides valuable information about the movement of plasma in a much larger region: the magnetosphere.

Coupling of the magnetosphere and ionosphere occurs primarily through field-aligned currents, or FACs, flowing parallel to the magnetic field [*Cowley*, 2000]. FACs flow both up out of the ionosphere and down into it, as seen in Figure 1.1. (FACs and ionospheric plasma motion are connected, as will be shown in Section 2.4.) Knowledge of FACs is important for studying the connection between the ionosphere and the magnetosphere. FACs can show where horizontal currents flow within the ionosphere between the locations of downward FACs and upward FACs. FACs can also be used to study plasma dynamics in the magnetosphere.

1.1 Determining Field-Aligned Current

There are a number of ways to estimate FACs, and each way has its own advantages and disadvantages. From radar measurements of the ionospheric plasma velocity it is straightforward to determine the electric field in the ionosphere when the magnetic field is known. From the electric and magnetic fields, FACs can be determined if the ionospheric conductivity is known, but in practice the conductivity typically must be modelled or set to unity [e.g., *Sofko et al.*, 1995]. Ground-based magnetometers (magnetic field detectors) require similar modelling of the ionospheric conductivity to determine the ionospheric electric field and FACs [*Kamide et al.*, 1981]. Satellite-based magnetometers can detect FACs, but a satellite can only make single-point measurements. An impractically large number of satellites would be required to reach both spatial and temporal resolutions fine enough to see the whole picture of magnetospheric dynamics. The main advantage of the radar approach in this regard is its extensive spatial coverage.

The Super Dual Auroral Radar Network (SuperDARN), a global network of high frequency radars operated by an international scientific consortium [*Greenwald et al.*, 1995], was used for the work in this thesis. Each SuperDARN radar has a field of view of approximately 5.6 million square kilometres, and the combined network of 23 radars in the northern hemisphere and 12 radars in the southern hemisphere is able to observe a significant portion of the high-latitude ionosphere (poleward of 50° in the north and 60° in the south). Each SuperDARN radar sweeps through

its field of view once every 60 to 120 seconds in normal operations, meaning that a network-wide image of plasma convection can be obtained with a cadence that is useful for the study of magnetospheric dynamics. Data processing techniques allow the raw radar measurements to be converted into hemisphere-scale maps of plasma flow and electric potential that are invaluable for studying magnetosphere–ionosphere coupling.

1.2 Purpose and Scope

This thesis presents a novel technique for calculating estimates of FACs using SuperDARN data. While previous techniques for performing this task have used SuperDARN plasma velocity measurements to estimate FACs [e.g., *McWilliams*, 1997; *Sofko et al.*, 1995], the work presented here uses the electrostatic potential (voltage) functions produced in standard SuperDARN data analysis. The potential functions can be mathematically manipulated to obtain functions describing FAC per unit of ionospheric conductivity. Computer application of these FAC functions to standard SuperDARN potential data then directly produces hemispheric maps of estimated FAC per unit conductivity. The maps can be used to study FAC location and direction, and can be combined with data from other instruments to determine conductivity or combined with measured or modelled conductivity to obtain maps of FAC magnitude as well as direction.

The purpose of this thesis is to present the SuperDARN FAC estimation technique. Application of the technique to obtain new physical results (such as multi-instrument conductivity determination) and integration of separately determined conductivity into the technique are outside the scope of this thesis, although a short case study is presented to demonstrate the utility of the technique.

CHAPTER 2

BACKGROUND

The interaction between the solar wind and the Earth's magnetosphere and ionosphere produces effects that are observable in the magnetosphere and ionosphere and on the ground. The effects of the Sun–Earth interaction include plasma convection, FACs, and geomagnetic storms and substorms.

2.1 The Sun–Earth System

The interaction of the Sun and the Earth includes the solar wind of plasma particles that stream outward from the sun. The solar wind and the IMF interact with the Earth's geomagnetic field, allowing transfer of energy, momentum, and particles to take place between the solar wind and the magnetosphere.

2.1.1 The Sun and the Solar Wind

At the core of the Sun is a nuclear fusion reactor that converts protons into helium nuclei. Energy produced by the reactor travels outward from the core of the Sun and eventually heats the outer part of the Sun's atmosphere, called the corona. The corona undergoes supersonic expansion into interplanetary space, giving rise to the solar wind [*Parker*, 1958, 1965].

2.1.2 The Interplanetary Magnetic Field

The magnetic field of the Sun extends through the corona into interplanetary space, where it is called the IMF [*Parker*, 1965]. The interaction of the IMF and the solar wind plasma is governed by

the convection–diffusion equation for the plasma (which is derived in Appendix B in Section B.3):

$$\frac{\partial \mathbf{B}}{\partial t} = \nabla \times (\mathbf{v} \times \mathbf{B}) + \frac{1}{\mu_0 \sigma} \nabla^2 \mathbf{B}, \tag{2.1}$$

where $\mathbf{v}$ is the plasma velocity, $\mathbf{B}$ is the magnetic field vector, t is time, μ_0 is the permeability of free space, and σ is the conductivity of the plasma (parallel to $\mathbf{B}$). If parallel conductivity is small, magnetic diffusion (the second term of the right hand side) becomes significant, and plasma and magnetic flux may move perpendicular to the surrounding magnetic field. If parallel conductivity is high, diffusion becomes small and convection (the first term of the right hand side) dominates.

2.1.3 Frozen-In Flow

In the case of high parallel conductivity σ, equation 2.1 can be rewritten as

$$\mathbf{E} = -\mathbf{v} \times \mathbf{B} \tag{2.2}$$

by using Faraday's law,

$$\frac{\partial \mathbf{B}}{\partial t} = -\nabla \times \mathbf{E}. \tag{2.3}$$

The case of large parallel conductivity is called frozen-in flow or frozen-in flux. This condition is satisfied in the solar wind [*Baumjohann and Treumann*, 1997]. The electric field, the velocity, and the magnetic field are balanced according to equation 2.2. If this were not so, then the high conductivity would quickly redistribute the plasma until the arrangement reached a balanced state. The bulk motion of charged particles subject to these conditions (on a scale larger than their gyroradii) is described by what is called the convective drift, which is a rearrangement of equation 2.2 to read

$$\mathbf{v}_{\text{cnv}} = \frac{\mathbf{E} \times \mathbf{B}}{B^2}. \tag{2.4}$$

An important result of equation 2.2, and the origin of the term *frozen-in flux*, is that the magnetic flux through an arbitrary surface moving with the plasma is constant. This is shown in Appendix B in Section B.4.

2.1.4 Magnetic Reconnection

When σ becomes infinitely large, there is no diffusion of the magnetic field through the plasma, and conversely there is no movement of plasma particles across the magnetic field. However,

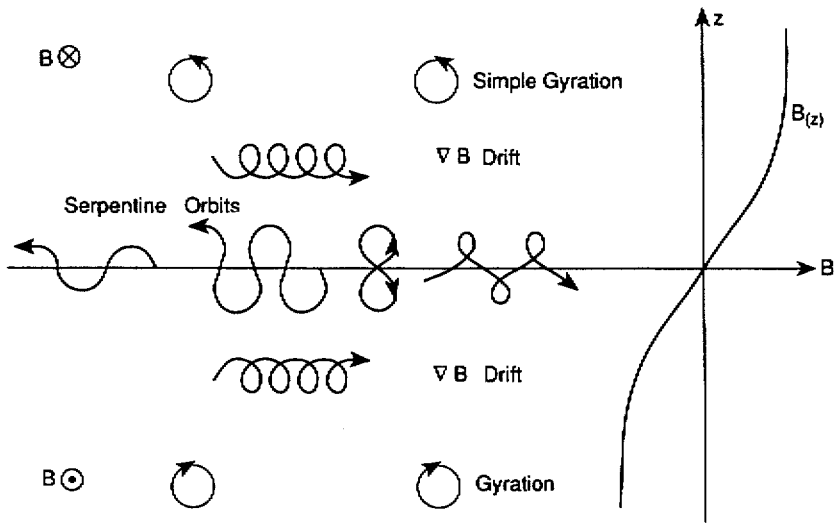

Figure 2.1: Trajectories of electrons in the boundary current sheet between two magnetised plasmas. The tangential component of the magnetic field varies as shown at the right, pointing into the page in the top half of the figure (also shown as a crossed circle at the upper left) and out of of the page in the bottom half of the figure (also shown as a dotted circle at the lower left). From *Hughes* [1995]; in turn, adapted from *Cowley* [1986].

at the boundary between two regions of magnetised plasma, any discontinuity in the tangential component of the magnetic field requires a current sheet to form. An example is the Chapman–Ferraro current sheet at the boundary between the solar wind and the magnetosphere [*Chapman and Ferraro*, 1930]. On the small length scale of the boundary current sheet, previous assumptions about the relative magnitudes of the convection term and the diffusion term of equation 2.1 break down and the diffusion term becomes significant. In this diffusion region, diffusion of the magnetic field occurs and plasma particles can diffuse across the magnetic field, moving perpendicular to the magnetic field lines.

Under the conditions of the diffusion region, plasma particles may cross the boundary between regions of frozen-in plasma in a process called magnetic reconnection [*Dungey*, 1961]. As the particles pass through the diffusion region, they encounter the new, differently oriented magnetic field, and their motion adjusts accordingly. For example, an electron that had been spiralling clockwise around an upward-pointing magnetic field will begin to spiral counter-clockwise when it enters a downward-pointing magnetic field region. Trajectories such as those shown in Figure 2.1 result, depending on the speeds of the particles and the angles at which they cross the boundary.

Plasma exits the diffusion region in reconnection "jets" [e.g., *Petschek*, 1964], moving perpen-

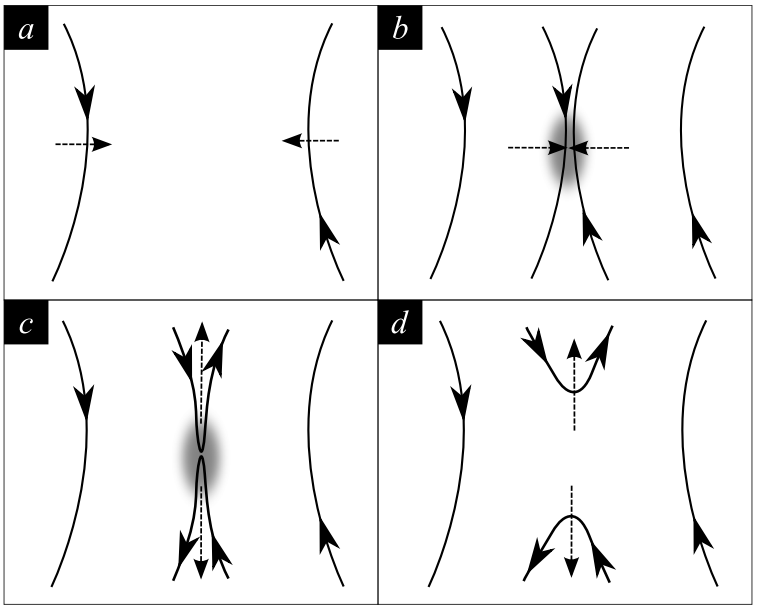

Figure 2.2: Two-dimensional sketch of magnetic reconnection. Magnetic field lines are drawn as solid lines, plasma motion is illustrated with dashed arrows, and the diffusion zone is represented by a diffuse grey region. Reconnection proceeds as follows: (*a*) antiparallel magnetic fields approach, (*b*) a diffusion zone forms on close approach, (*c*) reconfiguration of field topology occurs through the current sheet in the diffusion zone, and (*d*) the reconnected field moves away in a direction perpendicular to its original motion, carrying plasma in two oppositely-directed reconnection jets.

dicular to the direction of the plasma's original flow into the diffusion region. Once out of the diffusion region, the plasma returns to a frozen-in state. The magnetic field on both sides of the boundary is reconfigured in the process of reconnection, with the field on each side deconnecting from itself and the fields reconnecting to each other across the boundary through the diffusion of magnetic flux within the diffusion region.

A diagram of the magnetic reconnection process is shown in Figure 2.2. In panel (*a*) the two magnetised plasma regions with oppositely directed magnetic fields approach each other. In panel (*b*) a thin diffusion zone forms upon close approach, and particle and flux exchange begins to take place. In panel (*c*) the reconnected fields leave the diffusion zone after they have changed their topology. In panel (*d*) the two reconnection jets of plasma, frozen into the reconnected magnetic field, move away from the reconnection site. The remaining fields approaching from the left and right in panel (*d*) will undergo reconnection as the two regions continue to move toward one another.

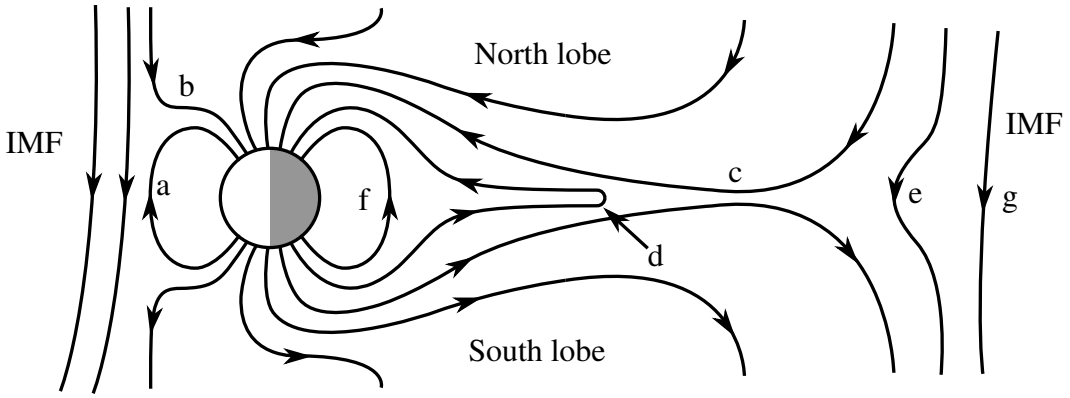

Figure 2.3: Earth's magnetosphere, showing the magnetotail (to the right of the Earth) and the Dungey cycle. The Earth is viewed in its equatorial plane with the Sun to the left.

2.2 The Magnetosphere

The Earth produces its own approximately dipolar magnetic field, which is known as the geomagnetic field. At the boundary between the geomagnetic field and the IMF, called the magnetopause, is the magnetopause current sheet, or the Chapman–Ferraro current [*Chapman and Ferraro*, 1930]. The cavity within the magnetopause is called the magnetosphere.

Because of the influence of the IMF and solar wind, the quasi-dipolar shape of the geomagnetic field is drastically altered beyond an altitude of a few Earth radii. On the sunward side (or dayside) of the Earth, the oncoming IMF exerts plasma pressure, compressing the geomagnetic field until the magnetic pressure of the geomagnetic field and the dynamic pressure of the solar wind are in balance. On the nightside, the geomagnetic field takes on an elongated teardrop shape called the magnetotail and extends far beyond the orbit of the Moon [*Hughes*, 1995]. A sketch of the magnetosphere is shown in Figure 2.3.

2.2.1 The Dungey Cycle

When the IMF points southward, the antiparallel arrangement of the IMF and the northward-pointing dayside geomagnetic field (see Figure 2.3) means that reconnection can take place on the dayside magnetopause, as was first recognised by *Dungey* [1961], who proposed the Dungey cycle of magnetospheric dynamics.

The cycle begins as the IMF and the geomagnetic field become linked through reconnection

on the dayside. The geomagnetic field line that has not yet undergone reconnection, shown at marker (a) in Figure 2.3, is called a "closed" field line because its complete closed loop is inside the magnetosphere. The geomagnetic field line that has reconnected with the IMF, shown at marker (b) in Figure 2.3, is called an "open" field line because close to the Earth it has the appearance of not closing on itself (although it necessarily does, through both Earth and Sun via the IMF). The open field forms what is known as the Earth's magnetospheric lobe regions. In each hemisphere, the region of the Earth's ionosphere through which the (open) lobe field lines pass is called the polar cap.

Because the open field beyond the magnetopause is still frozen into the solar wind it continues to move antisunward with the solar wind plasma. The portion of the open field within the magnetosphere also moves antisunward. This induces a motional electric field, the dawn-dusk electric field $\mathbf{E}_{DD}$. Figure 2.4 shows $\mathbf{E}_{DD}$, along with what is called the Region 1 FAC system (described in Section 2.4), as well as the associated plasma flow in the magnetosheath (outside the magnetopause) and within the ionosphere (described in Section 2.3.3). The duskward direction of the dawn-dusk electric field is the result of the southward magnetic field and the antisunward plasma flow, according to equation 2.2. The antisunward pull of the solar wind on the lobe field, combined with magnetic pressure and tension, forms the lobe into the elongated teardrop shape seen in the magnetotail in Figure 2.3.

In the magnetotail near the equatorial plane, the north and south lobe fields are adjacent and antiparallel, which provides opportunity for reconnection to occur between the north lobe and the south lobe near marker (c) in Figure 2.3. During reconnection in the magnetotail, two lobe field lines produce one IMF line and one closed geomagnetic field line. The geomagnetic field and the IMF are both restored to the topologies they had before undergoing reconnection at the dayside magnetopause. The newly reconnected geomagnetic field is still in a stretched state, however, as shown in Figure 2.3 at marker (d).

As the north and south lobes reconnect in the magnetotail, the reconnection jet of plasma that leaves the reconnection site moves primarily in the sunward and antisunward directions. The closed geomagnetic field at marker (d), now highly non-dipolar, relaxes toward the Earth, gradually returning to its former quasi-dipolar shape at marker (f) as a result of magnetic tension. The relaxing geomagnetic field continues to move sunward around the flanks of the Earth until it returns

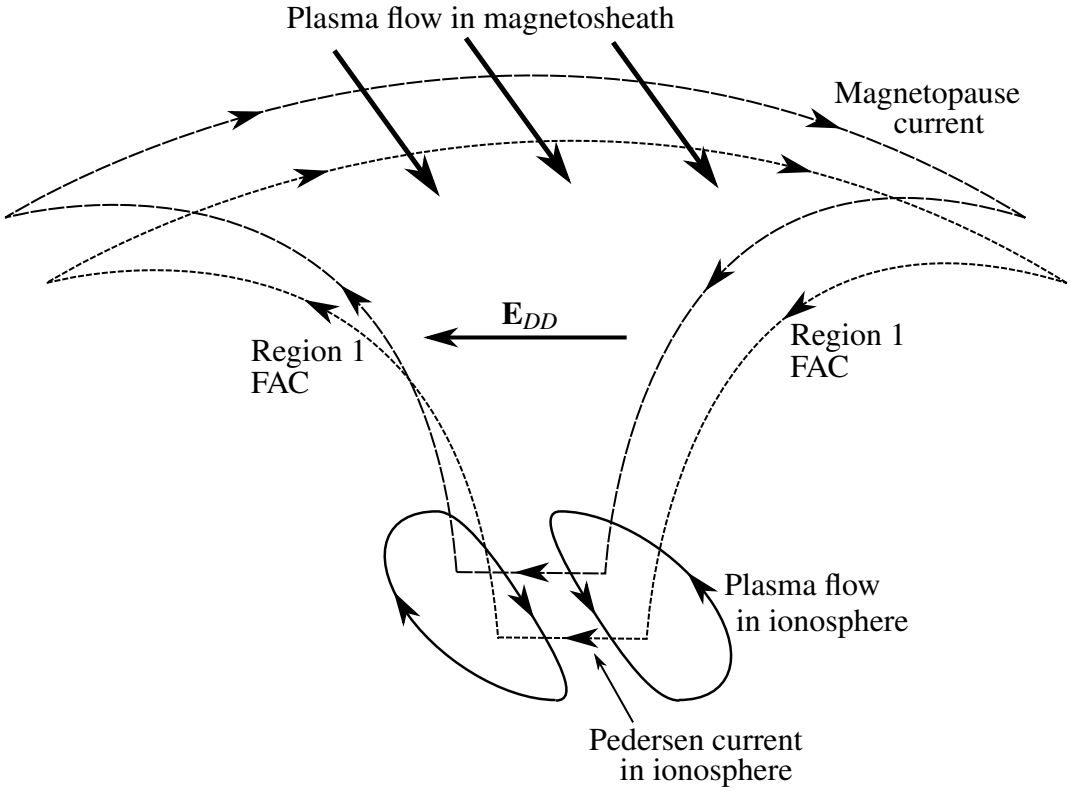

Figure 2.4: The Region 1 FAC system viewed from the magnetospheric lobe on the nightside of the Earth, with the sunward direction into the page and the antisunward magnetosheath flow (out of the page) shown at the top of the diagram. Currents are shown as dashed lines, and plasma flow and the dawn-dusk electric field $\mathbf{E}_{DD}$ are shown as solid lines. After *Cowley* [2000].

to the dayside magnetopause at marker (a), where it can undergo dayside reconnection again when IMF conditions are favourable. The newly reconnected IMF and its frozen-in plasma at marker (e), disconnected from the geomagnetic field, flow away from the Sun into interplanetary space at marker (g).

2.2.2 Magnetic Storms and Substorms

As dayside reconnection occurs, plasma of solar wind origin and plasma of ionospheric origin mingle along the newly reconnected field lines, particularly considering the high parallel conductivity. As the solar wind draws the newly created lobe field antisunward, ionospheric plasma spreads out parallel to the magnetic field and is carried farther out into the magnetosphere. When the lobe field is stretched out in the magnetotail and distant tail reconnection takes place between the north and south lobes, the plasma earthward of the tail reconnection site becomes effectively stored in the tail.

Reconnection of the north and south lobes can occur near the Earth, leading to the release of stored particles in reconnection jets. The particles travel easily along the magnetic field and precipitate into the ionosphere. Collisions between precipitating particles and atmospheric constituents produce auroral displays through particle excitation and de-excitation. First deduced by *Akasofu* [1964] from studies of the corresponding auroral behaviour, this process is called a magnetic substorm. *Akasofu*'s [1964] drawings of auroral displays seen in the phases of a substorm are presented in Figure 2.5. The particle precipitation that creates the auroral displays is important for changing the conductivity of the ionosphere on the nightside of the Earth.

The energy released in a substorm is primarily that which was transferred into the magnetosphere through reconnection under southward IMF conditions [*Birn*, 2007], but the plasma particles that precipitate into the ionosphere during a substorm are largely of atmospheric origin [*Lennartsson and Sharp*, 1982], having travelled outward into the tail along the lobe field. The buildup of plasma and energy in the tail, called the growth phase (or quiet phase) of the substorm, lasts approximately an hour. The beginning of the energy release is called the substorm onset, and corresponds to the first auroral brightening in the ionosphere, as defined by *Akasofu* [1964]. The onset is visible in Figure 2.5 as the heavy line of aurora at the bottom of panel **B**. The auroral displays occur during what is called the expansive phase of the substorm, which lasts tens of minutes. Fi-

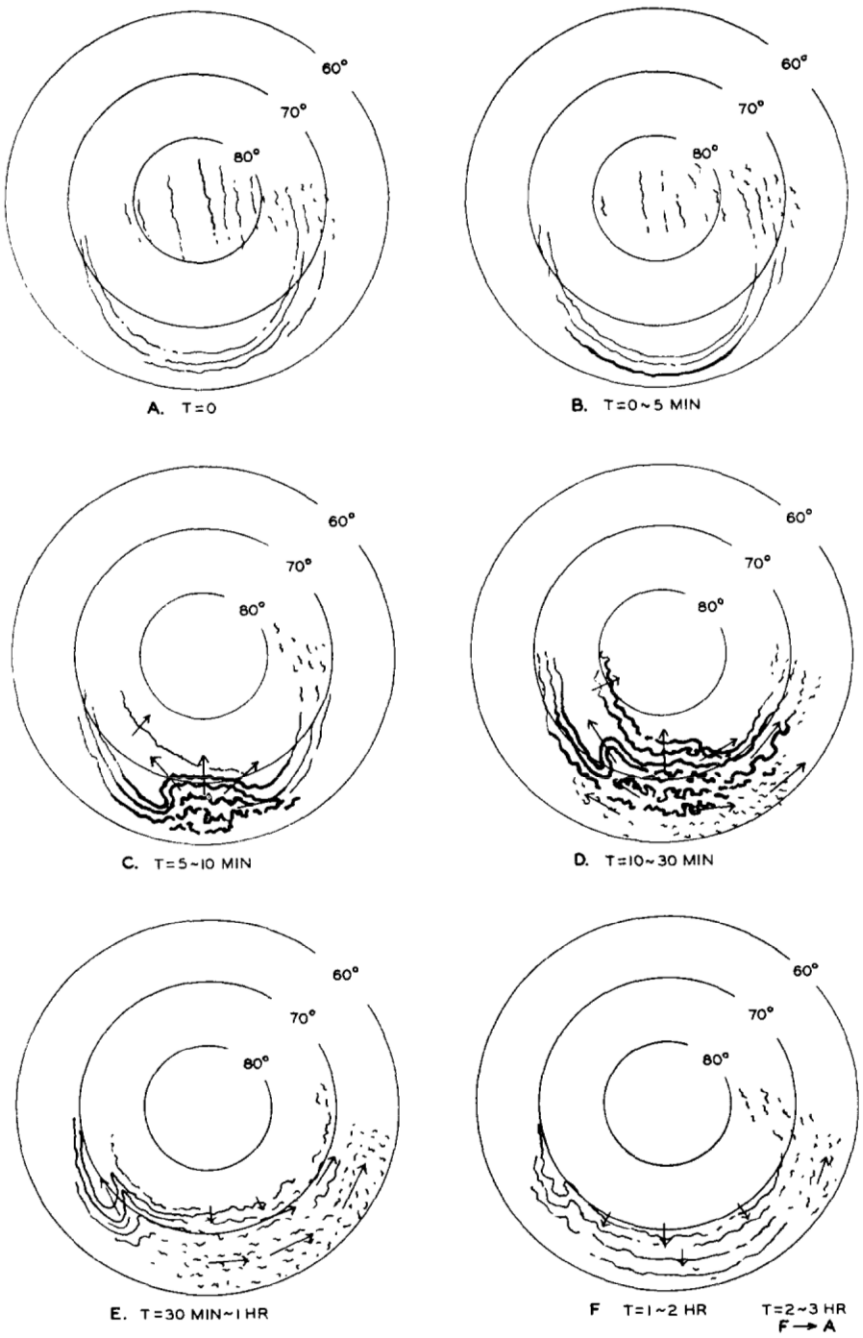

Figure 2.5: Phases of a substorm, showing patterns of aurora (wavy lines) and their motion (arrows). From *Akasofu* [1964]. Heavier lines indicate brighter aurora. The diagrams are in magnetic invariant latitude (MLAT) coordinates and magnetic local noon is upward. **A** shows the quiet phase; **B**, **C**, and **D** show the expansive phase; and **E** and **F** show the recovery phase.

nally, the return to "quiet" magnetic conditions is called the recovery phase, which may last a few hours. Substorms are described in more detail in, for example, *Akasofu* [1964] and *McPherron* [1970].

Should a long period (on the order of hours) of southward IMF occur, the prolonged, strong driving of magnetospheric dynamics can produce a magnetic storm, which is more dynamic and energetic than a substorm [*McPherron*, 1995]. The magnetospheric disturbance spreads, with nightside reconnection injecting high-energy particles near to the Earth and causing an intensification of the ring current, the westward-flowing near-earth magnetospheric current shown in Figure 1.1. (The ring current is described in Section B.2 of Appendix B.) A storm can last for days, until a change in the IMF slows the dayside reconnection that feeds the magnetotail, and loss processes sufficiently deplete the enhanced ring current. During a storm the southward magnetic field induced by the ring current is enhanced, causing a strong magnetic disturbance measured at the surface of the Earth [*McPherron*, 1995].

2.2.3 Reconnection Under Other IMF Conditions

Reconnection between the IMF and the geomagnetic field may occur for conditions other than directly southward IMF. Nearly any orientation of the IMF will be antiparallel to the geomagnetic field at some location on the magnetopause [*Speiser*, 1971]. For example, IMF that is southward with an additional east–west component can produce reconnection away from the subsolar point (the point on the magnetopause directly between the Earth and the Sun). In Figure 2.6, an example of reconnection under southward IMF conditions with a duskward IMF component is shown. Because of the angle of the IMF, reconnection occurs away from the subsolar point at the locations shown. The magnetic tension inherent in the sharply kinked lobe field causes the field lines to straighten, resulting in motion of the "footprints" of the lobe field in the ionosphere in the directions shown by the grey arrows in Figure 2.6. This east–west plasma motion is in addition to the antisunward motion caused by the antisunward flow of the solar wind.

Reconnection between the lobe field and the IMF is possible when the IMF is northward. For example, northward IMF with an antisunward component can reconnect with the north lobe field as shown in Figure 2.7. In this case the resulting field topologies begin as north lobe field and IMF and end as IMF and north lobe field, although both fields are left kinked and the north lobe field

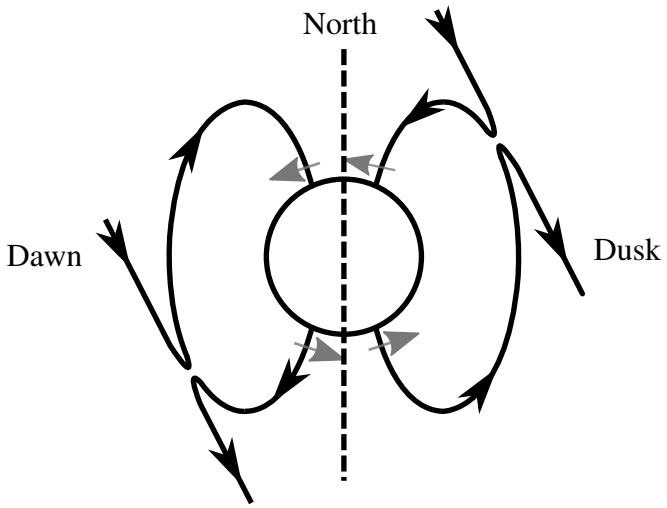

Figure 2.6: Dayside reconnection under southward and duskward IMF. The Earth is viewed in its equatorial plane from the direction of the Sun. The grey arrows indicate the east–west motion caused by magnetic tension in the newly reconnected and highly kinked open field lines.

is in an "overdraped" state. Plasma frozen into the north lobe earthward of the reconnection site remains on north lobe field while the tailward north lobe deconnects from the geomagnetic field, reconnects with the IMF, and travels antisunward with the solar wind into interplanetary space.

2.3 The Ionosphere

The most accessible part of the magnetosphere is the ionosphere, the ionised upper layers of Earth's atmosphere. At high enough altitudes the bulk motion of the ionospheric plasma is controlled by the electrodynamics of the magnetosphere. The ionosphere acts like a gigantic cathode ray tube screen, showing a projection of activity throughout the magnetosphere. (This is especially true when particles precipitating along the magnetic field interact with atmospheric particles and stimulate photon emission, like the interaction of electrons with a phosphor screen.)

2.3.1 The Production and Structure of the Ionosphere

Ionisation of neutral atoms and molecules in the atmosphere by sunlight depends on the amount of incident energy absorbed by a parcel of air. Absorption depends on the density of the air, on the radiation cross-section of the atoms or molecules, and on the amount of incident light, which

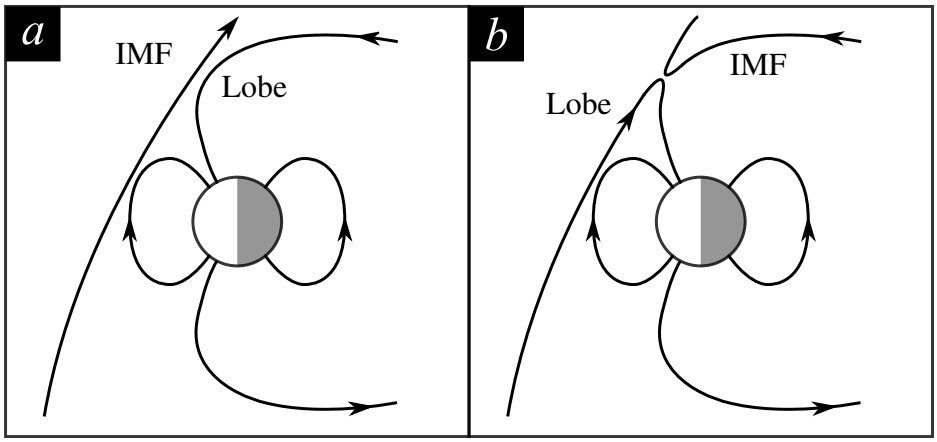

Figure 2.7: Reconnection for northward IMF. The Earth is viewed from the duskside, with north up and the Sun to the left. (*a*) The IMF reconnects with the north lobe field, producing (*b*) overdraped north lobe field and IMF.

depends on the integrated absorption along the path of the incoming solar radiation. An efficiency factor describes how many electrons are liberated for a given quantity of absorbed energy. The production function describes the resulting altitude profile of the generation of ions and electrons. Rather than an exponential shape, the production function Q has a peak, described as follows by *Chapman* [1931]. If Q_{mo} is the peak production rate at the subsolar point (directly between the Earth and the Sun) and h_{mo} is the altitude of that subsolar peak, then the production function Q overhead is

$$Q = Q_{mo} \exp\left(1 - z - \sec\chi \exp\left(-z\right)\right), \tag{2.5}$$

where χ is the solar zenith angle and z is the normalised altitude. The solar zenith angle is the angle to the direction of the Sun measured down from the local vertical. Here, z is given by

$$z = \frac{h - h_{mo}}{H}, \tag{2.6}$$

where h is altitude and H is the scale height of the atmospheric gas. H is given by

$$H = \frac{k_B T}{mg}, \tag{2.7}$$

where k_B is Boltzmann's constant, T is temperature, m is molecular mass, and g is gravitational acceleration.

Photoionisation by the Sun is not the only source of ions in the ionosphere. Particularly at high latitudes, precipitation of magnetospheric plasma particles into the ionosphere is also a significant source. Charged particles in the magnetosphere that have sufficient parallel kinetic energy

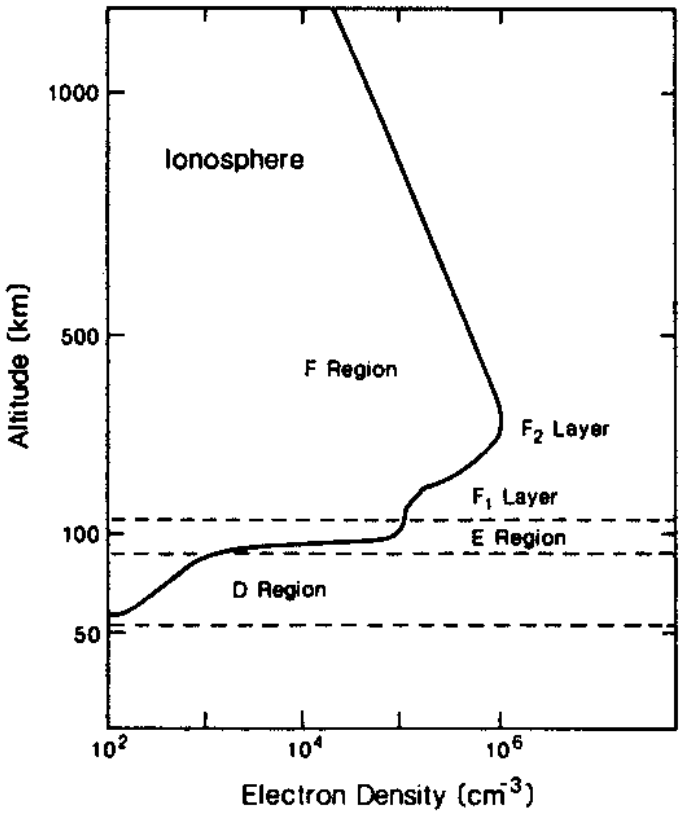

Figure 2.8: An ionospheric electron density profile showing D, E, and F regions. From *Russell* [1995].

will reach altitudes where atmospheric collisions are likely. The effects of the collisions include ionisation of atmospheric particles by the primary, precipitating particles, and ionisation by both the secondary particles and the *bremsstrahlung* photons created by the primary interactions [*Luhmann*, 1995]. The production function for particle impact ionisation depends on atmospheric density, precipitation particle flux, scattering and absorption cross sections, and secondary production efficiency.

When ion production is combined with ion loss through such processes as recombination, and with vertical and horizontal transport, an overall ion or electron density profile is established. A typical electron density profile for Earth's ionosphere is shown in Figure 2.8. The regions of the ionosphere marked in the figure are produced through different combinations of production, loss, and transport processes; for example, the high-energy end of the particle precipitation spectrum (including galactic cosmic rays) is important in the production of the D region [*Luhmann*, 1995].

2.3.2 Ionospheric Plasma Dynamics

The responses of ionospheric plasma constituents to electric and magnetic fields also differentiate the regions of the ionosphere. The electron-neutral collision frequency ν_{en} is considerably lower than the electron cyclotron frequency ω_{ce} above approximately 80 km [*Carlson and Egeland*, 1995] (ν_{en} is on the order of 10^4 s^{-1} and ω_{ce} is nearly 10^7 s^{-1} [*Luhmann*, 1995]), so electrons are magnetised and respond to the frozen-in convective drift (equation 2.4) in the E and F regions. In the F region, the ion–neutral collision frequency ν_{in} is less than the ion cyclotron frequency ω_{ci}, so ions are also magnetically controlled and move with the convective drift. In the E region, ion–neutral collisions are frequent enough that ν_{in} is greater than ω_{ci} (the former on the order of 10^3 s^{-1} below 120 km and the latter just above 10^2 s^{-1} [*Luhmann*, 1995]). As a result, the ions at E-region altitudes are unable to gyrate: they lose their frozen-in behaviour and respond primarily to electric fields. In the vicinity of 80 km altitude and below (that is, the D region), both electrons and ions collide so frequently with neutrals that they become demagnetised.

In the E region, the ions, much more affected by collisions than the electrons, drift in the electric field direction, relative to the electrons, and form a Pedersen current $\mathbf{J}_P$, written [e.g., *Schunk and Nagy*, 1999]:

$$\mathbf{J}_P = \sigma_P \mathbf{E}, \tag{2.8}$$

to first order (that is, neglecting the influence of the neutrals), where σ_P is the Pedersen conductivity. The electrons, mostly magnetically controlled, drift perpendicular to the electric and magnetic fields, relative to the ions, and form a Hall current $\mathbf{J}_H$, written [e.g., *Schunk and Nagy*, 1999]:

$$\mathbf{J}_H = \sigma_H \frac{\mathbf{B} \times \mathbf{E}}{B}, \tag{2.9}$$

again to first order (neglecting neutral influence), where σ_H is the Hall conductivity.

Because the E-region electrons are magnetically controlled, they do not affect σ_P to first order. The Pedersen conductivity, considering only the ion contribution, is given by [e.g., *Schunk and Nagy*, 1999]:

$$\sigma_P = \sum_i \frac{N_i e_i^2}{m_i \nu_i} \frac{\nu_i^2}{\nu_i^2 + \omega_{ci}^2}, \tag{2.10}$$

where the sum is over all ion species i, N_i is the ion density, e_i is the ion charge, m_i is the ion mass, and the ion collision frequency ν_i contains collisions with all neutral species for ion i. The Hall

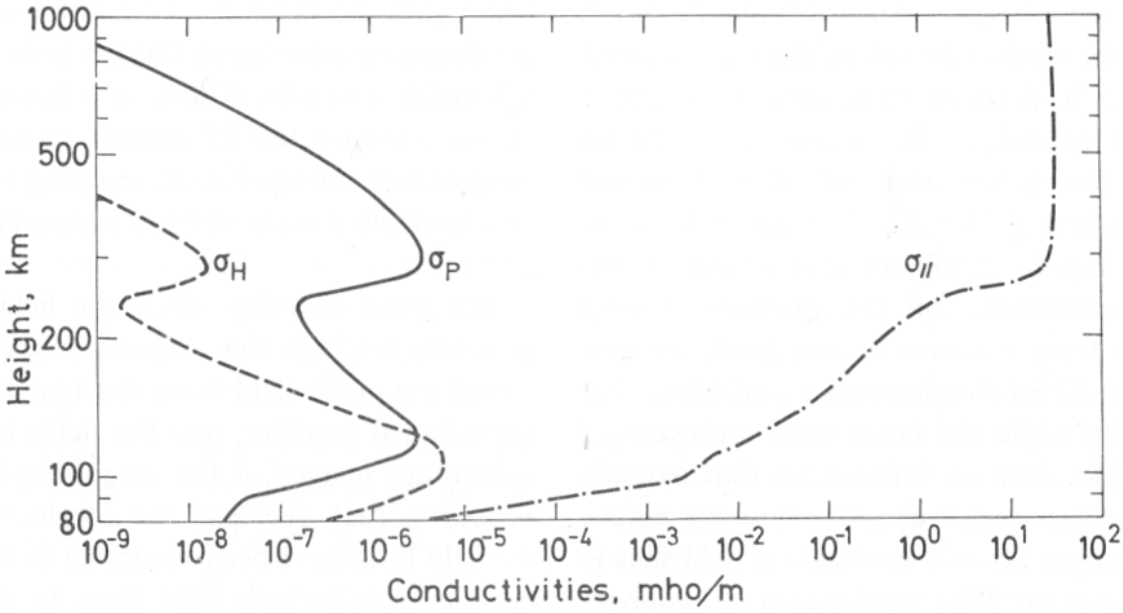

Figure 2.9: Ionospheric Pedersen (σ_P), Hall (σ_H), and parallel ($\sigma_\parallel$) conductivity profiles on the nightside. From *Boström* [1973].

conductivity, considering that $\nu_{en} \ll \omega_{ce}$ above approximately 80 km altitude, can be written [e.g., *Schunk and Nagy*, 1999]:

$$\sigma_H = -\sum_i \frac{N_i e_i^2}{m_i \nu_i} \frac{\nu_i \omega_{ci}}{\nu_i^2 + \omega_{ci}^2} + \frac{N_e e^2}{m_e \nu_e} \frac{\nu_e}{\omega_{ce}}, \tag{2.11}$$

where N_e is the electron density, e is the electron charge, m_e is the electron mass, and the electron collision frequency ν_e contains all electron–neutral collisions. The parallel (or specific) conductivity $\sigma_\parallel$ (or σ_0) is primarily dependent on electrons because they are much more mobile than ions, and is given by [e.g., *Schunk and Nagy*, 1999]:

$$\sigma_\parallel = \frac{N_e e^2}{m_e \nu_e'}, \tag{2.12}$$

where the modified electron collision frequency ν_e' contains both electron–ion and electron–neutral collisions.

The Pedersen and Hall conductivities fall off with height, as seen in Figure 2.9 from *Boström* [1973], which shows typical nightside conductivity profiles (without particle precipitation). Currents parallel to the magnetic field (that is, FACs) become the only significant currents at high altitudes. The parallel conductivity increases with height as seen in Figure 2.9, consistent with the large parallel conductivity found in frozen-in regions such as the F region.

2.3.3 Ionospheric Convection

The magnetospheric circulation that occurs in response to reconnection creates patterns in the motion of the magnetically controlled F-region plasma. The simplest is that occurring under conditions of directly southward IMF, in which case the lobe field moves directly antisunward to the magnetotail and the reconnected geomagnetic field moves sunward around the flanks of the Earth. The resulting ionospheric convection pattern is like the schematic in Figure 2.10, from *Cowley* [2000], commonly called a two-cell convection pattern. As the magnetic field reconnects with the IMF on the dayside, plasma flows into the polar cap at magnetic noon. Tailward convection over the pole ensues, consistent with the dawn-dusk electric field $\mathbf{E}_{DD}$ in the polar cap (which corresponds to the dawn-dusk electric field farther out in the magnetosphere) and the downward-pointing magnetic field, and according to $\mathbf{v} = \mathbf{E} \times \mathbf{B}/B^2$ (equation 2.4). As the north and south lobe fields reconnect in the magnetotail, the F-region plasma transfers from open to closed field lines, leaving the polar cap at magnetic midnight. Finally, sunward convection draws the plasma on the closed field lines around the Earth on the equatorward side of the polar cap boundary. The electric field equatorward of the polar cap boundary points equatorward on the dawnside and poleward on the duskside. The quasi-dipolar shape of the magnetic field at these latitudes means that the electric field equatorward of the polar cap maps along the magnetic field to the magnetospheric dawn-dusk electric field in the equatorial plane of the Earth [*Dungey*, 1961].

When the dayside reconnection site is formed away from the subsolar point because of a dawn–dusk component in the IMF, the direction of the cross polar cap flow of plasma is altered from the directly antisunward flow shown in Figure 2.10. Dayside ionospheric plasma flows in a direction contrary to the orientation of the dawn–dusk component of the IMF. The non-symmetrical two-cell flow is shown by the grey arrows in Figure 2.6. The return flow at lower latitudes is not affected. The resulting convection pattern in the northern-hemisphere F-region ionosphere is like that shown schematically in Figure 2.11, where one of the convection cells is larger and more circular (the round cell) and the other is smaller and crescent-shaped (the crescent cell). The example in Figure 2.11 is for IMF with a duskward component, the same configuration as in Figure 2.6. For IMF with a dawnward component the convection pattern in Figure 2.11 is mirrored across the noon–midnight axis.

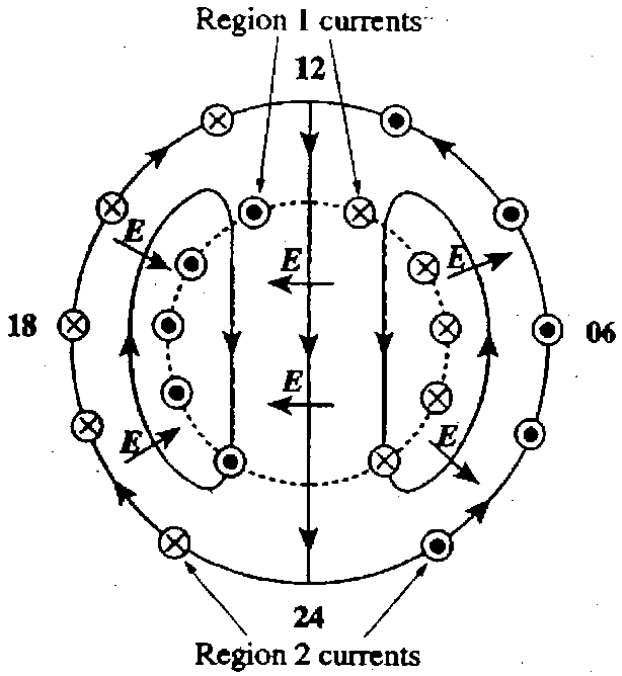

Figure 2.10: Ionospheric two-cell plasma convection pattern for southward IMF. Plasma flow is shown with closed solid lines, electric field **E** with arrows, and the polar cap boundary with a dashed line. Magnetic field-aligned currents are shown flowing upward out of the ionosphere (out of the page, dotted circles) and downward into the ionosphere (into the page, crossed circles). From *Cowley* [2000].

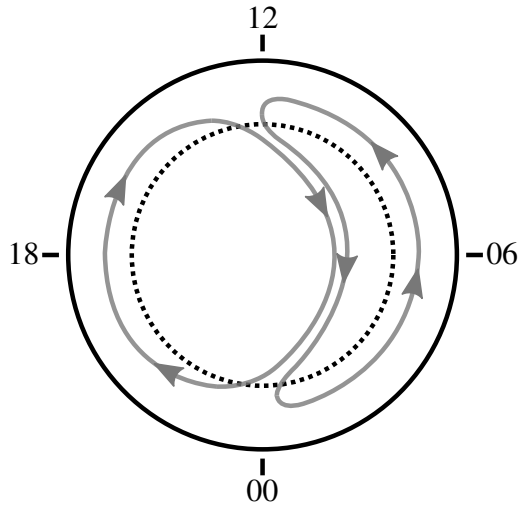

Figure 2.11: Ionospheric convection pattern (northern hemisphere) under southward IMF with a duskward component. Viewed from above the north pole with the Sun toward the top of the page—that is, in magnetic local time (MLT) coordinates.

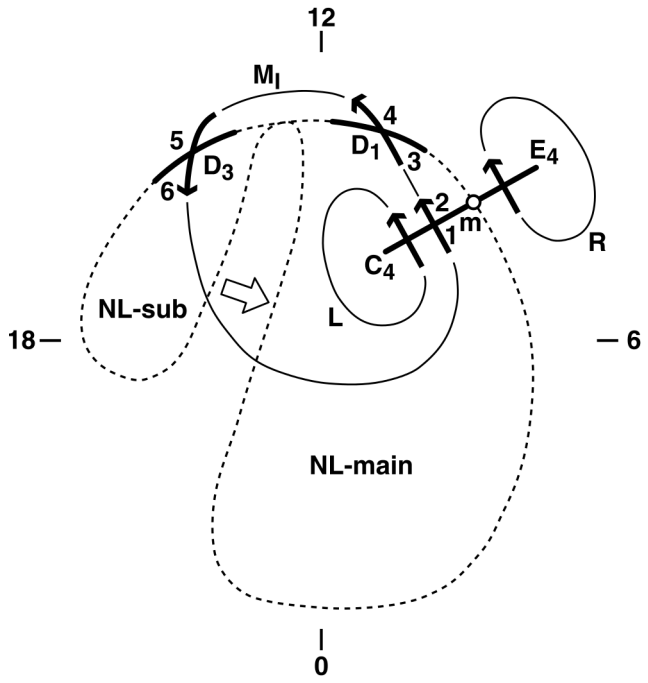

Figure 2.12: Northern hemisphere convection pattern expected under conditions with prolonged and strongly northward IMF with a dawnward component. From *Watanabe and Sofko* [2009]. The open–closed field line boundary is shown as a dashed line. Heavy lines without arrows represent the projections of reconnection sites on the ionosphere and are labelled according to the reconnection geometries responsible (not shown). Plasma flowlines are shown as solid lines with heavy arrows marking plasma flow across reconnection lines. The diagram is plotted in MLT coordinates.

During periods of northward IMF or of IMF dominated by a dawn–dusk component, reconnection can take place simultaneously at different locations on the magnetopause. Each reconnection site maps along the magnetic field to one or two locations in the ionosphere, moving the ionospheric plasma and changing the open/closed identity of the magnetic fields according to the configuration of the IMF and the geomagnetic field. As a result, the convection pattern seen in the ionosphere can become more complicated.

An example of a complicated convection pattern from *Watanabe and Sofko* [2009] is shown in Figure 2.12. Here the IMF is primarily northward, tilted less than 30° toward dawn from the purely northward direction. A type of reconnection referred to as interchange reconnection is occurring between the IMF and the lobe field. This interchange reconnection is as depicted in Figure 2.7, except for being away from the Earth–Sun axis. The IMF–north lobe reconnection site maps to the line marked "C_4" in Figure 2.12, showing that ionospheric plasma initially on the north lobe

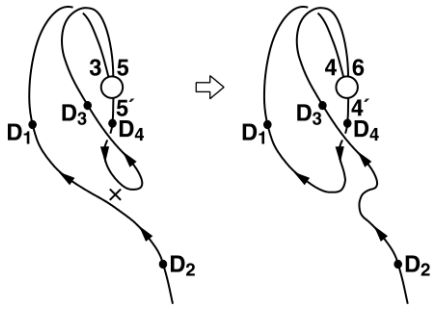

Figure 2.13: Interchange reconnection between the north lobe and the dayside closed geomagnetic field. From *Watanabe and Sofko* [2009]. The Earth is viewed from the sunward side with north up. The changing field topology proceeds from the left image to the right image (as indicated by the open white arrow) when reconnection occurs at the place marked with an "X" to the south of the Earth.

is still on the north lobe after reconnection and circulates within the polar cap, always in the open lobe magnetic field region. Interchange reconnection is also taking place between the overdraped north lobe and the closed geomagnetic field as shown in Figure 2.13, also from *Watanabe and Sofko* [2009]. In this case, the ionospheric footprint of the reconnection is at the heavy lines labelled "D_1" and "D_3" in Figure 2.12, showing how the northern-hemisphere ionospheric plasma associated with this interchange reconnection passes from the lobe field to the closed field at the former site and from closed field to the lobe field at the latter site.

The convection pattern shown in Figure 2.12 is the result of a variety of reconnection geometries occurring simultaneously, as modelled and described in *Watanabe and Sofko* [2009], and it is beyond the scope of this thesis to discuss all of them. Still, features such as the circulation in open lobe field at the centre of the figure (around the C_4 label) and across the open–closed field line boundary (OCFLB) on the dayside (at the D_1 and D_3 labels) can be detected in convection patterns measured by SuperDARN, and can be studied using the technique described in this thesis. Models such as *Watanabe and Sofko*'s [2009] can then be applied to the interpretation of the proposed technique.

The bulk $\mathbf{E} \times \mathbf{B}$ plasma flow in the F region reveals the dynamics of the magnetosphere, but plasma at lower altitudes is affected as well. Pedersen and Hall currents, mentioned above, still flow in the lower F region and the E region. Hall currents, which flow in the E region, are due to electrons moving in the $\mathbf{E} \times \mathbf{B}$ direction relative to collision-controlled ions. Hall currents form closed loops in the ionosphere, along the same streamlines followed by the upper F region bulk

plasma flow $\mathbf{v}_{cnv}$. Pedersen currents flow in the lower F region in the direction of the electric field (for example, the electric field **E** in Figure 2.10 for the southward-IMF Dungey cycle). Pedersen currents have finite divergence in some places and therefore must complete their current loops outside the ionospheric plane. They close through FACs that flow in and out of the ionosphere along the geomagnetic field.

2.4 Field-Aligned Currents

The FACs flowing parallel (and antiparallel) to the magnetic field between the ionosphere and the magnetosphere are an important means of coupling between the magnetosphere and the ionosphere. FACs and the convective drift associated with solar wind-driven reconnection and convection described in Section 2.3.3 are particularly important because they can be used as ionospheric indicators of magnetospheric activity. Plasma drifts besides the convective drift, such as the curvature–gradient drift, affect plasma in the equatorial magnetosphere but are not significant at high latitudes. (The curvature–gradient drift is described in Section B.2 of Appendix B.) The differing plasma behaviours in the magnetosphere and ionosphere produce stresses that are communicated between the regions by FACs.

2.4.1 The FAC Equation

Not only are FACs and the convective drift the main ionospheric indicators of magnetospheric dynamics, but signatures of FACs can be found in the plasma drift patterns using radar. Ground-based magnetometers can also be used to determine currents, but it is not possible to discern between horizontal currents and FACs using magnetometer data alone [*Chapman*, 1935]. Horizontal equivalent current functions can be derived from magnetometer measurements, but ionospheric conductance must be known or modelled before FACs can be determined [*Kamide et al.*, 1981]. Satellite-based magnetometers measure the magnetic perturbations caused by FACs directly, but FACs must be calculated from perturbation data by assuming infinite sheets of current [*Iijima and Potemra*, 1976b]. Additionally, global-scale coverage takes hours for a satellite, although a squadron of satellites significantly reduces the time required.

Ground-based measurements of ionospheric plasma velocity allow data to be obtained with fine

spatial and temporal resolution (on the order of hundreds of kilometres and on the order of minutes, respectively). The data can be used to estimate the locations and intensities of FAC ionospheric footprints. This is the method used by *Sofko et al.* [1995] and *McWilliams* [1997] and reviewed by *Chisham et al.* [2007]. As shown by, for example, *Sofko et al.* [1995], an expression for FAC can be found in terms of the electric and magnetic fields, the F-region convective drift velocity, and the Pedersen and Hall conductivities by starting with the continuity equation:

$$\nabla \cdot \mathbf{J} = -\frac{d\rho}{dt} = 0, \tag{2.13}$$

where $\mathbf{J}$ is total current density, ρ is charge density, and t is time. On a large enough spatial scale the charge density of the quasi-neutral plasma can be assumed not to vary with time. The divergence can be broken down into components perpendicular and parallel to the magnetic field:

$$\nabla \cdot \mathbf{J} = \nabla_{\perp} \cdot \mathbf{J}_{\perp} + \nabla_{\parallel} \cdot \mathbf{J}_{\parallel} = 0. \tag{2.14}$$

The parallel component is chosen here to be positive when pointing upward out of the ionosphere along $\mathbf{B}$, which is antiparallel to the magnetic field in the high-latitude northern hemisphere and parallel in the high-latitude southern hemisphere. Choosing an integration volume in the form of a field-aligned cylinder, as shown in Figure 2.14, and using an infinitesimal volume $d\tau$, equation 2.14 can be written

$$\int d\tau \nabla_{\perp} \cdot \mathbf{J}_{\perp} = -\left(J_{\parallel}^{top} - J_{\parallel}^{bottom}\right) A, \tag{2.15}$$

where A is the cross-sectional area of the integration volume (assumed to be approximately constant over the length of the volume) and the top and bottom parallel current are considered separately. If the bottom of the integration volume is at a low enough altitude that conductivity is negligible there, the bottom parallel current $J_{\parallel}^{bottom}$ is zero (as is the perpendicular current at the bottom). Rearranging,

$$AJ_{\parallel} = -A \int dh \nabla_{\perp} \cdot \mathbf{J}_{\perp}, \tag{2.16}$$

if $d\tau = Adh$ for height h. The parallel current has been simplified to $J_{\parallel}$, now only flowing out the top of the volume, and the cross-sectional area A cancels. In practice, if the top of the integration volume is at a typical SuperDARN measurement altitude of 300 km and the bottom of the volume is at 80 km, the top area will exceed the bottom area by approximately 0.1% at 70° MLAT according to the methods of *Walker and Sofko* [2016].

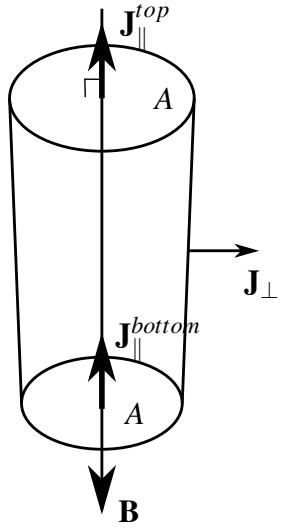

Figure 2.14: The integration volume for the FAC equation. **B** is the geomagnetic field (downward-pointing in the northern hemisphere), A is the cross-sectional area of the integration volume (approximately constant), the heavy arrows $\mathbf{J}_{\parallel}^{top}$ and $\mathbf{J}_{\parallel}^{bottom}$ are the parallel current at the top and bottom of the volume, respectively, and $\mathbf{J}_{\perp}$ is the perpendicular current.

The perpendicular current can be broken down into the Pedersen and Hall currents, and the divergence can be brought out of the integral:

$$J_{\parallel} = -\nabla_{\perp} \cdot \int dh \left(\sigma_P \mathbf{E} + \sigma_H \frac{\mathbf{B} \times \mathbf{E}}{B} \right). \tag{2.17}$$

The conductivities, the electric field, and the magnetic field can be replaced with their height-integrated weighted means:

$$J_{\parallel} = -\nabla_{\perp} \cdot \left(\Sigma_P \langle \mathbf{E} \rangle + \Sigma_H \left\langle \frac{\mathbf{B} \times \mathbf{E}}{B} \right\rangle \right), \tag{2.18}$$

where $\Sigma_P = \int dh \sigma_P$ and $\Sigma_H = \int dh \sigma_H$ are the height-integrated Pedersen and Hall conductivities, respectively, and the means of the fields are represented with $\langle\rangle$. It may be noted that the Pedersen current peak is higher than the Hall current peak by tens of kilometres, but the variation in magnetic and electric fields over that range is negligible. The divergence can be applied to each term to yield

$$J_{\parallel} = -\left(\langle \mathbf{E} \rangle \cdot \nabla_{\perp} \Sigma_P + \Sigma_P \nabla_{\perp} \cdot \langle \mathbf{E} \rangle + \langle \frac{\mathbf{B} \times \mathbf{E}}{B} \rangle \cdot \nabla_{\perp} \Sigma_H + \Sigma_H \nabla_{\perp} \cdot \langle \frac{\mathbf{B} \times \mathbf{E}}{B} \rangle \right). \tag{2.19}$$

If the integration volume extends from the E region at the bottom to the altitude of SuperDARN measurements at the top, it is convenient to replace the mean electric field with the electric field

measured by SuperDARN (that is, calculated from SuperDARN convective drift velocity measurements) and replace the mean magnetic field with the magnetic field at SuperDARN altitudes. Over the same 300 km to 100 km range as before, at 70° MLAT the magnetic field increases by approximately 0.1% and the electric field increases by approximately 4% [*Walker and Sofko*, 2016], while at 79° MLAT the magnetic field increases by less than 0.1% and the electric field increases by less than 6%. The small change in magnetic field warrants replacement of $\langle \mathbf{B} \rangle$ with $\mathbf{B}$, assuming the field to be approximately constant. The larger change in the electric field from the top to the bottom of the integration volume introduces error into the calculation, but within the scope of this thesis the error is acceptable.

At the top of the integration volume, plasma follows the convective drift, so equation 2.2, $\mathbf{E} = -\mathbf{v} \times \mathbf{B}$, may be used. The mean electric field $\langle \mathbf{E} \rangle$ is replaced with the convective drift electric field $\mathbf{E}$. The divergence of the electric field can be written

$$\begin{aligned} \nabla_\perp \cdot \mathbf{E} &= -\nabla_\perp \cdot (\mathbf{v}_{cnv} \times \mathbf{B}) \\ &= \mathbf{v}_{cnv} \cdot (\nabla_\perp \times \mathbf{B}) - \mathbf{B} \cdot (\nabla_\perp \times \mathbf{v}_{cnv}) \\ &= \mu_0 \mathbf{v}_{cnv} \cdot \left(\mathbf{J}_\perp + \varepsilon_0 \frac{\partial \mathbf{E}}{\partial t} \right) - \mathbf{B} \cdot (\nabla_\perp \times \mathbf{v}_{cnv}) \,, \end{aligned} \tag{2.20}$$

replacing the curl of the magnetic field using Ampère's law:

$$\nabla \times \mathbf{B} = \mu_0 \left(\mathbf{J} + \varepsilon_0 \frac{\partial \mathbf{E}}{\partial t} \right). \tag{2.21}$$

Assuming the fields vary slowly with time, the time derivative is approximately zero. One can split the perpendicular current into a Pedersen component $\mathbf{J}_P$ and a Hall component $\mathbf{J}_H$:

$$\begin{aligned} \nabla_\perp \cdot \mathbf{E} &= \mu_0 \mathbf{v}_{cnv} \cdot (\mathbf{J}_P + \mathbf{J}_H) - \mathbf{B} \cdot (\nabla_\perp \times \mathbf{v}_{cnv}) \\ &= \mu_0 \mathbf{v}_{cnv} \cdot \mathbf{J}_H - \mathbf{B} \cdot (\nabla_\perp \times \mathbf{v}_{cnv}) \\ &= -\mu_0 \Sigma_H B v_{cnv}^2 - \mathbf{B} \cdot (\nabla_\perp \times \mathbf{v}_{cnv}) \,. \end{aligned} \tag{2.22}$$

In the equation above, $\mathbf{J}_P = \Sigma_P \langle \mathbf{E} \rangle$ has been used to eliminate the Pedersen current from the dot product, knowing that $\mathbf{v}_{cnv} \perp \mathbf{E}$. Also,

$$\mathbf{J}_H = \Sigma_H \langle \frac{\mathbf{B} \times \mathbf{E}}{B} \rangle = -\Sigma_H B \mathbf{v}_{cnv} \tag{2.23}$$

has been used for the Hall current, following the same argument as above regarding the mean.

The divergence of $\mathbf{B}\times\mathbf{E}/B$ is

$$\begin{aligned}\nabla_\perp\cdot\frac{\mathbf{B}\times\mathbf{E}}{B} &= \nabla_\perp\frac{1}{B}\cdot(\mathbf{B}\times\mathbf{E})+\frac{\nabla_\perp\cdot(\mathbf{B}\times\mathbf{E})}{B}\\ &= \frac{\nabla_\perp B}{B^2}\cdot\left(-B^2\mathbf{v}_{cnv}\right)+\frac{\mathbf{E}\cdot(\nabla_\perp\times\mathbf{B})-\mathbf{B}\cdot(\nabla_\perp\times\mathbf{E})}{B},\end{aligned} \tag{2.24}$$

using the convective drift equation (2.4) in the first term on the right. Using Faraday's law (equation 2.3) and Ampère's law (equation 2.21),

$$\begin{aligned}\nabla_\perp\cdot\frac{\mathbf{B}\times\mathbf{E}}{B} &= -\mathbf{v}_{cnv}\cdot\nabla_\perp B+\frac{\mu_0\mathbf{E}\cdot\left(\mathbf{J}_P+\mathbf{J}_H+\varepsilon_0\frac{\partial\mathbf{E}}{\partial t}\right)+\mathbf{B}\cdot\frac{\partial\mathbf{B}}{\partial t}}{B}\\ &= -\mathbf{v}_{cnv}\cdot\nabla_\perp B+\frac{\mu_0}{B}\mathbf{E}\cdot\mathbf{J}_P\\ &= -\mathbf{v}_{cnv}\cdot\nabla_\perp B+\frac{\mu_0\Sigma_P E^2}{B}\\ &= -\mathbf{v}_{cnv}\cdot\nabla_\perp B+\mu_0\Sigma_P v_{cnv}^2 B,\end{aligned} \tag{2.25}$$

assuming again that the time derivatives are negligible, and noting that only the Pedersen current survives the dot product with the electric field.

Substituting equation 2.22 and equation 2.25 into equation 2.19 and cancelling like terms, the full FAC equation in terms of ionospheric parameters is

$$J_\parallel = \Sigma_P\mathbf{B}\cdot(\nabla_\perp\times\mathbf{v}_{cnv})+\Sigma_H\mathbf{v}_{cnv}\cdot\nabla_\perp B-\mathbf{E}\cdot\nabla_\perp\Sigma_P+B\mathbf{v}_{cnv}\cdot\nabla_\perp\Sigma_H. \tag{2.26}$$

Not all terms of the FAC equation are significant in the context of the work at hand. A dipolar approximation to the geomagnetic field is applicable at ionospheric altitudes:

$$\mathbf{B} = \frac{B_{eq,s}R_E^3}{r^3}\left(-2\cos\vartheta\hat{\mathbf{r}}-\sin\vartheta\hat{\vartheta}\right), \tag{2.27}$$

where $B_{eq,s} = 0.310\times10^{-4}$ T is the magnetic field at the equator at the Earth's surface, $R_E = 6371$ km is the radius of the Earth, $\mathbf{r}$ is the radial vector (magnitude r and unit vector $\hat{\mathbf{r}}$), and ϑ is the colatitude (unit vector $\hat{\vartheta}$). The gradient of the magnetic field is then given by

$$\nabla B = -\frac{3B}{r}\left(\hat{\mathbf{r}}+\frac{\sin 2\vartheta}{1+3\cos^2\vartheta}\hat{\vartheta}\right). \tag{2.28}$$

If the magnetic field is taken to be approximately radial, then only the ϑ component of the gradient is significant, and it is small in the high latitude F-region ionosphere. The $\nabla_\perp B$ term can be

assumed to be approximately zero with little effect on the calculation of $J_{\parallel}$, as discussed by *Ruohoniemi et al.* [1989]. That leaves the curl term and the two conductivity gradient terms. *Boström* [1974] identified these three terms according to their origins:

$$J_{\parallel} = \overbrace{\Sigma_P \mathbf{B} \cdot (\nabla_{\perp} \times \mathbf{v}_{cnv})}^{\text{magnetospheric}} + \overbrace{(-\mathbf{E} \cdot \nabla_{\perp} \Sigma_P) + B\mathbf{v}_{cnv} \cdot \nabla_{\perp} \Sigma_H}^{\text{ionospheric}}; \tag{2.29}$$

that is, one term that depends on magnetospheric dynamics through the convective drift velocity, and two terms that depend on ionospheric structure through conductivity gradients.

The ionospheric terms are set to zero within this work in the manner of, for example, *Sofko et al.* [1995] and *McWilliams* [1997]. The spatial scales in the ionosphere that are studied in this thesis are on the order of 100 km. The scale lengths of variations in the photo-induced Pedersen and Hall conductivities are considerably larger, meaning that the conductivity gradients are small compared to the velocity curl term. Shorter scale lengths occur in regions of particle precipitation. Any conductivity gradients on scales comparable to the velocity curl term would then be sources of error. They must be kept in mind when interpreting results, but are otherwise neglected in the development of the technique presented in this thesis.

When only the magnetospheric term of the FAC equation (2.29) is considered, the FAC depends on the curl term alone. The signatures of magnetospheric dynamics are thereby strongly linked to measurements of F region plasma velocity even when the ionospheric conductance is unknown. The estimations of FAC in this thesis begin with the approximation

$$\frac{J_{\parallel}}{\Sigma_P} \approx \mathbf{B} \cdot (\nabla_{\perp} \times \mathbf{v}_{cnv}) \,. \tag{2.30}$$

In Section 4.2, equation 2.30 is modified to make use of SuperDARN potential functions.

2.4.2 FAC Systems

Large-scale systems of FACs link the ionosphere and the magnetosphere. One such system, the region 1 FAC system, is illustrated in Figure 2.4. The region 1 FAC system consists of an upward (that is, away from the Earth) FAC flowing at the boundary of the polar cap on the duskside, a downward FAC at the boundary of the polar cap on the dawnside, a portion of the magnetopause currents, and an ionospheric Pedersen current flowing dawn to dusk across the polar cap. The iono-

spheric portion of the region 1 system is marked in Figure 2.10. Both Figure 2.4 and Figure 2.10 show that the region 1 FACs are located primarily within the ionospheric plasma convection cells.

Figure 2.10 also includes the region 2 FAC system, which consists of an upward FAC at the equatorward edge of the sunward return plasma flow on the dawnside, and a downward FAC in the same place on the duskside. The ionospheric portion of the region 2 system is made up of meridional Pedersen currents across the regions of sunward return plasma flow, located equatorward of the OCFLB, where the Pedersen currents flow parallel to the electric field. These Pedersen currents link the region 1 and region 2 FACs [*Cowley*, 2000]. The region 2 system is connected to the ring current that flows westward around the Earth at equatorial latitudes (shown in Figure 1.1).

Iijima and Potemra [1976a] investigated the region 1 and 2 FACs using magnetometers on board the Triad satellite and produced the map shown here in Figure 2.15. The map shows the statistical locations and directions of the region 1 and region 2 FACs, as well as the higher-latitude noon sector FACs sometimes called Region 0 (see, for example, *Eriksson et al.* [2002]). The region 1 FACs are visible as the most poleward of the bands (with the exception of the three-box strip at magnetic noon) and region 2 FACs are visible as the most equatorward of the bands. The three-box strip at magnetic noon constitutes what is known as the Region 0 FAC. Region 0 FACs are associated with the cusp, the funnel-shaped part of the magnetopause between the dayside closed field region at lower latitudes and the lobe field at higher, including polar, latitudes. The northern cusp is visible in Figure 1.1.

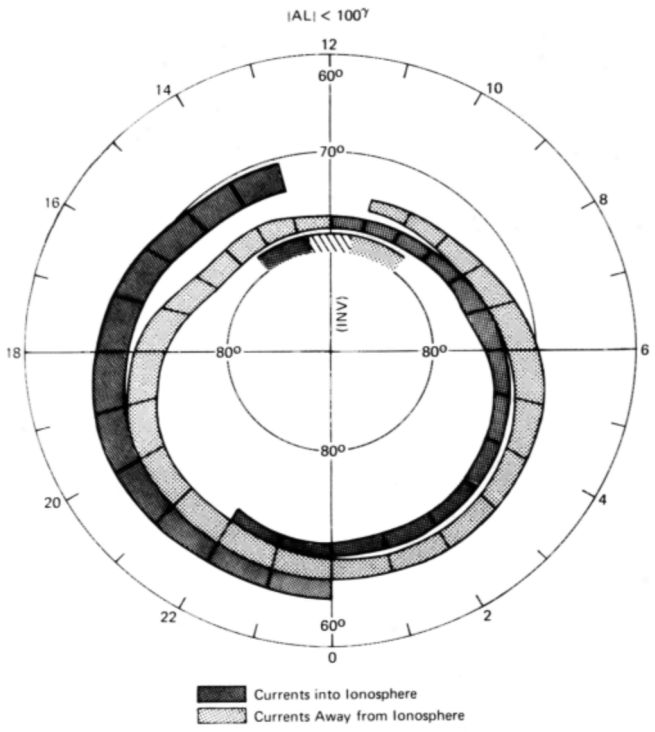

Figure 2.15: Statistical plot of FAC distribution from *Iijima and Potemra* [1976a], measured using Triad satellite magnetometers and projected onto the ionosphere in MLT and MLAT coordinates. Upward and downward FACs are plotted as light and dark boxes, respectively, and the hatched box at magnetic noon represents currents of variable sense.

CHAPTER 3

INSTRUMENTS

3.1 SuperDARN

The Super Dual Auroral Radar Network (SuperDARN) is the primary instrument used for this thesis work. SuperDARN is a network of high frequency (HF) radars operated by an international scientific consortium [*Greenwald et al.*, 1995]. PolarDARN, a northward extension of the network by the Canadian SuperDARN team [*Chisham et al.*, 2007], improved radar coverage of the polar cap. During the time of the case study presented in Chapter 5 there were 21 stations in the northern hemisphere and 11 stations in the southern hemisphere, but more have subsequently been added. Those radars that were present during the case study period are listed in Table 3.1, and their fields of view are depicted in Figure 3.1.

The primary function of a SuperDARN radar is to determine the convective drift velocities ($\mathbf{v}_{cnv} = \mathbf{E} \times \mathbf{B}/B^2$) of plasma in the ionosphere by measuring the mean Doppler shifts of plasma irregularity structures. Because the density irregularities are embedded in the moving plasma, measurement of their convective drift velocity equates to measurement of the bulk plasma convective drift motion in the ionosphere, motion that is driven by magnetospheric dynamics. The large extent of the radar coverage allows plasma motion to be mapped throughout the northern and southern hemispheres, providing information that is used to study global plasma flow patterns, such as those examined in this thesis.

Because the vector magnetic field **B** is well known at ionospheric altitudes, measured plasma convective drift velocities can be converted to the vector electric field **E**, which would otherwise

Table 3.1: SuperDARN sites during the case study period of 31 May–1 June 2013[a]

Name	Code	Geographical (°)			Magnetic (°)		
		Latitude	Longitude	Boresight	Latitude	Longitude	Boresight
Northern hemisphere sites							
Adak West	adw	51.9	-176.6	-28.0	47.8	-111.9	-32.9
Adak East	ade	51.9	-176.6	46.0	47.8	-111.9	30.3
King Salmon	ksr	58.7	-156.7	-20.0	57.7	-97.9	-30.0
Kodiak	kod	57.6	-152.2	30.0	57.4	-93.6	12.4
Inuvik	inv	68.4	-133.8	29.5	71.7	-83.6	8.3
Prince George	pgr	54.0	-122.6	-5.0	59.6	-62.9	-14.9
Christmas Valley West	cvw	43.3	-120.4	-20.0	49.3	-57.1	-29.7
Christmas Valley East	cve	43.3	-120.4	54.0	49.3	-57.1	41.1
Saskatoon	sas	52.2	-106.5	23.1	60.8	-42.5	17.6
Fort Hays West	fhw	38.9	-99.4	-25.0	48.5	-31.0	-32.0
Fort Hays East	fhe	38.9	-99.4	45.0	48.5	-31.0	42.9
Rankin Inlet	rkn	62.8	-92.1	5.7	72.5	-23.2	2.7
Kapuskasing	kap	49.4	-82.3	-12.0	59.7	-7.1	-13.0
Blackstone	bks	37.1	-78.0	-40.0	47.4	-1.6	-41.0
Wallops Island	wal	37.9	-75.5	35.9	48.0	1.9	45.5
Clyde River	cly	70.5	-68.5	-55.6	78.6	18.7	-43.2
Goose Bay	gbr	53.3	-60.5	5.0	60.8	23.5	10.7
Stokkseyri	sto	63.9	-21.0	-59.0	64.8	67.1	-34.6
Þykkvibær	pyk	63.8	-20.5	30.0	64.6	67.4	40.1
Hankasalmi	han	62.3	26.6	-12.0	59.4	104.9	1.6
Hokkaido	hok	43.5	143.6	30.0	37.3	-143.9	27.3

Table 3.1: SuperDARN sites during the case study period of 31 May–1 June 2013[a] (continued)

Name	Code	Geographical (°)			Magnetic (°)		
		Latitude	Longitude	Boresight	Latitude	Longitude	Boresight
Southern hemisphere sites							
Halley	hal	-75.5	-26.6	165.0	-62.5	29.9	176.0
SANAE	san	-71.7	-2.9	173.2	-62.2	44.3	-162.1
Syowa South	sys	-69.0	39.6	165.0	-66.9	72.6	-152.0
Syowa East	sye	-69.0	39.6	106.5	-66.9	72.6	144.2
Kerguelen	ker	-49.4	70.3	168.0	-58.9	123.9	-164.2
Zhongshan Station	zho	-69.4	76.4	72.5	-75.2	97.7	123.0
South Pole Station	sps	-90.0	118.3	75.7	-74.4	19.2	-112.9
Dome C East	dce	-75.1	123.3	115.0	-88.9	50.4	-100.3
TIGER	tig	-43.4	147.2	180.0	-54.5	-132.5	169.7
McMurdo	mcm	-77.9	166.7	263.4	-80.0	-31.9	173.5
Unwin	unw	-46.5	168.4	227.9	-54.3	-105.5	-152.3

[a] Sites are listed in order of geographic longitude, west to east. Boresight is the centreline of the radar's look direction and is measured positive east of north.

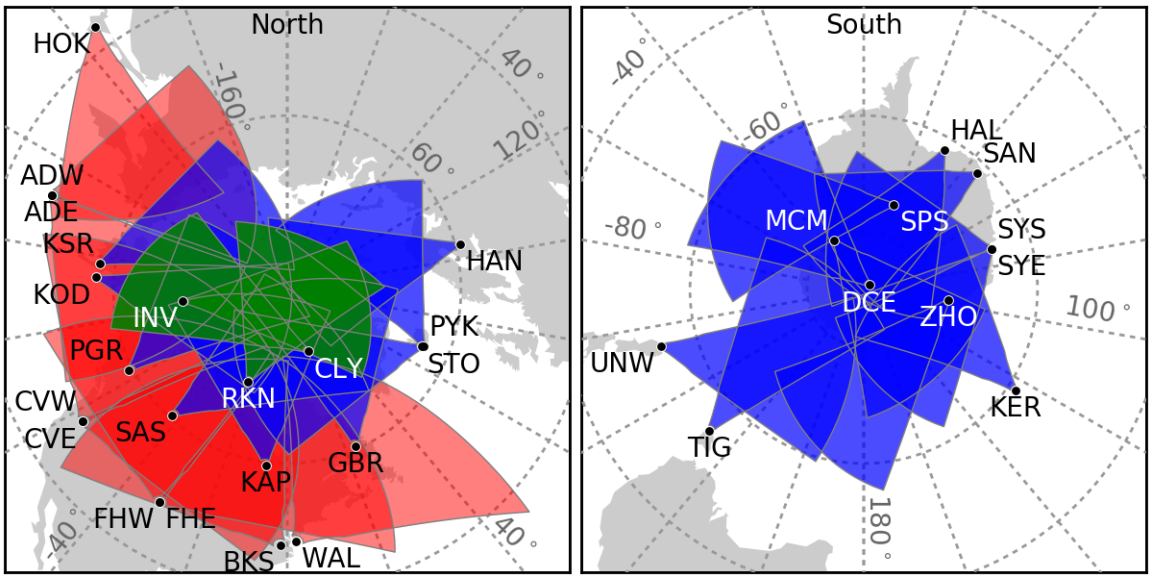

Figure 3.1: The fields of view of all SuperDARN radars operational during the case study period of 31 May–1 June 2013, plotted in magnetic invariant coordinates. The northern hemisphere radars are shown at left with mid-latitude radars in red, high-latitude in blue, and polar cap (PolarDARN) in green. The southern hemisphere radars are shown at right in blue.

be difficult to measure. Knowledge of **E** in the ionosphere is important for studies of FAC systems because the systems primarily close through the ionosphere as Pedersen currents (flowing parallel to **E**).

3.1.1 Refraction and Scattering

A SuperDARN radar operates in the HF radio band (3 MHz to 30 MHz) and is capable of operating at frequencies between 8 MHz and 20 MHz. An important feature of the HF band is its over-the-horizon propagation. At HF frequencies, refraction of radio waves by ionospheric plasma is significant. The index of refraction n of a plasma is given by the Appleton–Hartree equation [*Appleton*, 1925; *Hartree*, 1931]:

$$n^2 \approx 1 - \frac{N_e e^2}{4\pi^2 m_e \varepsilon_0 f^2} \tag{3.1}$$

(in the high-frequency limit), where N_e is the electron number density, m_e is the electron mass, e is the electron charge, ε_0 is the permittivity of free space, and f is the radio transmitter frequency. For frequencies in the HF band, a large enough electron density N_e will cause n to be appreciably less than unity, such that radio waves entering the ionosphere from below are refracted toward the

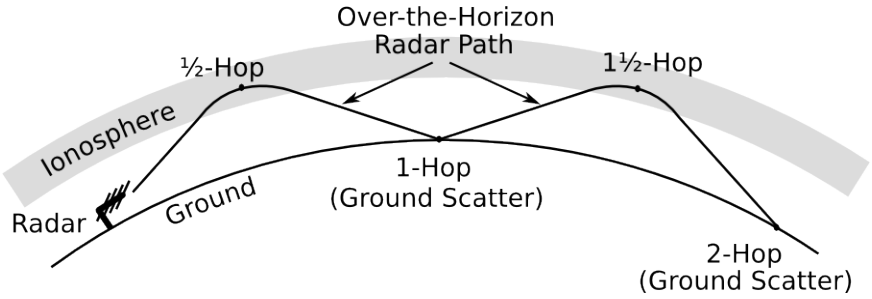

Figure 3.2: Over-the horizon propagation of a radio wave that is refracted by the ionosphere and scattered by the ground.

ground.

The effect of $n < 1$ allows the radar field of view to extend well over the horizon, as shown schematically in Figure 3.2. A radio wave travelling outward from the radar propagates to ionospheric heights, refracts toward the ground, scatters from the ground, and propagates toward the ionosphere again. Each segment of the propagation path beginning and ending at the ground is called a "hop." When a radio wave is scattered by plasma density irregularities or by the ground, some of the incident energy is scattered backwards along the path travelled by the incident wave and is received by the radar. This backscatter can occur in plasma at half of a hop, at the ground at one hop, in plasma again at one and one-half hops, and so on until the return signal becomes too weak to measure.

The mass difference between electrons and ions means that, to a first approximation, only the ionospheric electrons are affected by a radio wave passing through the plasma. The electrons oscillate in space with the oscillating radio wave electric field. The plasma frequency ω_p is the characteristic oscillation frequency of the plasma's electrons when they are perturbed, and is given by

$$\omega_p^2 = \frac{N_e e^2}{m_e \varepsilon_0}. \tag{3.2}$$

The plasma frequency may also be written f_p, such that $\omega_p = 2\pi f_p$. A radio wave of frequency f entering the plasma will be reflected by the plasma if $f < f_p$ and transmitted through the plasma if $f > f_p$. When a transmitted wave propagates through the plasma, if there is a density irregularity structure within the plasma, the irregularity will consist of high-to-low density gradients from which some of the incident radio power will be reflected. The reflected power from a single density irregularity is small, but there are many density irregularities in a turbulent region of the

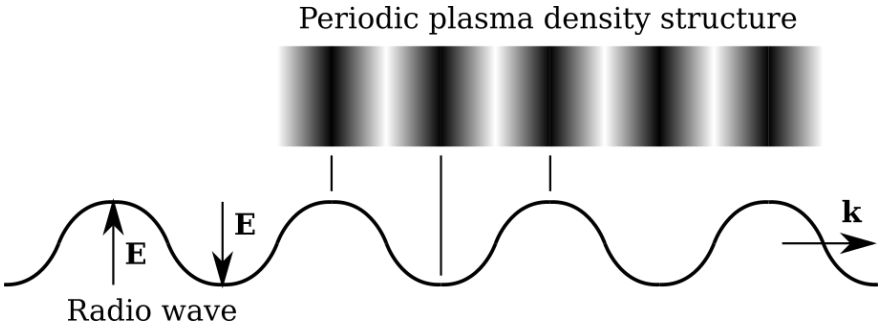

Figure 3.3: The electric field **E** of a propagating radar wave (with wavevector **k**) and a periodic density structure in a plasma, demonstrating the alignment of their wavelengths necessary for coherent scatter. The density structure has a wavelength half that of the radio wave.

ionosphere. Because of the turbulence there will be a variety of spacing distances between the density irregularities, and periodic spacing may occur. Should the wavelength of a periodic plasma density structure equal half of the radio wavelength (tens of meters for SuperDARN), constructive interference will result, and the reflected power can be sufficient to be detected by the radar receiver. This process is called coherent scatter, and it is analogous to Bragg scattering in a crystal. Figure 3.3 shows a sketch of wavelength alignment between the electric field of a radio wave and a periodic plasma density structure.

3.1.2 Radar Operation

SuperDARN uses a monostatic radar design, meaning the same antenna array is used for transmitting and receiving. The array itself consists of a line of 16 antennas, each of which has a dedicated transmitter, power amplifier, and receiver. Transmitting the same signal from all of the antennas produces an interference pattern, similar to light passing through a diffraction grating. When the signal is transmitted in phase from all of the antennas, a narrow beam is directed in the "boresight" direction (that is, normal to the array), compared to the broad beam pattern of an individual antenna. The diffraction grating effect also produces lower power "sidelobes" to the left and right of the main lobe, or beam.

The main beam of the array can also be directed left or right of boresight by introducing a phase shift to the signal that varies linearly with antenna position, as shown in Figure 3.4. The phase shift applied to the signal at antenna n is $n\Delta\varphi$ for the basic shift of $\Delta\varphi = kd\sin\vartheta$ for antenna

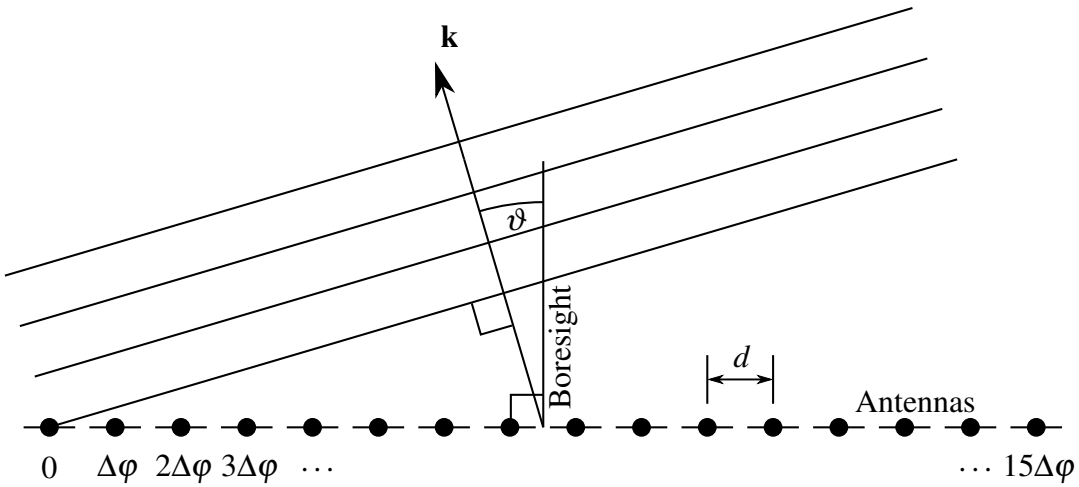

Figure 3.4: Phasing an antenna array with antenna spacing d by applying phase shifts of integer multiples of $\Delta\varphi$ to steer the main beam direction an angle ϑ from boresight (array normal). The radar wavevector is denoted **k** and the antennas are shown along the bottom of the diagram.

spacing d, wavevector magnitude k, and beam direction ϑ (measured relative to boresight). This configuration for steering the radar beam is called a phased array. The beam may be pointed in any azimuthal direction, with its achievable angular resolution limited only by the phasing element of the system. In practice, a typical SuperDARN radar uses 16 to 24 fixed beam directions spaced 3.24° apart, scanning across the field of view through sequential beams over a duration of one to two minutes.

SuperDARN radars operate as pulsed radars, transmitting multi-pulse sequences such as the Katscan sequence shown in Figure 3.5. The timing of the pulses is designed so that a wide range of lag time intervals can be obtained by choosing pairs of pulses from the sequence. The lag times are integer multiples of a fundamental lag time τ. This technique is called pulse coding, and is a way of obtaining received signals from only the desired range.

A range–time diagram for a simple two-pulse sequence is presented in Figure 3.6 to demonstrate pulse coding. The transmitted signal line (Tx) shows that the two pulses, which have finite width, are transmitted at times t_0 and $t_1 = t_0 + \tau$ (for lag time τ). The pulses travel outward from the radar at the speed of light c and are back-scattered from plasma density structures in the darker-coloured intersections of the diagonal lines. At time $t_2 = t_0 + 2R/c$ the echo of the first pulse from the desired range R is received, but the received signal also contains what is called a "clutter" echo of the second pulse from the nearer range R_n. At time $t_3 = t_1 + 2R/c$ the echo of the second pulse

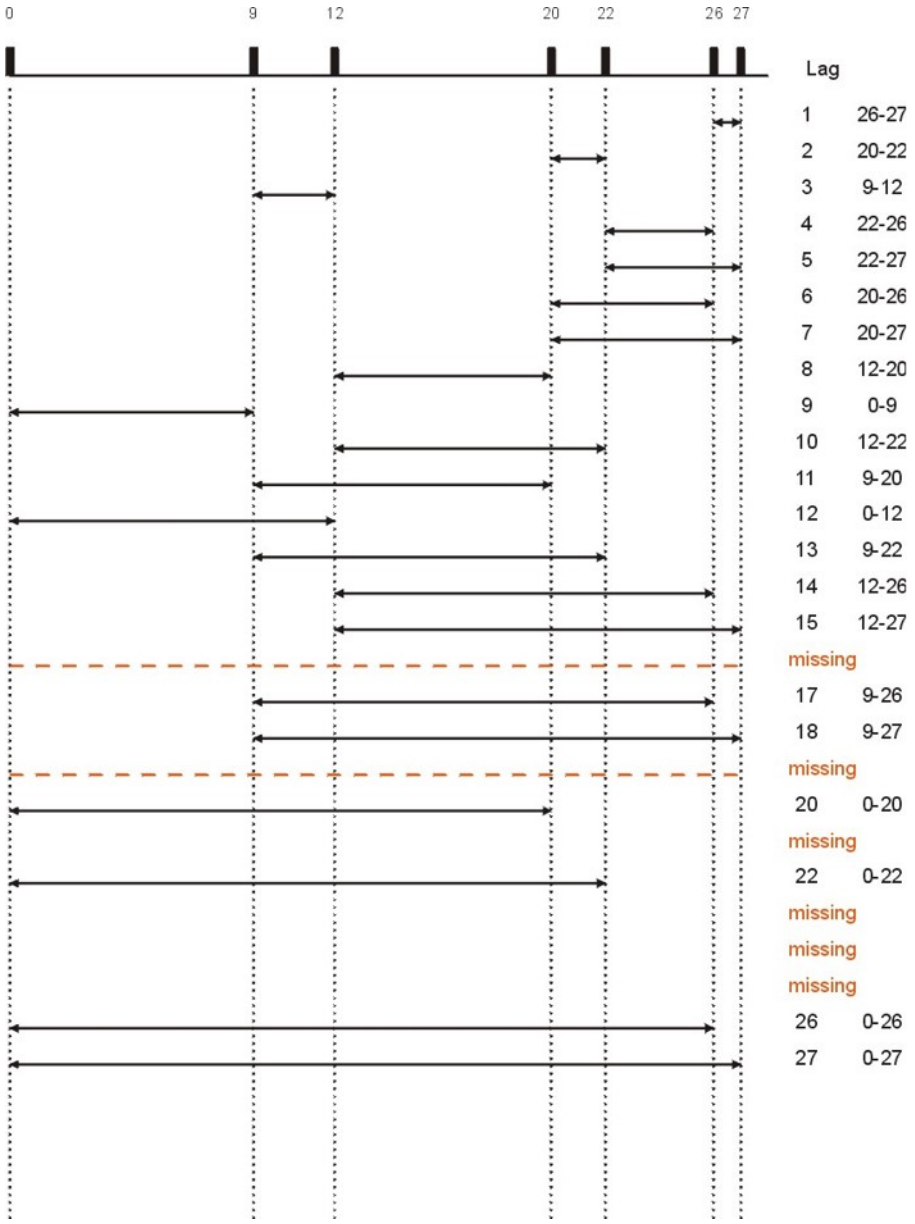

Figure 3.5: The Katscan pulse sequence. The pulses are marked by vertical bars at the top of the figure along a time axis, and are labelled according to the number of fundamental lag times τ elapsed at the transmission of each pulse. Analysis lag intervals are listed below the pulse sequence from 1 (τ) to 27 (27τ), and the pulse pairs used to obtain the lag intervals are noted (according to the number of τ elapsed, as at the top) and shown graphically with arrowed lines. The intervals that are not available from this sequence are marked as missing. From *McWilliams* [2001].

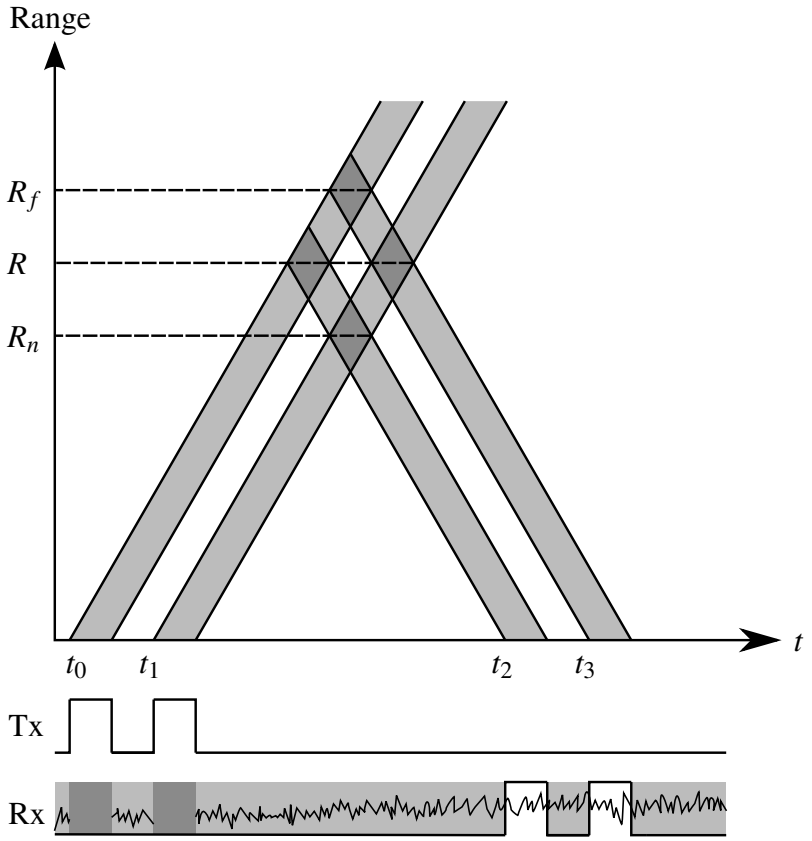

Figure 3.6: Farley diagram (range–time diagram) of a simple two-pulse sequence with transmitted (Tx) and received (Rx) signals. Range R is the range being studied. R_n is a nearer undesired range and R_f is a farther undesired range. Time t begins an arbitrary interval before the first pulse is transmitted at time t_0.

from R is received, as well as a clutter echo of the first pulse from the farther range R_f. As shown by the received signal line (Rx), the received signal is masked (light grey and heavy black line) with the same pattern as the transmitted pulse sequence. Only times corresponding to the reception of the echo pulses at t_2 and t_3 are used in the analysis of signals from range R. (The dark grey blocks in the Rx line show where the received signal is cut off, or "blanked," during transmission of the pulses to avoid damaging the radio receiver with excessive power. This is a necessary operational constraint for monostatic radar systems—that is, when the same antenna is used to transmit and receive.)

To remove the clutter echoes from the received signal, the complex autocorrelation function (ACF) of each possible received-signal pulse pair in the pulse sequence (with their various intervening lag times) is calculated. (For the simple two-pulse sequence there is only one such

pair.) Signals from plasma structures at range R are expected to be well-correlated with each other (within the beam width, the radio bandwidth, and a handful of τ) but poorly correlated with signals from plasma structures at range R_n and range R_f, meaning only signals received from R should constructively correlate. Each pulse pair contributes the ACF value for its lag time. The ACF is expressed as a discrete function of lag times, which are integer multiples of the fundamental lag time τ. It can be shown [e.g., *Woodman and Hagfors*, 1969] that the time derivative of the phase φ of the complex ACF is given by

$$\frac{d\varphi}{dt} = 2\pi f_D, \tag{3.3}$$

where t is time and f_D is the Doppler shift. The Doppler shift, calculated from the time derivative of the ACF phase, is then used to calculate the line-of-sight (l-o-s) velocity component of the periodic plasma density structures at range R according to the equation for Doppler shift:

$$f + f_D = \frac{cf}{c - v}, \tag{3.4}$$

where f is the radar transmitter frequency, c is the speed of light, and v is the l-o-s speed (positive toward the radar receiver). The measured l-o-s velocity at range R in the radar's beam direction is equated with the l-o-s component of the bulk plasma convective drift velocity at that location.

The complex ACF of the received signal at range R can be used to study parameters of the plasma besides Doppler shift. The ACF as a function of time is converted via a Fourier transform to the ACF as a function of frequency. Functional fitting of the ACF makes it possible to determine, for example, the power received from range R, the spectral width of the distribution, and the correlation length and time of the plasma density structures being measured [*Villain et al.*, 1996]. Also, in SuperDARN data, if the received signal from range R has a velocity less than 30 m/s and a spectral width less than 60 m/s (when expressed in velocity units) it is classified as ground scatter. (The rationale is that the ground moves slowly and is a source of highly coherent echoes. Note that the ground includes surface water.)

SuperDARN radio receivers use a method called quadrature detection [e.g., *Wehner*, 1987], in which the received signal is divided into two equal parts and a 90° phase shift is applied to one of the parts. The resulting "in-phase" (unaltered) and "in-quadrature" (phase-shifted) signals provide the full complex received signal. The complex ACF of the received signal at any available range R can then be calculated from the component signals.

Data from a single SuperDARN radar are conveniently viewed in a field-of-view plot, as shown in Figure 3.7, displaying measured parameters along with their azimuth and range information. In the example of Figure 3.7, a band of ground scatter (grey) is present across the field of view past range gate 30 (which represents a time-of-flight distance of 1530 km). Past range gate 40 (1980 km) there are small velocities toward and away from the radar (yellow and green) located across the central beams of the field of view, as well as fast away velocities (red) and fast toward velocities (dark blue) in the rightmost beams. Near range gate 50 (2430 km) more fast velocities are present, both toward (dark blue) and away (red), as well as some slower velocities (green, yellow, and orange). A slow toward velocity (green) is present at the centre of the far edge of the field of view. A mix of slow and fast velocities (toward and away) and ground scatter appears in the ranges nearest the radar.

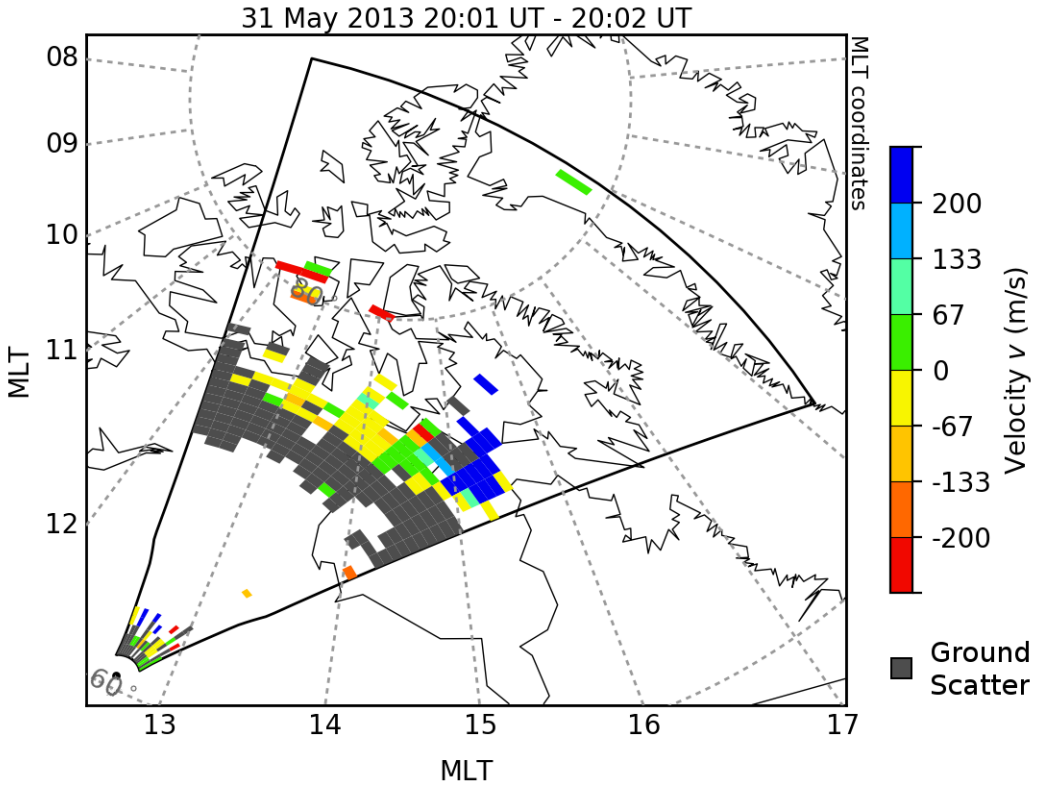

Figure 3.7: Line-of-sight velocity in the field of view of the Saskatoon SuperDARN radar in MLT–MLAT coordinates. The radar location, at the bottom left, is marked with a black dot. The field of view, outlined in black, is divided into 16 beams of 75 range cells each. A range cell with measured velocity is shown as a coloured block: yellow to red (negative) represent velocity away from the radar and green to blue (positive) represent velocity toward the radar. Grey blocks represent measured data classified as ground scatter. Lines of MLT and parallels of MLAT are shown as short-dashed grey lines, with 60° MLAT at the bottom of the plot and 80° MLAT near the top.

CHAPTER 4

METHODS

4.1 Convection Map Fitting

The primary goal of SuperDARN is to monitor ionospheric plasma motion on a global scale by combining data from multiple SuperDARN radars [*Greenwald et al.*, 1995]. The pairing of radars with overlapping fields of view is the origin of the word *Dual* in the SuperDARN acronym. With more than one radar covering a common viewing area, the velocity of drifting plasma structures can be observed from two different directions. The calculated resultant provides the vector velocity of the ionospheric plasma [*Greenwald et al.*, 1995]. *Ruohoniemi and Baker* [1998] developed a method to extend the coverage of the two-dimensional vector velocity determination beyond the regions of overlapping observations by combining data from all available radars using a fit of a scalar electrostatic potential function Φ to the velocity data. Their processing technique is implemented in the standard SuperDARN software package, the Radar Software Toolkit (RST), and the technique and its implementation are described in this section.

4.1.1 Data Preparation

The *Ruohoniemi and Baker* [1998] method uses an equal-area grid over the northern or southern hemisphere of the Earth, with cells measuring approximately 111 km$\times$111 km, or one degree of latitude square, as shown in Figure 4.1. Radar l-o-s velocity data are filtered and smoothed and then grouped by spatial grid cell, and an electrostatic potential function Φ is fitted to the gridded l-o-s velocities denoted $\mathbf{u}$. The equal-area grid is necessary to compensate for (1) the high spatial

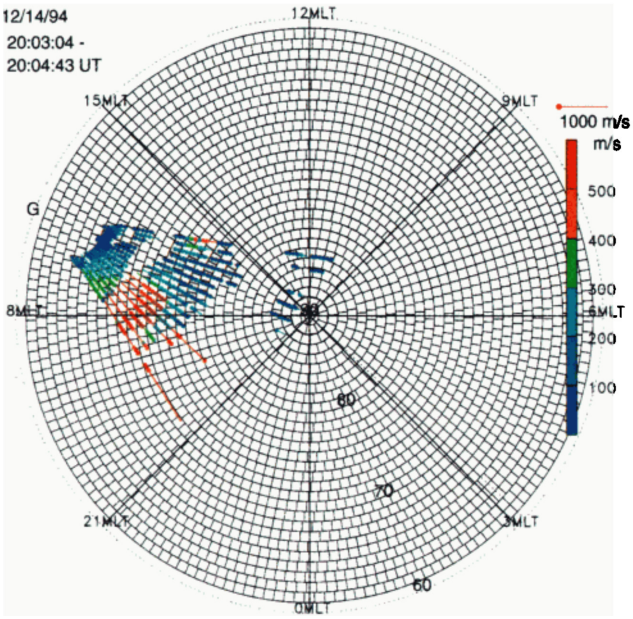

Figure 4.1: The grid used for processing l-o-s velocity vectors into fitted velocity vectors. A sample of SuperDARN data from the Goose Bay station is shown. Radial lines show magnetic local time (MLT) and magnetic latitudes are marked. From *Ruohoniemi and Baker* [1998].

sampling density in regions near SuperDARN stations where the radar beams are narrow and low sampling density in regions far from the stations where the beams are wide, and (2) to avoid the nonuniform cell widths that would arise if a constant angular longitudinal width were used (so that cells narrowed with increasing latitude).

A filter is applied to the SuperDARN data, proceeding site by site. Data elements with large estimated uncertainty or high probability of being ground scatter are discarded. *Ruohoniemi and Baker* [1998] imposed an upper bound of 200 m/s on the estimated uncertainty of the l-o-s velocity components. The SuperDARN ground scatter standard implemented in RST is that any data having both l-o-s velocity less than 30 m/s and spectral width less than 60 m/s are classified as ground scatter.

Next, for each SuperDARN site, the l-o-s velocity data are smoothed both spatially and temporally. Each radar's field of view is divided into cells by beam and range (not to be confused with the hemispheric-grid cells). Around each radar beam–range cell a 3×3 spatial grid is formed. The radar cell grid includes the central cell, the two adjacent range cells in the same beam, and the three corresponding cells in each of the two adjacent beams. The central cell is given a weight of four

and each of the surrounding cells is given a weight of two. The same nine cells in the preceding and following scans of the radar are then prepended and appended, although in these cases the central cell is given a weight of two and each surrounding cell is given a weight of one. The 27-point weighted median l-o-s velocity is calculated and assigned to the original central beam–range cell. If the assigned median l-o-s velocity is below the lower bound of 12 m/s used in RST, no velocity is assigned and the central beam–range cell is deemed empty.

The filtered, smoothed data from all of the SuperDARN radars within the hemisphere are grouped by hemispheric-grid cell. Within each grid cell, all of the l-o-s velocities from each radar are averaged to produce a resultant gridded l-o-s velocity $\mathbf{u}$ in each grid cell for each contributing radar.

Because of spatial gaps in the radar observations, an *a priori* model is needed to constrain the electrostatic potential fit. A model constructed from large ensemble averages of SuperDARN data measured over several years and classified according to IMF conditions is used. To determine the prevailing IMF conditions and extract the corresponding data from the model, IMF data are obtained from the NASA GSFC multi-satellite OMNI data set through the online OMNIWeb database (URL: https://omniweb.gsfc.nasa.gov). The data in the OMNI dataset are time-shifted to the nose (or sunward extreme) of the Earth's bow shock, a standing fluid shock in the solar wind plasma caused by the wind's flow around the magnetosphere. A time delay is applied to the OMNI IMF data (set to a constant of 10 minutes for this thesis work) to account for the propagation time from the bow shock nose to the dayside magnetopause, where the IMF reconnects with the geomagnetic field.

4.1.2 The Hemispheric Electric Potential

In the *Ruohoniemi and Baker* [1998] technique, the electric field $\mathbf{E}$ in the high-latitude ionosphere is assumed to be invariant with radial distance r, or

$$\mathbf{E} = \mathbf{E}(\vartheta, \varphi), \tag{4.1}$$

where ϑ is the polar angle or colatitude and φ is the azimuthal angle. The field is also assumed to be irrotational (so that the magnetic field is constant on sufficiently short time scales), meaning

that $\mathbf{E}$ can be expressed as the gradient of a scalar potential function $\Phi(\vartheta,\varphi)$:

$$\mathbf{E}(\vartheta,\varphi) = -\nabla\Phi(\vartheta,\varphi) = \begin{bmatrix} 0 \\ -\frac{1}{r}\frac{\partial}{\partial\vartheta} \\ -\frac{1}{r\sin\vartheta}\frac{\partial}{\partial\varphi} \end{bmatrix} \Phi(\vartheta,\varphi) = \begin{bmatrix} 0 \\ -\frac{1}{r}\frac{\partial}{\partial\vartheta}\Phi(\vartheta,\varphi) \\ -\frac{1}{r\sin\vartheta}\frac{\partial}{\partial\varphi}\Phi(\vartheta,\varphi) \end{bmatrix}. \tag{4.2}$$

The definition $\Phi = \Phi(\vartheta,\varphi)$ is based on the assumption that SuperDARN measurements all occur at approximately the same altitude, and on the near-radial orientation of the high-latitude magnetic field that is approximated as perfectly radial for the purposes of potential fitting. The lack of r-dependence in Φ means that $\mathbf{E} = -\nabla\Phi$ has no radial component, which is consistent with frozen-in flow, $\mathbf{E} = -\mathbf{v}\times\mathbf{B}$, and the radial magnetic field. The equivalent statement of the convective drift in equation 2.4 also supports the assumption of purely tangential velocity because of its requirement of $\mathbf{v}\perp\mathbf{B}$ and the vertical magnetic field. Because SuperDARN detects field-aligned plasma irregularities, the measured velocities and electric fields are perpendicular to the magnetic field as expected.

Ruohoniemi and Baker [1998] chose to represent Φ as a series of associated Legendre functions of the first kind, $P_l^m(\cos\vartheta')$, of order l and degree m. The angle ϑ' is a normalised polar angle given by

$$\vartheta' = \frac{\pi}{\frac{\pi}{2}-\Lambda_0}\vartheta, \tag{4.3}$$

where Λ_0 is the low-latitude boundary of the potential, such that ϑ' ranges from 0 to π. The normalisation is similar to that introduced by *De Santis* [1992] (who normalised to $\pi/2$) and allows Legendre polynomials of integer order and degree to be used, compared to the spherical cap harmonics fitting method of *Haines* [1985, 1988] that uses spherical harmonics of integer order and non-integer degree. The normalisation equates to a stretching of the convection pattern to cover an entire sphere before the fit is performed. For a potential, *Ruohoniemi and Baker* [1998] used the real part of a complex potential (found, for example, in *Jackson* [1975]), writing the potential Φ as

$$\Phi(\vartheta',\varphi) = \sum_{l=0}^{L}\left(A_{l0}P_l^0(\cos\vartheta') + \sum_{m=1}^{l}(A_{lm}\cos m\varphi + B_{lm}\sin m\varphi)P_l^m(\cos\vartheta')\right), \tag{4.4}$$

where A_{lm} and B_{lm} are real coefficients and L is the highest order of the fit. For computer implementation it is best to express associated Legendre functions in terms of Legendre polynomials using the definition of the associated Legendre function of the first kind,

$$P_l^m(x) = (-1)^m(1-x^2)^{\frac{m}{2}}\frac{d^m}{dx^m}P_l(x), \tag{4.5}$$

so that

$$\Phi(x,\varphi) = \sum_{l=0}^{L} \Bigg(A_{l0} P_l(x) + \sum_{m=1}^{l} (A_{lm}\cos m\varphi + B_{lm}\sin m\varphi)(-1)^m (1-x^2)^{\frac{m}{2}} \frac{d^m}{dx^m} P_l(x) \Bigg), \tag{4.6}$$

where the variable $x = \cos\vartheta'$ is introduced to simplify the expression. A Legendre polynomial, in turn, is given by [e.g., *Jackson*, 1975]

$$P_l(x) = \frac{1}{2^l l!} \frac{d^l}{dx^l} (x^2-1)^l. \tag{4.7}$$

4.1.3 Obtaining Plasma Velocity

When the electric field, given by equation 4.2, is combined with the geomagnetic field **B** in the convective drift equation 2.4, the plasma velocity **v** can be computed from Φ. **B** is approximated as dipolar:

$$\mathbf{B} = \frac{B_{polar}}{2} \frac{R_E^3}{r^3} \begin{bmatrix} -2\cos\vartheta \\ -\sin\vartheta \\ 0 \end{bmatrix}, \tag{4.8}$$

where $B_{polar} = 0.62 \times 10^{-4}$ T is the field magnitude at a pole of the Earth and $R_E = 6371$ km is the mean radius of the Earth. The magnitude of the field is

$$B = \frac{B_{polar}}{2} \frac{R_E^3}{r^3} \sqrt{3\cos^2\vartheta + 1}. \tag{4.9}$$

Inserting **E**, **B**, and B into equation 2.4, the result is

$$\mathbf{v} = \begin{bmatrix} v_r \\ v_\vartheta \\ v_\varphi \end{bmatrix} = \frac{4r^2}{B_{polar} R_E^3 (3\cos^2\vartheta + 1)} \begin{bmatrix} -\frac{\sin\vartheta}{2} \frac{\partial}{\partial\varphi}\Phi \\ \frac{1}{\tan\vartheta} \frac{\partial}{\partial\varphi}\Phi \\ -\cos\vartheta \frac{\partial}{\partial\vartheta}\Phi \end{bmatrix}. \tag{4.10}$$

At high latitudes $\sin\vartheta/2$ is small, supporting the assumption that the velocity measured by SuperDARN radars has a negligible radial component.

4.1.4 Fitting the Potential

Fitting a potential function, and the resulting fit velocities $\mathbf{v}$, to the gridded velocities $\mathbf{u}$ is achieved by minimising χ^2 through singular value decomposition [e.g., *Press et al.*, 1992]. The parameter χ is defined by

$$\chi^2 = \sum_{i=1}^{N} \frac{1}{\sigma_i^2} \left(\mathbf{v}_i \cdot \hat{\mathbf{u}}_i - u_i \right)^2, \tag{4.11}$$

where $\mathbf{u}_i$ is the ith of N gridded velocities, $\mathbf{v}_i$ is the corresponding ith velocity of N velocities calculated using equation 4.10, σ_i is the uncertainty in gridded velocity $\mathbf{u}_i$ (further discussed in *Ruohoniemi and Baker* [1998]), and $\hat{\mathbf{u}}_i$ and u_i are the direction and magnitude of $\mathbf{u}_i$, respectively.

Shepherd and Ruohoniemi [2000] changed the equatorward boundary of the convection pattern, where plasma velocity is set to zero, from a circular boundary to the Heppner–Maynard boundary (HMB). *Heppner and Maynard* [1987] found that the edge of the convection pattern is mostly circular but with a poleward perturbation on the dayside as shown in Figure 4.2. The shape is maintained through varying geomagnetic activity levels, but the boundary expands equatorward as geomagnetic activity increases. *Shepherd and Ruohoniemi* [2000] define a family of HMB curves and choose the curve that contains nearly all gridded data with velocity over a set threshold. The SuperDARN standard implemented in RST is to use the lowest-latitude curve at which three or more gridded velocities of at least 100 m/s are present.

When the fitting is completed, the set of coefficients of the potential A_{lm} and B_{lm} are given as output by the RST software, along with the gridded velocities and statistical model velocities, their locations, the IMF conditions used, the order of the fit, the location of the HMB, and some other relevant information.

4.1.5 Fit Velocity and True Velocity

The potential-derived velocity field $\mathbf{v}$, or the fit velocity, can be calculated over the hemispheric grid area from the coefficients to produce a fitted convection velocity map. An example of such a map, also including contours of the potential, the HMB, and the IMF conditions applied to the fitting, is shown in Figure 4.3. The map shows the potential contours (as solid and dashed curves, denoting positive and negative potential, respectively) and the resulting fitted plasma velocity field (as colour-coded barbs) at grid cells where the fit is constrained by measured SuperDARN data. A

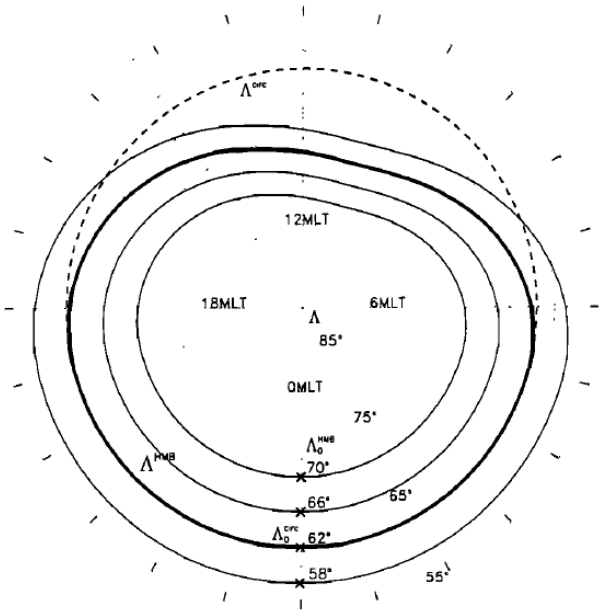

Figure 4.2: A family of Heppner–Maynard boundary curves plotted in MLAT–MLT coordinates. From *Shepherd and Ruohoniemi* [2000].

two-cell convection pattern can be seen in the plasma flow vectors and the potential contours, with the dusk cell centred at approximately 75° MLAT and 18:30 MLT.

On a given map, the fitted velocity vectors are generally reliable only in areas where the fit is constrained by measured, gridded data, and for this reason only fitted vectors at the same coordinates as the gridded vectors are plotted. However, it is possible even then that the fitted vectors differ greatly from the l-o-s measurements by the radars because of close spacing of divergent data from different radars, lack of widespread favourable radar scattering conditions that leads to heavy dependence on the statistical model, or peculiarities of the data from any of the radars (for example, contamination by E-region or meteor scatter). Therefore, the "true vector" (or true velocity) parameter is introduced in SuperDARN convection fitting. The component of the fitted velocity $\mathbf{v}$ that is perpendicular to the gridded l-o-s vector $\mathbf{u}$ is added to the gridded vector to produce a modified resultant, the true vector $\mathbf{v}_t$:

$$\mathbf{v}_t = \mathbf{u} + \hat{\mathbf{u}} \times (\mathbf{v} \times \hat{\mathbf{u}}) \,. \tag{4.12}$$

True vectors have closer connections to the measured l-o-s velocities than purely fitted vectors have in cases where the *a priori* model dominates a fit, but true vectors still take fitting into account so the large-scale combination of multiple radars is not ignored. Examination of true vectors may re-

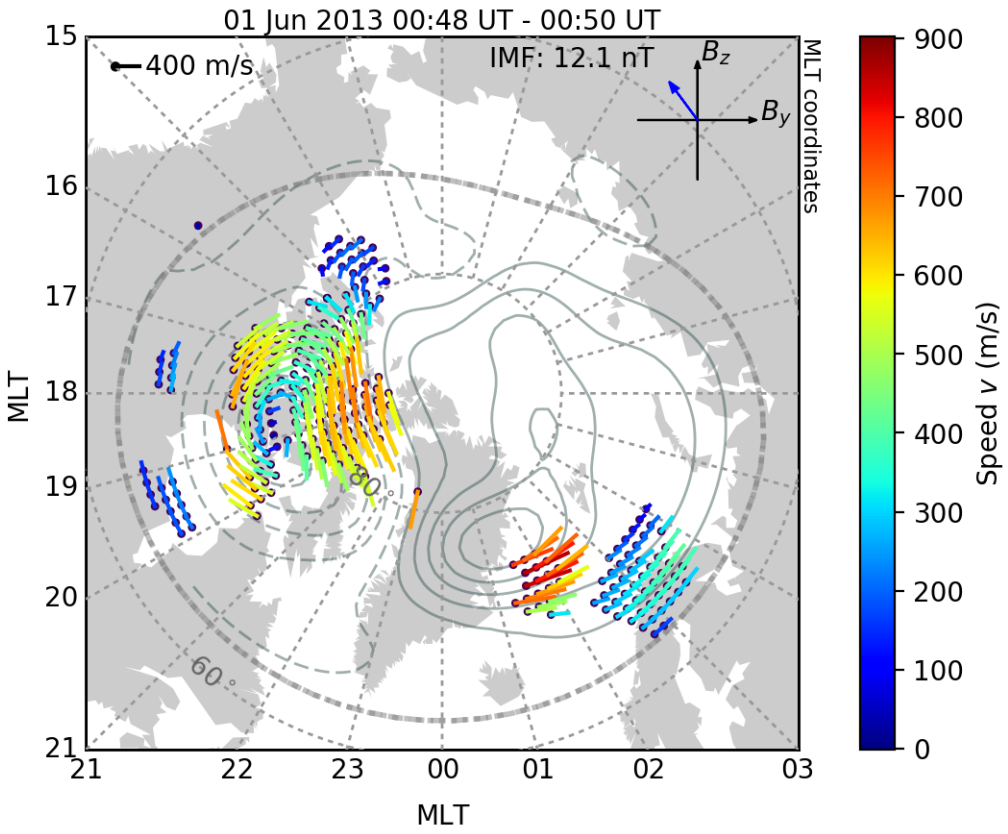

Figure 4.3: A sample SuperDARN convection map in magnetic coordinates, including MLAT and MLT. This example, from the 00:48 universal time (UT) to 00:50 UT interval on 1 June 2013, used a sixth-order Legendre polynomial fit. Plasma velocities are shown as coloured barbs originating in black circles (which mark the locations of the fitted vectors) and pointing in the direction of flow, with both barb length and colour corresponding to speed. A sample scale vector of length 400 m/s is shown in the upper left corner of the plot. The colour bar at the right shows the colour scale of the speed. The contours of the electrostatic potential are shown as solid (positive potential) and long-dashed (negative potential) curves. The HMB is shown as a heavy dotted line. Circles of magnetic invariant latitude (at 60° MLAT and 80° MLAT) and lines of MLT are shown as short-dashed lines, and the MLT lines are labelled at the edges of the map. The IMF conditions at the dayside magnetopause are shown in the upper right corner of the figure: the IMF projection on the GSM y–z plane is plotted and the magnitude of the projection is annotated along the top of the map.

veal regions of fitting inconsistent with the original data—visible as vectors that differ widely from their neighbours or from the fitted convection pattern—which suggest the fit may not be reliable in those areas and therefore greater care must be taken when making physical interpretations.

4.2 Estimating FAC Using the Potential

As discussed in Section 2.4.1, estimations of $J_{\parallel}/\Sigma_P$ can be made using equation 2.30 if the curl of velocity (specifically, the component perpendicular to the magnetic field) can be found. This approach was used by *Sofko et al.* [1995] and *McWilliams* [1997], for example, and a diagram of the configuration used by *McWilliams* [1997] is shown in Figure 4.4. In this technique, Stokes' theorem is used to obtain the plasma flow vorticity in a cell formed by overlapping SuperDARN beams. Stokes' theorem can be stated:

$$\int_S d\mathbf{a} \cdot (\nabla \times \mathbf{v}) = \oint_{\partial S} d\mathbf{l} \cdot \mathbf{v}, \tag{4.13}$$

for a vector quantity $\mathbf{v}$ over a surface S (where $d\mathbf{a}$ and $d\mathbf{l}$ represent infinitesimal area and length elements, respectively, and ∂S is the boundary of S). Although the Stokes' theorem technique is effective, it is limited by its requirements of overlapping SuperDARN fields of view and of measured velocity data sufficient to perform an integration around the boundary of each radar beam intersection cell, and is somewhat time-consuming and difficult to automate. An adapted version of the Stokes' theorem technique is described in Section 4.3.

In contrast to the Stokes' theorem method, this thesis takes a new approach: calculating FAC estimates directly from the SuperDARN fitted potential function Φ. This method takes advantage of the fast-cadence potential function output from SuperDARN, the spatial coverage and resolution of SuperDARN, and the ability of the SuperDARN fitting technique to operate using sparse measured data. Calculations directly from the potential also have the advantages of being computationally faster and more easily automated than the Stokes' theorem method.

When using the potential, it is convenient to return to equation 2.19 rather than to calculate the plasma flow vorticity. Neglecting the conductivity gradients and the divergence of the Hall current (all of which are small, as previously established), then

$$\frac{J_{\parallel}}{\Sigma_P} \approx -\nabla_{\perp} \cdot \mathbf{E}. \tag{4.14}$$

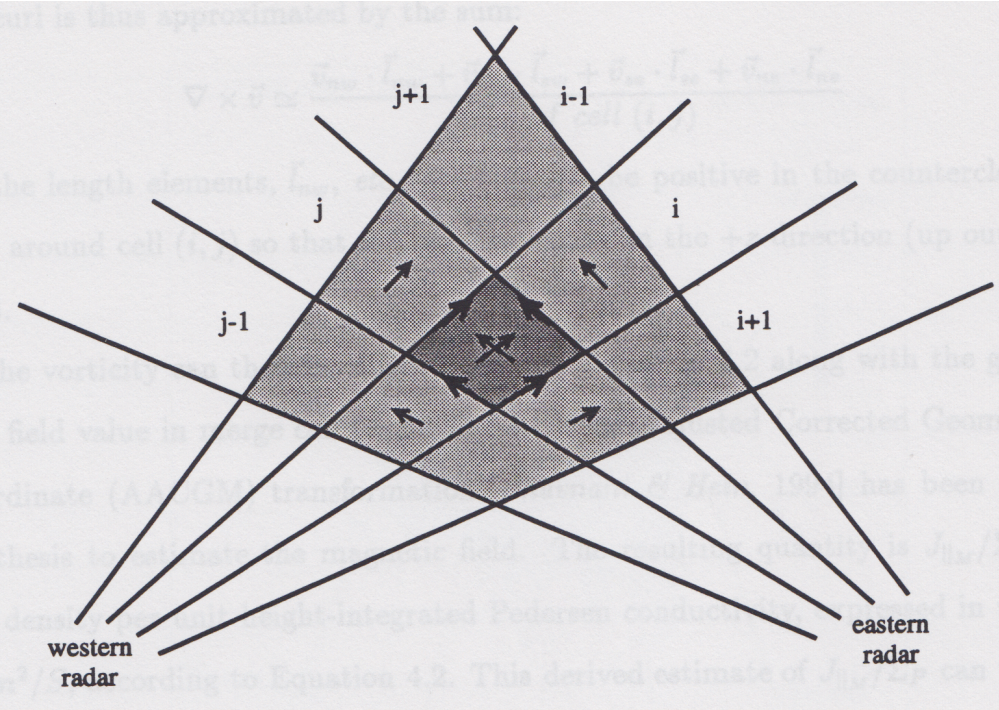

Figure 4.4: Plasma flow vorticity measurement configuration from *McWilliams* [1997]. The lines radiating from the radars represent the radar beam edges and shaded areas represent the beam intersection cells. Arrows represent plasma flow velocities. The indices i and j refer to the beam numbers of the western and eastern radars, respectively.

Using the electrostatic potential Φ and dropping the $\perp$ sign,

$$\frac{J_\parallel}{\Sigma_P} \approx -\nabla\cdot\mathbf{E} = -\nabla\cdot(-\nabla\Phi) = \nabla^2\Phi. \tag{4.15}$$

The Laplacian can be expanded to yield the FAC estimate in terms of the potential:

$$\begin{aligned}\frac{J_\parallel}{\Sigma_P} &\approx \frac{1}{r^2}\frac{\partial}{\partial r}\left(r^2\frac{\partial}{\partial r}\Phi\right) + \frac{1}{r^2\sin\vartheta}\frac{\partial}{\partial\vartheta}\left(\sin\vartheta\,\frac{\partial}{\partial\vartheta}\Phi\right) + \frac{1}{r^2\sin^2\vartheta}\frac{\partial^2}{\partial\varphi^2}\Phi \\ &\approx \frac{1}{r^2\sin\vartheta}\left(\cos\vartheta\,\frac{\partial}{\partial\vartheta}\Phi + \sin\vartheta\,\frac{\partial^2}{\partial\vartheta^2}\Phi + \frac{1}{\sin\vartheta}\,\frac{\partial^2}{\partial\varphi^2}\Phi\right).\end{aligned} \tag{4.16}$$

Equation 4.16 requires derivatives of the potential Φ with respect to ϑ and φ. For ϑ it is first necessary to find derivatives with respect to ϑ'. By inspection, these will have the same form as equation 4.4 but with $P_l^m(\cos\vartheta')$ replaced by a corresponding derivative:

$$\begin{aligned}\frac{\partial}{\partial\vartheta'}P_l^m(x) &= \frac{\partial}{\partial\vartheta'}x\frac{\partial}{\partial x}P_l^m(x) \\ &= -\sin\vartheta'\frac{\partial}{\partial x}P_l^m(x) \\ &= -\sqrt{1-x^2}P_l'^m(x),\end{aligned} \tag{4.17}$$

where $P_l'^m(x) = \frac{\partial}{\partial x}P_l^m(x)$, and

$$\begin{aligned}\frac{\partial^2}{\partial\vartheta'^2}P_l^m(x) &= -\cos\vartheta'\frac{\partial}{\partial x}P_l^m(x) - \sin\vartheta'\frac{\partial}{\partial\vartheta'}x\frac{\partial^2}{\partial x^2}P_l^m(x) \\ &= -\cos\vartheta'\frac{\partial}{\partial x}P_l^m(x) + \sin^2\vartheta'\frac{\partial^2}{\partial x^2}P_l^m(x) \\ &= -xP_l'^m(x) + (1-x^2)\frac{\partial^2}{\partial x^2}P_l^m(x).\end{aligned} \tag{4.18}$$

Using equation 4.5, the first derivative in x of $P_l^m(x)$ (that is, $P_l'^m(x)$) can be written

$$\begin{aligned}\frac{\partial}{\partial x}P_l^m(x) = P_l'^m(x) &= (-1)^m\frac{m}{2}(1-x^2)^{\frac{m}{2}-1}(-2x)\frac{d^m}{dx^m}P_l(x) \\ &\quad + (-1)^m(1-x^2)^{\frac{m}{2}}\frac{d^{m+1}}{dx^{m+1}}P_l(x) \\ &= -\frac{mx}{1-x^2}(-1)^m(1-x^2)^{\frac{m}{2}}\frac{d^m}{dx^m}P_l(x) \\ &\quad + (-1)^{m+1-1}(1-x^2)^{\frac{m+1}{2}-\frac{1}{2}}\frac{d^{m+1}}{dx^{m+1}}P_l(x) \\ &= -\frac{mx}{1-x^2}P_l^m(x) + \frac{(-1)^{m+1}}{-1}\frac{(1-x^2)^{\frac{m+1}{2}}}{\sqrt{1-x^2}}\frac{d^{m+1}}{dx^{m+1}}P_l(x) \\ &= -\frac{1}{\sqrt{1-x^2}}\left(\frac{mx}{\sqrt{1-x^2}}P_l^m(x) + P_l^{m+1}(x)\right).\end{aligned} \tag{4.19}$$

The second derivative in x can be written

$$\begin{aligned}\frac{\partial^2}{\partial x^2}P_l^m(x) &= -\frac{x}{(1-x^2)^{\frac{3}{2}}}\left(\frac{mx}{\sqrt{1-x^2}}P_l^m(x)+P_l^{m+1}(x)\right)-\frac{1}{\sqrt{1-x^2}}\left(\left(\frac{m}{\sqrt{1-x^2}}+\frac{mx^2}{(1-x^2)^{\frac{3}{2}}}\right)P_l^m(x)\right.\\ &\quad\left.+\frac{mx}{\sqrt{1-x^2}}P_l'^m(x)+P_l'^{m+1}(x)\right)\\ &= \frac{x}{1-x^2}P_l'^m(x)-\frac{1}{\sqrt{1-x^2}}\left(\frac{m(1-x^2)+mx^2}{(1-x^2)^{\frac{3}{2}}}P_l^m(x)+\frac{mx}{\sqrt{1-x^2}}P_l'^m(x)+P_l'^{m+1}(x)\right)\\ &= -\left(\frac{m}{(1-x^2)^2}P_l^m(x)+\frac{(m-1)x}{1-x^2}P_l'^m(x)+\frac{1}{\sqrt{1-x^2}}P_l'^{m+1}(x)\right)\\ &= \frac{m\big((m+1)x^2-1\big)}{(1-x^2)^2}P_l^m(x)+\frac{2mx}{(1-x^2)^{\frac{3}{2}}}P_l^{m+1}(x)+\frac{1}{1-x^2}P_l^{m+2}(x).\end{aligned} \tag{4.20}$$

The first derivative in ϑ' is then

$$\frac{\partial}{\partial\vartheta'}P_l^m(x) = \frac{mx}{\sqrt{1-x^2}}P_l^m(x)+P_l^{m+1}(x), \tag{4.21}$$

and the second derivative is

$$\begin{aligned}\frac{\partial^2}{\partial\vartheta'^2}P_l^m(x) &= -xP_l'^m(x)\\ &\quad+(1-x^2)\left(\frac{m\big((m+1)x^2-1\big)}{(1-x^2)^2}P_l^m(x)+\frac{2mx}{(1-x^2)^{\frac{3}{2}}}P_l^{m+1}(x)+\frac{1}{1-x^2}P_l^{m+2}(x)\right)\\ &= \frac{m\big((m+2)x^2-1\big)}{1-x^2}P_l^m(x)+\frac{(2m+1)x}{\sqrt{1-x^2}}P_l^{m+1}(x)+P_l^{m+2}(x).\end{aligned} \tag{4.22}$$

The derivative of $P_l^m(\cos\vartheta')$ with respect to ϑ is

$$\frac{\partial}{\partial\vartheta}P_l^m(\cos\vartheta') = \frac{\partial}{\partial\vartheta'}P_l^m(\cos\vartheta')\frac{\partial}{\partial\vartheta}\vartheta' = \frac{\pi}{\frac{\pi}{2}-\Lambda_0}\frac{\partial}{\partial\vartheta'}P_l^m(\cos\vartheta'), \tag{4.23}$$

and the second derivative is

$$\frac{\partial^2}{\partial\vartheta^2}P_l^m(\cos\vartheta') = \left(\frac{\pi}{\frac{\pi}{2}-\Lambda_0}\right)^2\frac{\partial^2}{\partial\vartheta'^2}P_l^m(\cos\vartheta'). \tag{4.24}$$

Finally, combining equation 4.23 and equation 4.21 and applying them to equation 4.4 gives the

first ϑ derivative:

$$\begin{aligned}
\frac{\partial}{\partial\vartheta}\Phi(x,\varphi) &= \frac{\pi}{\frac{\pi}{2}-\Lambda_0}\sum_{l=0}^{L}\left(A_{l0}\frac{\partial}{\partial\vartheta'}P_l^0(x)+\sum_{m=1}^{l}(A_{lm}\cos m\varphi+B_{lm}\sin m\varphi)\frac{\partial}{\partial\vartheta'}P_l^m(x)\right)\\
&= \frac{\pi}{\frac{\pi}{2}-\Lambda_0}\sum_{l=0}^{L}\left(A_{l0}P_l^1(x)\right.\\
&\quad\left.+\sum_{m=1}^{l}(A_{lm}\cos m\varphi+B_{lm}\sin m\varphi)\left(\frac{mx}{\sqrt{1-x^2}}P_l^m(x)+P_l^{m+1}(x)\right)\right)\\
&= \frac{\pi}{\frac{\pi}{2}-\Lambda_0}\sum_{l=0}^{L}\left(-A_{l0}\sqrt{1-x^2}\frac{d}{dx}P_l(x)\right.\\
&\quad+\sum_{m=1}^{l}(A_{lm}\cos m\varphi+B_{lm}\sin m\varphi)\left((-1)^m mx(1-x^2)^{\frac{m-1}{2}}\frac{d^m}{dx^m}P_l(x)\right.\\
&\quad\left.\left.+(-1)^{m+1}(1-x^2)^{\frac{m+1}{2}}\frac{d^{m+1}}{dx^{m+1}}P_l(x)\right)\right) \qquad (4.25)
\end{aligned}$$

Combining equation 4.24 and equation 4.22 and applying them to equation 4.4 gives the second ϑ derivative:

$$\begin{aligned}
\frac{\partial^2}{\partial\vartheta^2}\Phi(x,\varphi) &= \left(\frac{\pi}{\frac{\pi}{2}-\Lambda_0}\right)^2\sum_{l=0}^{L}\left(A_{l0}\frac{\partial^2}{\partial\vartheta'^2}P_l^0(x)\right.\\
&\quad\left.+\sum_{m=1}^{l}(A_{lm}\cos m\varphi+B_{lm}\sin m\varphi)\frac{\partial^2}{\partial\vartheta'^2}P_l^m(x)\right)\\
&= \left(\frac{\pi}{\frac{\pi}{2}-\Lambda_0}\right)^2\sum_{l=0}^{L}\left(A_{l0}\left(\frac{x}{\sqrt{1-x^2}}P_l^1(x)+P_l^2(x)\right)\right.\\
&\quad+\sum_{m=1}^{l}(A_{lm}\cos m\varphi+B_{lm}\sin m\varphi)\left(\frac{m(mx^2-1)}{1-x^2}P_l^m(x)\right.\\
&\quad\left.\left.+\frac{(2m+1)x}{\sqrt{1-x^2}}P_l^{m+1}(x)+P_l^{m+2}(x)\right)\right)\\
&= \left(\frac{\pi}{\frac{\pi}{2}-\Lambda_0}\right)^2\sum_{l=0}^{L}\left(A_{l0}\left(-x\frac{d}{dx}P_l(x)+(1-x^2)\frac{d^2}{dx^2}P_l(x)\right)\right.\\
&\quad+\sum_{m=1}^{l}(A_{lm}\cos m\varphi+B_{lm}\sin m\varphi)\left((-1)^m m(mx^2-1)(1-x^2)^{\frac{m}{2}-1}\frac{d^m}{dx^m}P_l(x)\right.\\
&\quad+(-1)^{m+1}(2m+1)x(1-x^2)^{\frac{m}{2}}\frac{d^{m+1}}{dx^{m+1}}P_l(x)\\
&\quad\left.\left.\left.+(-1)^m(1-x^2)^{\frac{m}{2}+1}\frac{d^{m+2}}{dx^{m+2}}P_l(x)\right)\right)\right). \qquad (4.26)
\end{aligned}$$

The derivatives in φ of equation 4.4 are:

$$\frac{\partial}{\partial\varphi}\Phi(x,\varphi) = \sum_{l=0}^{L}\sum_{m=1}^{l} m(-A_{lm}\sin m\varphi + B_{lm}\cos m\varphi)P_l^m(x)$$
$$= \sum_{l=0}^{L}\sum_{m=1}^{l} (-1)^m m(-A_{lm}\sin m\varphi + B_{lm}\cos m\varphi)(1-x^2)^{\frac{m}{2}}\frac{d^m}{dx^m}P_l(x), \quad (4.27)$$
$$\frac{\partial^2}{\partial\varphi^2}\Phi(x,\varphi) = -\sum_{l=0}^{L}\sum_{m=1}^{l} m^2(A_{lm}\cos m\varphi + B_{lm}\sin m\varphi)P_l^m(x)$$
$$= \sum_{l=0}^{L}\sum_{m=1}^{l} (-1)^{m+1} m^2(A_{lm}\cos m\varphi + B_{lm}\sin m\varphi)(1-x^2)^{\frac{m}{2}}\frac{d^m}{dx^m}P_l(x). \quad (4.28)$$

It is then possible to produce maps of $J_\parallel/\Sigma_P$, such as that shown in Figure 4.5.

Although $J_\parallel/\Sigma_P$ can be calculated analytically from the potential Φ, the method of fitting the potential chosen by *Ruohoniemi and Baker* [1998] means that the results of $J_\parallel/\Sigma_P$ calculations may not, in fact, be mathematically consistent. *De Santis* [1992], in introducing the method that would later be used in SuperDARN potential fitting, approximated $\sin\vartheta \approx \vartheta$ in order to convert Legendre's equation to a form in which ϑ may be scaled. He acknowledged that expanding the upper bound of ϑ to $\pi/2$ (compared to π in SuperDARN fitting) makes $\sin\vartheta \approx \vartheta$ no longer valid, but considered the results to be a fair approximation nevertheless. *Green et al.* [2006] discussed the method further and noted that reconstructed vectors calculated from the fitted potential are indeed valid. They did, however, point out that "stretching the data in this way distorts the basis functions so that they are no longer eigenfunctions of the Laplacian [p. 945]," meaning that analysis beyond reconstruction of the vector field must be done numerically or with complicated transformations to retain accuracy. In addition to the effects of the scaling, the Altitude-Adjusted Corrected Geomagnetic (AACGM) system of magnetic invariant coordinates used in the fitting of SuperDARN data (and from which the MLAT and MLT coordinates used in this thesis are obtained) is itself constructed in a non-orthogonal basis, built as it is upon realistic magnetic field line tracing between the northern and southern hemispheres [*Baker and Wing*, 1989].

Despite the reservations expressed by *Green et al.* [2006] and the non-orthogonal basis of the AACGM coordinates, this thesis proceeds with the approximations made by *De Santis* [1992] and consequently by *Ruohoniemi and Baker* [1998], although future improvements are suggested in Section 6.1. The following section compares $J_\parallel/\Sigma_P$ estimates calculated directly from the SuperDARN best-fit potential to estimates calculated numerically using Stokes' theorem, following, for

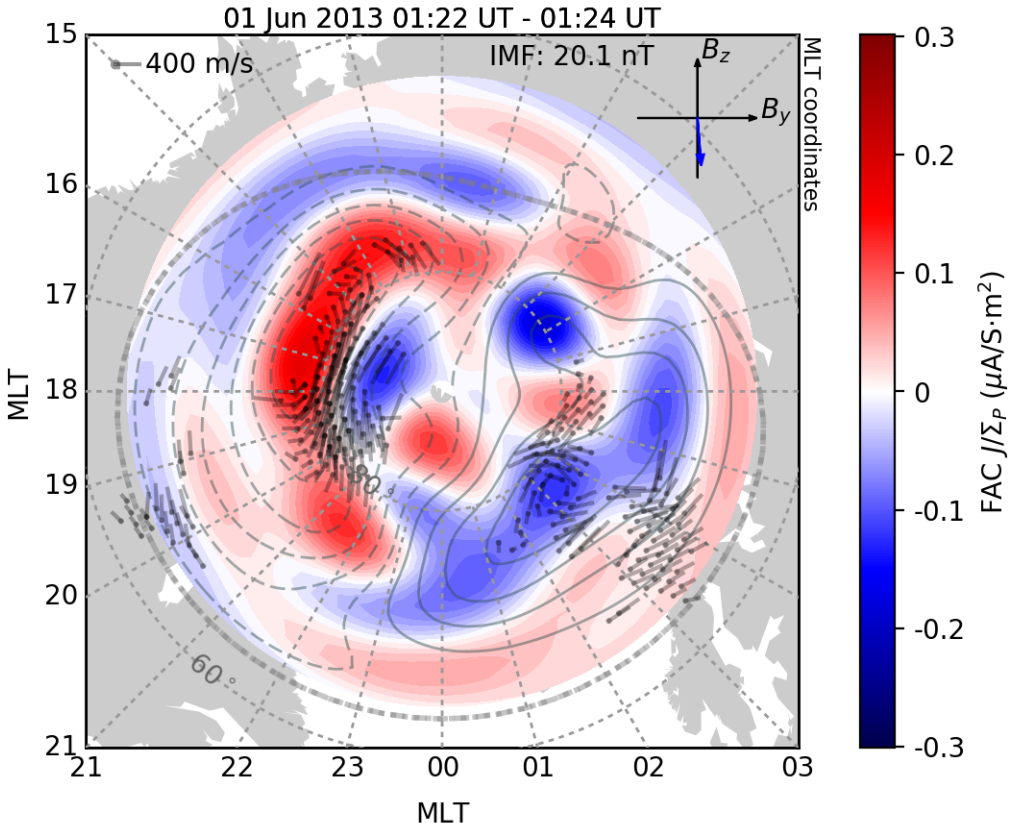

Figure 4.5: $J_{\parallel}/\Sigma_P$ in the 01:22 UT to 01:24 UT interval on 1 June 2013, calculated analytically from the SuperDARN potential function, in MLAT–MLT coordinates. $J_{\parallel}/\Sigma_P$ is shown as a heat map, with red representing upward (positive) FAC and blue representing downward (negative) FAC and the colour intensity scaling with the intensity of $J_{\parallel}/\Sigma_P$ as shown by the colour bar at the right of the figure. True vectors (of plasma velocity) are overlaid as grey barbs pointing in the direction of flow. Barb length is proportional to speed, and a scale sample barb of length 400 m/s is plotted at the upper left corner of the figure. MLT lines and MLAT curves (at 60° MLAT and 80° MLAT) are marked with short-dashed lines. The positive and negative potential contours and the HMB are plotted as solid, long-dashed, and heavy dotted curves, respectively, and the IMF projection on the GSM y–z plane is plotted in the upper right corner with the projected magnitude annotated along the top of the figure.

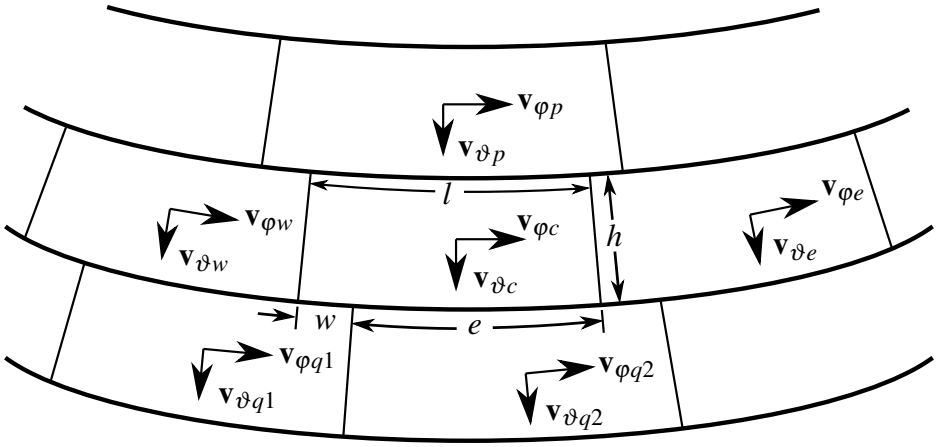

Figure 4.6: Velocity components and dimensions of typical adjacent *Ruohoniemi and Baker* [1998] grid cells. The central cell has components denoted c, the west cell w, the east cell e, the poleward cell p, and the equatorward cell q. Cell height h is constant for all cells. Poleward edge cell length l is less than equatorward cell length $w+e$.

example, *Sofko et al.* [1995] and *McWilliams* [1997]. Stokes' theorem is independent of the coordinate system used, requiring only a surface with a closed boundary, so the non-orthogonal basis resulting from the *De Santis* [1992] approximations and the use of AACGM coordinates does not pose a problem. The results of the potential calculation method are consistent with the results of the established Stokes' theorem method, meaning the new method may be employed without significant loss of accuracy when compared to the existing method.

4.3 Calculating Plasma Flow Vorticity Using Stokes' Theorem

The curl of velocity can be calculated from discrete velocity data using Stokes' theorem, an established approach introduced by *Sofko et al.* [1995]. Using equation 4.13, if S is an n-sided polygon and $\mathbf{v}$ is constant along each of the sides of S, then the integrals of Stokes' theorem can be converted to multiplications and additions:

$$A\nabla \times \mathbf{v} = \sum_{i=1}^{n} v_i l_i, \tag{4.29}$$

where A is the area of S, l_i is the length of the ith side of S, and v_i is the parallel component of $\mathbf{v}$ along the ith side.

It was convenient in the case of this thesis to use the grid cells defined by *Ruohoniemi and Baker* [1998] as the S surfaces, as shown in Figure 4.6. The fitting process already considers the θ

and φ components of the velocity in a grid cell to be constant over the area of the approximately trapezoidal cell.

The velocity component parallel to the eastern or western boundary of a grid cell was calculated from the average of the ϑ velocity components of that cell and its neighbour to the east or west. For example, the central cell in Figure 4.6 has a western boundary parallel velocity magnitude v_w of

$$v_w = \frac{v_{\vartheta w} + v_{\vartheta c}}{2}, \tag{4.30}$$

which is multiplied by the north–south cell height h for use in the sum of equation 4.29.

Calculating the velocity component parallel to the northern or southern boundary of a cell required the irregular arrangement of the cells to be considered, so the φ velocity components of the adjacent cells were combined in an average weighted by the lengths of the shared boundaries between the cells. For example, the central cell in Figure 4.6 has only one neighbouring cell on the poleward side and the cells have a shared boundary of length l, so the parallel velocity magnitude v_p times length l_p that enters into the sum of equation 4.29 is

$$v_p l_p = \frac{v_{\varphi p} + v_{\varphi c}}{2} l. \tag{4.31}$$

The central cell borders two cells on the equatorward side, however, so the parallel velocity magnitude v_q times length l_q is

$$v_q l_q = \frac{v_{\varphi q1} w + v_{\varphi q2} e + v_{\varphi c} (w + e)}{2}. \tag{4.32}$$

The ϑ components of velocity were all oriented as positive in the $\hat{\vartheta}$ direction, and the φ components were all oriented as positive in the $\hat{\varphi}$ direction. To obtain a curl from equation 4.29 that was positive counterclockwise, the sum was computed thus:

$$\sum_{i=1}^{n} v_i l_i = v_w l_w + v_q l_q - v_e l_e - v_p l_p. \tag{4.33}$$

Lengths used in these calculations were measured on the surface of the sphere, and were not chords.

The area A of each grid cell on the surface of the sphere was calculated exactly: it can be shown that

$$A = r^2 \Delta\varphi \left(\sin\Lambda_p - \sin\Lambda_q \right), \tag{4.34}$$

where r is the radius of the sphere, $\Delta\varphi$ is the angular (longitudinal) width of the grid cell, and Λ_p and Λ_q are the poleward and equatorward bounding magnetic latitudes of the grid cell, respectively.

Two special cases occurred when using Stokes' theorem to calculate plasma flow vorticity on the *Ruohoniemi and Baker* [1998] grid. First, the plasma velocity at the equatorward edge of the grid is set to zero in the fitting process, so for consistency the last row of grid cells had each cell's equatorward boundary velocity set to zero. Second, the most poleward of the grid cells are triangular, tapering to a point at the pole, and have no poleward boundary contribution. Applying the same calculation method to the grid cells at the pole was found to produce unreliable results, so Stokes' theorem was applied to the full spherical cap consisting of the polar grid cells. The equatorward boundary length and parallel velocity were found for each of the polar cells, and the sum of the contributions of all polar cells was divided by the area A of the full spherical cap, given by

$$A = 2\pi r^2 \left(1 - \sin\Lambda_q\right). \tag{4.35}$$

The resulting value of $J_\parallel/\Sigma_P$ was assumed to be uniform over the spherical cap and assigned to each of the polar cells.

Plasma flow vorticity estimates calculated using Stokes' theorem are included in this thesis for comparison and validation of FAC estimates calculated directly from the best-fit potential using equation 4.16. Stokes' theorem was used to calculate $J_\parallel/\Sigma_P$ from the fitted velocity components in every cell of the northern hemisphere convection map to compare with $J_\parallel/\Sigma_P$ calculated using equation 4.16 as a test of consistency. Stokes' theorem applied to fitted velocities and equation 4.16 should produce similar results because both are computed from the same fitted potential function. Stokes' theorem was also applied to calculate $J_\parallel/\Sigma_P$ estimates using raw gridded SuperDARN velocity vectors resolved into ϑ and φ components to compare with $J_\parallel/\Sigma_P$ calculated using both of the methods that were based on the fitted potential. In this way it was possible to examine whether the potential fitting method returned reasonable results for $J_\parallel/\Sigma_P$ in light of the input velocity data, whichever way $J_\parallel/\Sigma_P$ was calculated from the potential. To use the raw gridded velocity data it was necessary to set velocity to zero in grid cells that did not contain measured SuperDARN data. (That is, no model or fitting contributions were included.)

A complication in the implementation of Stokes' theorem using gridded velocity data was the occasional occurrence of multiple gridded velocity vectors in some of the grid cells. As described

above, RST combines all of the data from each radar into a single velocity in each grid cell, but does not combine data from different radars. Multiple velocity vectors, one from each radar, may be contained in a grid cell. The fitting process is such that this should not have a large effect in practice: at each cell with gridded data, the comparison of the fitted velocity with the gridded velocity is added to the χ^2 sum in accordance with equation 4.11. How many times a grid cell contributes data is not important to the algorithm. The result is a sort of implicit averaging of velocity within a cell when multiple vectors are present. It is not straightforward singular value decomposition, but it is still usable. For plotting of raw or true velocity the occurrence of multiple data in a cell is likewise not a problem, as all vectors can be plotted. However, calculation of a single value for a specific cell, such as curl, must take account of all available data at once. Therefore, the full set of gridded velocity data were processed before performing a Stokes' theorem calculation to ensure there was only one gridded velocity vector in each grid cell. The simple method chosen to reduce multiple data within a cell was to average all ϑ components and all φ components separately and calculate a single resultant.

Figure 4.7 shows $J_{\parallel}/\Sigma_P$ estimated by applying Stokes' theorem to the *Ruohoniemi and Baker* [1998] grid cells. When compared to Figure 4.5, the $J_{\parallel}/\Sigma_P$ features appear to match well in size, shape, sense, and intensity (the same colour scale is used for both plots). The comparison of the two methods is made more clear when the absolute difference between the $J_{\parallel}/\Sigma_P$ estimates calculated using Stokes' theorem and the estimates calculated from the potential using equation 4.16 are plotted in Figure 4.8 using a colour scale that extends 10% as far as that of Figures 4.5 and 4.7. To produce this plot, $J_{\parallel}/\Sigma_P$ was calculated from the potential at the centre of each grid cell and subtracted from the Stokes' theorem result for $J_{\parallel}/\Sigma_P$ in that cell. The largest differences occur at the equatorward and poleward edges of the grid, which can be explained respectively as the effects of setting zero plasma velocity at the equatorward boundary and of the mathematical pole that equation 4.16 has at the coordinate poles. Everywhere else on the map the difference is small, even with this 10% colour scale. An examination of the data reveals that the largest relative differences occur where the value of $J_{\parallel}/\Sigma_P$ is small. The level of agreement seen in these examples is typical of comparisons between potential-calculated $J_{\parallel}/\Sigma_P$ estimates and Stokes' theorem $J_{\parallel}/\Sigma_P$ estimates using fitted velocities.

Figure 4.9 shows estimated $J_{\parallel}/\Sigma_P$ calculated by applying Stokes' theorem to the raw gridded

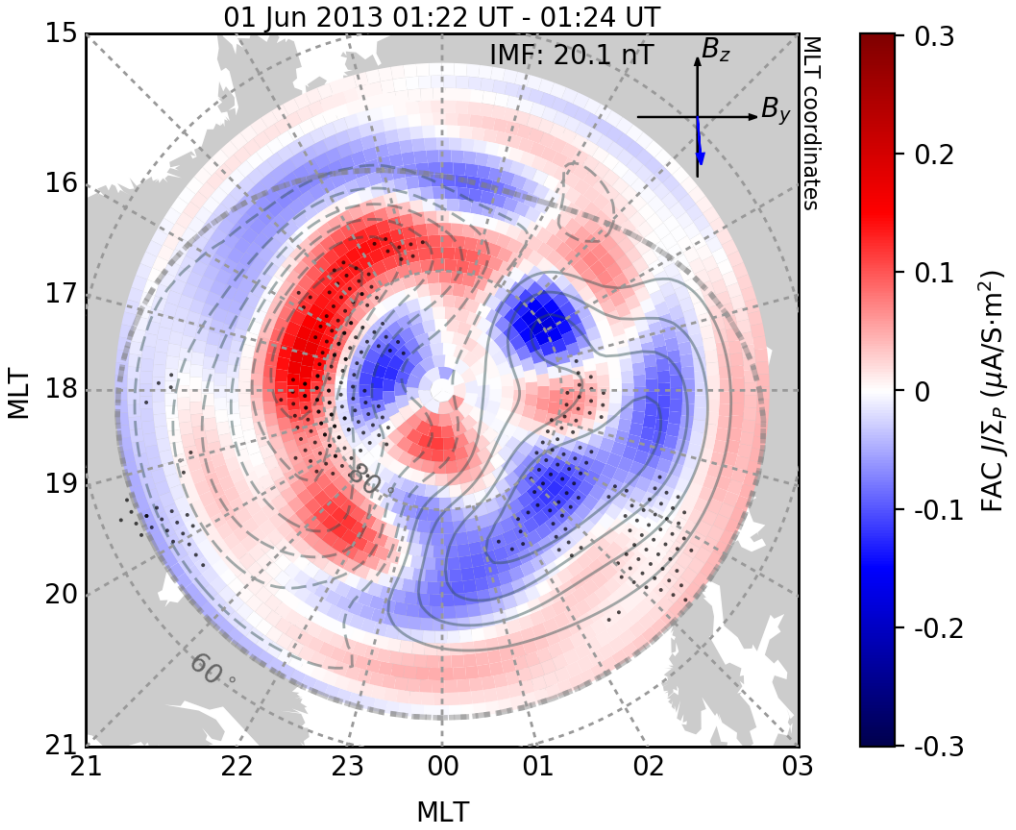

Figure 4.7: $J_{\parallel}/\Sigma_P$ in the 01:22 UT to 01:24 UT interval on 1 June 2013, calculated by applying Stokes' theorem to the fitted velocities in the grid cells of *Ruohoniemi and Baker* [1998], in MLAT–MLT coordinates. $J_{\parallel}/\Sigma_P$ is shown as a heat map, with red representing upward (positive) FAC and blue representing downward (negative) FAC and the colour intensity scaling with the intensity of $J_{\parallel}/\Sigma_P$ as shown by the colour bar at the right of the figure. MLT lines and MLAT curves (at 60° MLAT and 80° MLAT) are marked with short-dashed lines. The positive and negative potential contours and the HMB are plotted as solid, long-dashed, and heavy dotted curves, respectively, and the IMF projection on the GSM y–z plane is plotted in the upper right corner with the projected magnitude annotated along the top of the figure.

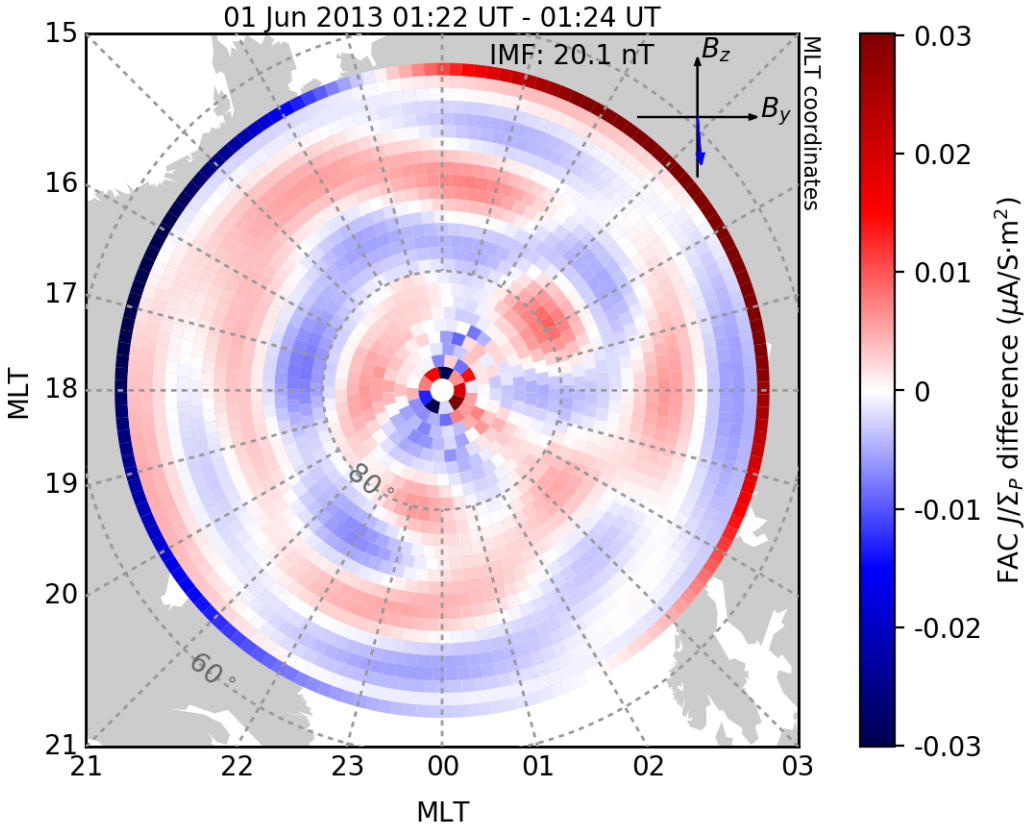

Figure 4.8: The absolute difference between the Stokes' theorem estimates of $J_\parallel/\Sigma_P$ (Figure 4.7) and the potential-calculated estimates of $J_\parallel/\Sigma_P$ (Figure 4.5) in the 01:22 UT to 01:24 UT interval of 1 June 2013, in MLT–MLAT coordinates. The difference is plotted as a heat map showing the Stokes' theorem value minus the potential-calculated value, according to the colour bar at the right of the figure. The colour scale has 10% of the extent of the scale used in previous maps of $J_\parallel/\Sigma_P$ estimates. Circles of MLAT and lines of MLT are shown as short-dashed lines, and the IMF projection on the GSM y–z plane is plotted in the upper right corner with the projected magnitude annotated along the top of the figure.

SuperDARN velocity data. There are two main clusters of visible FAC present, which necessarily correspond to the cells containing measured, gridded data (marked with black dots). In the afternoon cluster, a central region of upward FAC (red) centred at 17:30 MLT and 80° MLAT corresponds to the larger, similarly located region of upward FAC seen in the preceding Figures 4.5 and 4.7. A region of downward FAC (blue) closer to the pole also has a counterpart in the figures based on the potential. In the poleward portion of the morning data cluster centred at 03:30 MLT and 70° MLAT, a region of downward FAC paired with a region of upward FAC corresponds to the edge of the postmidnight downward FAC region in the preceding figures. A small data cluster is also seen at 20:00 MLT and 65° MLAT. In this cluster, upward FAC is on the poleward side and tilted slightly toward midnight, and downward FAC is on the equatorward side and tilted slightly toward sunset. A similar arrangement is seen at this location in the preceding plots (Figures 4.5 and 4.7).

In all of the cases of inconsistency of $J_{\parallel}/\Sigma_P$ estimates determined from the measured, gridded data and the potential-calculated data, the most noticeable discrepancies are seen when the edges of the FAC regions in Figure 4.9 are compared to the corresponding locations in Figures 4.5 and 4.7. In the calculation using raw gridded data, all of the grid cells except those containing original measured data (which are marked with black dots) have plasma velocity components set to zero, resulting in sharp, stepwise transitions at the edges of measured data regions. The sudden changes can lead to overestimation of $J_{\parallel}/\Sigma_P$. For example, if a grid cell has parallel plasma velocity components in the same direction at opposing cell boundaries, the counterclockwise integration around the grid cell used for the Stokes' theorem calculation causes a partial cancellation between the velocities. Should one of the parallel velocity components be set to zero, as was done in the case of Figure 4.9, the cancellation disappears and the calculated $J_{\parallel}/\Sigma_P$ artificially becomes either larger or smaller, depending on the contributions of the other sides. Overall, the level of agreement seen between this $J_{\parallel}/\Sigma_P$ estimate calculated from raw gridded data using Stokes' theorem and the $J_{\parallel}/\Sigma_P$ estimate in Figure 4.5 calculated directly from the fitted potential is typical of such comparisons.

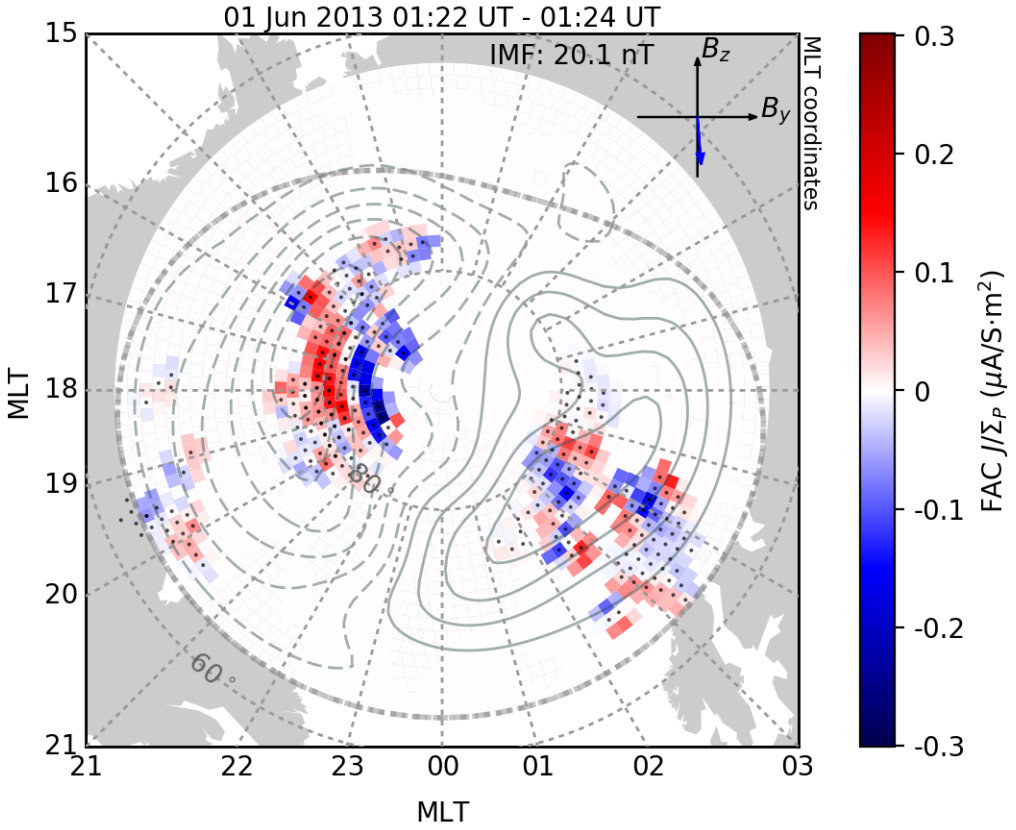

Figure 4.9: $J_{\parallel}/\Sigma_P$ in the 01:22 UT to 01:24 UT interval on 1 June 2013, calculated by applying Stokes' theorem to only the measured, gridded SuperDARN velocity data, in MLAT–MLT coordinates. $J_{\parallel}/\Sigma_P$ is shown as a heat map, with red representing upward (positive) FAC and blue representing downward (negative) FAC and the colour intensity scaling with the intensity of $J_{\parallel}/\Sigma_P$ as shown by the colour bar at the right of the figure. Grid cells containing measured data are marked with black dots. MLT lines and MLAT curves (at 60° MLAT and 80° MLAT) are marked with short-dashed lines. The positive and negative potential contours and the HMB are plotted as solid, long-dashed, and heavy dotted curves, respectively, and the IMF projection on the GSM y–z plane is plotted in the upper right corner with the projected magnitude annotated along the top of the figure.

4.4 Comparison with the Multi-Satellite AMPERE Project

In order to show that the method presented in this thesis may be consistent with externally-derived estimates of FAC, a comparison with published FAC data from AMPERE (Active Magnetosphere and Planetary Electrodynamics Response Experiment) is presented here. The AMPERE project [*Anderson et al.*, 2000] uses data from the engineering magnetometers on board the satellites of the commercial Iridium constellation to estimate FACs. AMPERE produces FAC information from *in-situ* measurements of the magnetic field in low Earth orbit, estimating $J_{\parallel}$ from Ampère's law $\nabla \times \mathbf{B} = \mu_0 \mathbf{J}$, compared to $J_{\parallel}/\Sigma_P$ estimated by SuperDARN.

Still, AMPERE has its own limitations. The Iridium satellites (there are over 70) are deployed in polar orbits in six planes spaced approximately two hours apart (at AMPERE's altitude of 780 km [*Anderson et al.*, 2000], that is approximately 1900 km at 60° latitude), and orbit once in approximately 104 minutes. The satellites have an average latitudinal spacing of approximately 33°. Each satellite transmits magnetometer data to the ground with a typical sampling rate of one every 200 seconds, placing a practical lower bound on the time resolution of the method [*Anderson et al.*, 2000]. Although AMPERE does not rely on modelled ionospheric conductivity, to estimate FAC from satellite data it is necessary to assume infinite sheets of current [*Iijima and Potemra*, 1976b], making the AMPERE method an approximation, just as the SuperDARN method is.

SuperDARN FAC maps can be produced every one to two minutes depending on the radar scan mode used, and the method provides latitudinal and longitudinal spacing of approximately 111 km (which is approximately 10 minutes of MLT at 60° latitude). When favourable radar scattering conditions are widespread, SuperDARN provides excellent coverage compared to AMPERE in both space and time.

Maps of $J_{\parallel}/\Sigma_P$ were generated from SuperDARN data following the method of this thesis and compared with published maps of FAC [*Anderson et al.*, 2000, 2008] estimated by AMPERE from measured magnetic field perturbation data. Good agreement was found in many of the comparisons. One of the better comparisons is shown in Figure 4.10 to demonstrate that it is possible to find reasonably good agreement between the two methods despite their respective limitations.

On the left of Figure 4.10 is a plot of AMPERE estimated FAC density in the 15 UT to 16 UT interval of 23 March 2002, from *Anderson et al.* [2008]. Region 2 downward FAC (blue) is present

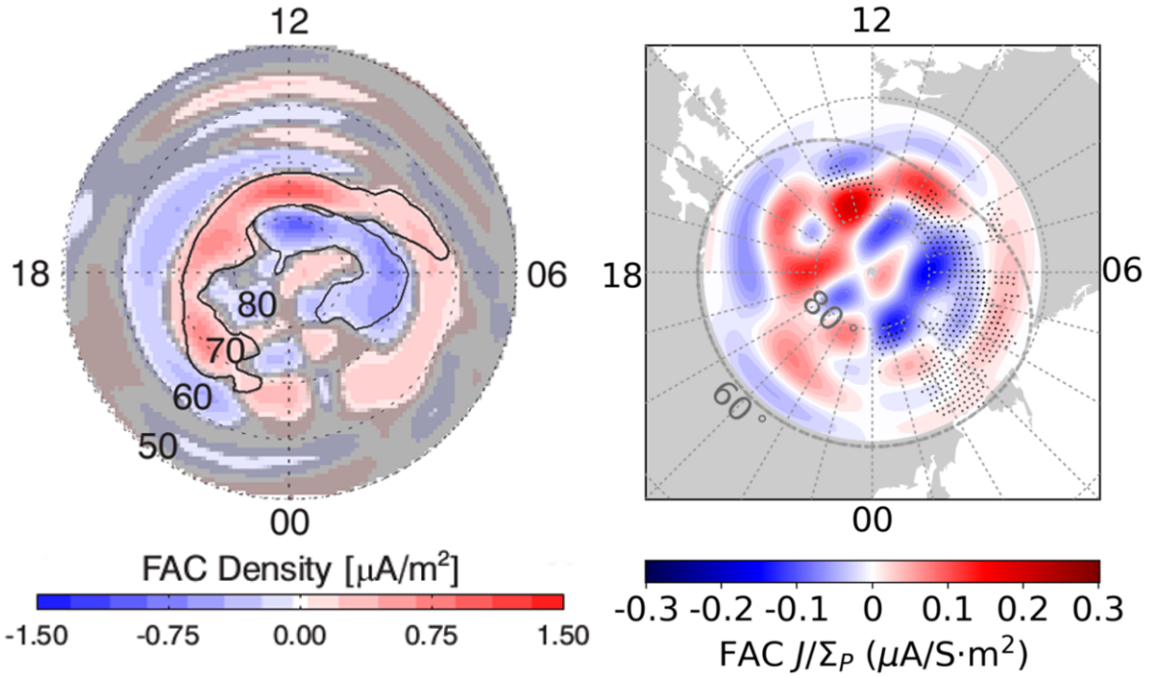

Figure 4.10: One-hour maps of FAC estimates from AMPERE and SuperDARN, 15 UT to 16 UT on 23 March 2002. On the left is Figure 1c from *Anderson et al.* [2008], showing AMPERE estimated FAC. On the right is SuperDARN estimated $J_{\parallel}/\Sigma_P$. In both cases FAC is shown as a colour map, with red indicating upward FAC and blue indicating downward FAC. The SuperDARN map also includes the HMB (a dashed grey line) and measured data locations (black dots). Both maps are plotted in MLT and invariant latitude coordinates. The IMF at this time was directed dawnward.

poleward of 60° MLAT between 11 MLT and 23 MLT. The region 2 FAC is paired with region 1 upward FAC (red) that extends from 10 MLT to magnetic midnight around the duskside and from 70° MLAT to 80° MLAT. The region 1 upward FAC blends into the region 2 upward FAC on the dawnside, extending from the noon sector around to 02 MLT and reaching as far equatorward as 60° MLAT. The region 1 down FAC is poleward of 70° MLAT from 04 MLT to 13 MLT, reaching 80° MLAT on the dawnside and nearly to the pole at magnetic noon. Strong FAC regions include upward FAC centred at noon and 75° MLAT and downward FAC centred slightly prenoon and at 82° MLAT.

On the right of Figure 4.10 is a map of SuperDARN estimated $J_{\parallel}/\Sigma_P$ for the same interval on 23 March 2002. Region 2 downward FAC (blue) extends from 09 MLT to magnetic midnight around the duskside, poleward of 60° MLAT. Region 1 upward FAC (red) begins at approximately 70° MLAT and reaches as far poleward as 85° MLAT, extending from 09 MLT to 23 MLT around the duskside. Weak region 2 upward FAC is present between 60° MLAT and 70° MLAT from magnetic midnight to 08 MLT. Region 1 downward FAC is present poleward of 70° MLAT, extending to approximately 85° MLAT on the dawnside and nearly to the pole at magnetic noon, and reaches from magnetic midnight to 13 MLT. The SuperDARN map ends at approximately 60° MLAT because of the boundary placed on the potential function fit by the location of the HMB, which is shown as a dashed grey line.

While the upward and downward FAC regions do not match perfectly between the AMPERE map and SuperDARN map of Figure 4.10, there is clearly strong agreement, even without the inclusion of conductivity in the SuperDARN estimates. The regions of strong FAC in the AMPERE estimates correspond reasonably well with some of the stronger $J_{\parallel}/\Sigma_P$ regions in the SuperDARN estimates, namely the upward FAC centred at 13 MLT and 75° MLAT and the downward FAC centred at 82° MLAT and 10:30 MLT. The SuperDARN estimates show stronger $J_{\parallel}/\Sigma_P$ on the nightside than the AMPERE estimates of FAC show, which is consistent with lower photo-induced conductance on the nightside.

It is important to note that because of the integration over times on the scale of hours performed to produce AMPERE maps, hours of SuperDARN data must likewise be integrated for comparison with AMPERE results. A certain amount of agreement between the two methods is therefore expected due to the statistical model used in the SuperDARN potential fitting algorithm. Maps

of $J_{\parallel}/\Sigma_P$ that include regions without SuperDARN coverage may appear to match AMPERE FAC maps well when, in truth, the model contribution is the cause of the match. Therefore, caution is necessary when making comparisons between the two instruments to ensure that measured data from the interval at hand is represented to a meaningful level in the SuperDARN maps.

4.5 Computer Implementation

The computer programs used for calculations and plotting in this thesis are written in Python to be used in conjunction with the DaViT-py SuperDARN data processing and plotting software package (URL: https://github.com/vtsuperdarn/davitpy). The FAC code will be integrated into DaViT-py. DaViT-py includes tools for handling other associated space physics data as well. The FAC code makes use of built-in DaViT-py functionality for using SuperDARN data files as input and for plotting. The Python NumPy package (URL: http://www.numpy.org) is used for calculations according to the equations presented in this chapter. Most notably, the Legendre Module of the Polynomial Package in NumPy is used for fast vector and array operations involving Legendre polynomials. (The equations for plasma velocity $\mathbf{v}$ and $J_{\parallel}/\Sigma_P$ were expressed in terms of Legendre polynomials P_l and not associated Legendre functions P_l^m because the Legendre Module does not include associated Legendre function capability.) Matplotlib [*Hunter*, 2007] (URL: https://matplotlib.org) is used in the FAC code and by DaViT-py for plotting. Line drawings were made with Inkscape (URL: https://inkscape.org) and this thesis was set in LaTeX.

CHAPTER 5

CASE STUDY

To demonstrate the applicability of the potential-function FAC estimation technique, a case study is presented here of the geomagnetic storm that occurred from 31 May to 1 June 2013. Maps of $J_{\parallel}/\Sigma_P$ from SuperDARN data in the northern hemisphere are examined, and the estimates are compared to measured plasma flow patterns, theoretical conceptions of FAC structure, and FAC measurements by other instruments. The strengths and weaknesses of the estimation method are discussed in light of the comparisons.

5.1 The 31 May 2013 Geomagnetic Storm

In the late evening (UT) of 31 May 2013, the IMF B_z component began to climb from near zero, reaching an unusually large value of nearly +18 nT (northward) in the early morning of 1 June before reversing to less than -20 nT (southward) within four minutes. The IMF components, shown in Figure 5.1, are measured in the geocentric solar magnetospheric (GSM) coordinate system. GSM coordinates are centred on the Earth, with positive x toward the Sun, y perpendicular to the plane containing x and the Earth's magnetic dipole axis and positive in the duskward direction, and z completing the right-handed system and positive in the northward direction. For a more detailed definition of the GSM system, see Appendix A.

Within an hour of the IMF's southward turning, the SYM-H geomagnetic activity index began to fall as shown in Figure 5.2, indicating that a geomagnetic storm was underway. SYM-H is a ground-based, longitudinally-symmetric index of geomagnetic disturbances in the horizontal, meridional direction, derived from measurements taken at six geomagnetic observatories selected

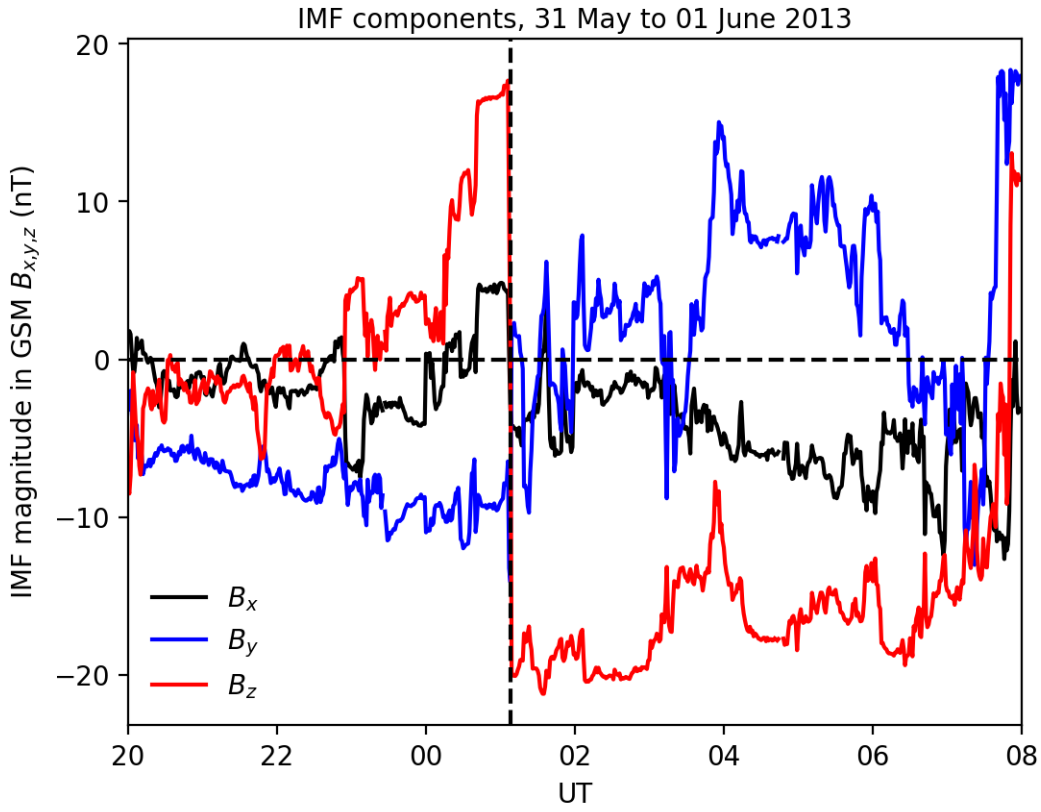

Figure 5.1: IMF components in GSM coordinates from 20 UT on 31 May to 08 UT on 1 June, 2013. The vertical dashed line marks the time of the IMF southward turning.

from a set of 13 such stations [*Nosé et al.*, 2012].

The following discussion includes a selection of FAC maps from the storm period showing $J_{\parallel}/\Sigma_P$ estimated from SuperDARN data and overlaid with SuperDARN true vectors. The aim is to demonstrate the utility of the $J_{\parallel}/\Sigma_P$ calculation method, as well as its consistency when compared with measured velocity data and with expected FAC and plasma convection patterns.

The IMF components in Figure 5.1 were measured by the Advanced Composition Explorer (ACE) spacecraft, and were time-shifted to Earth's bow shock nose according to the solar wind speed measured at the spacecraft and a model of the bow shock [*King and Papitashvili*, n.d.]. When used in SuperDARN analysis, IMF data are time-shifted by an additional 10 minutes to propagate the solar wind conditions from the bow shock nose to the magnetopause, where the earliest interaction between the IMF and the geomagnetic field occurs. A diagram of the IMF magnitude and orientation at the magnetopause is inset in the corner of each $J_{\parallel}/\Sigma_P$ map.

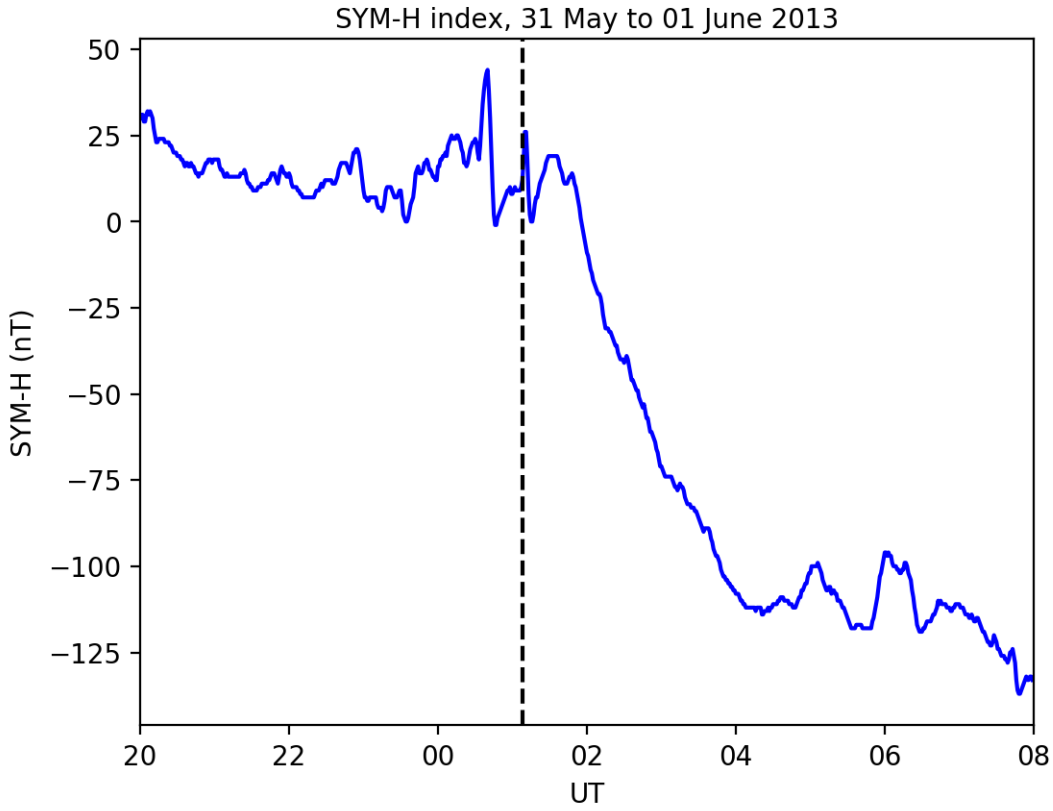

Figure 5.2: The SYM-H index from 20 UT on 31 May to 08 UT on 1 June, 2013. The vertical dashed line marks the time of the IMF southward turning.

5.2 A Two-Cell Convection Pattern

A map of $J_{\parallel}/\Sigma_P$ estimated from SuperDARN data using the potential method described in Chapter 4 is shown in Figure 5.3. The map was generated for the period from 21:34 UT to 21:36 UT on 31 May 2013. Southward IMF conditions prevailed, and a two-cell convection pattern can be seen in the figure. The estimated $J_{\parallel}/\Sigma_P$ can be compared with the expected FAC configuration to assess the performance of the estimation technique.

The IMF projection on the GSM coordinates y-z plane is inset in the top right corner of the plot, showing that the IMF reaching the dayside magnetopause at 21:34 UT had a strong negative B_y (dawnward) component and was weakly southward. Note that because the inset IMF coordinates are in a positive right, positive up orientation, the inset y component is directed oppositely to the y component in the $J_{\parallel}/\Sigma_P$ map. The GSM y coordinates in the map is positive duskward (left), the x component is positive sunward (up), and the z component is positive northward (out of the page). There is a velocity scale vector in the upper left corner of the figure.

The dawnward component of the IMF causes the cross-polar flow to deviate from the Earth–Sun (noon–midnight) line in the duskward direction as it enters the polar cap on the dayside. Ionospheric plasma flows across the pole to the nightside convection reversal, where the plasma leaves the polar cap and returns to the dayside at lower latitudes. The dawnside flow forms a round cell pattern, while the duskside flow forms a crescent cell pattern, which in this case is split into a small region of circulation on the dayside near noon and a larger region of circulation reaching across the polar cap to the nightside convection reversal.

The distribution of $J_{\parallel}/\Sigma_P$ in Figure 5.3 can be seen to correspond to locations of strong plasma vorticity. At the centre of the dawn round cell, where there is large upward $\nabla \times \mathbf{v}$, there is a region of strong downward FAC (shown in blue). The downward FAC is maintained through the majority of the round cell, consistent with its counterclockwise circulation. Similarly, in the centres of the two regions of large downward curl in the dusk crescent cell there is strong upward FAC (shown in red), as well as throughout the remainder of the clockwise circulation of the crescent cell. Regions of velocity shear also produce curl, which is demonstrated in places such as the equatorward fringes of the circulation pattern where flow speed weakens, and in the patches of upward FAC in the round cell and between the round and crescent cells near the pole.

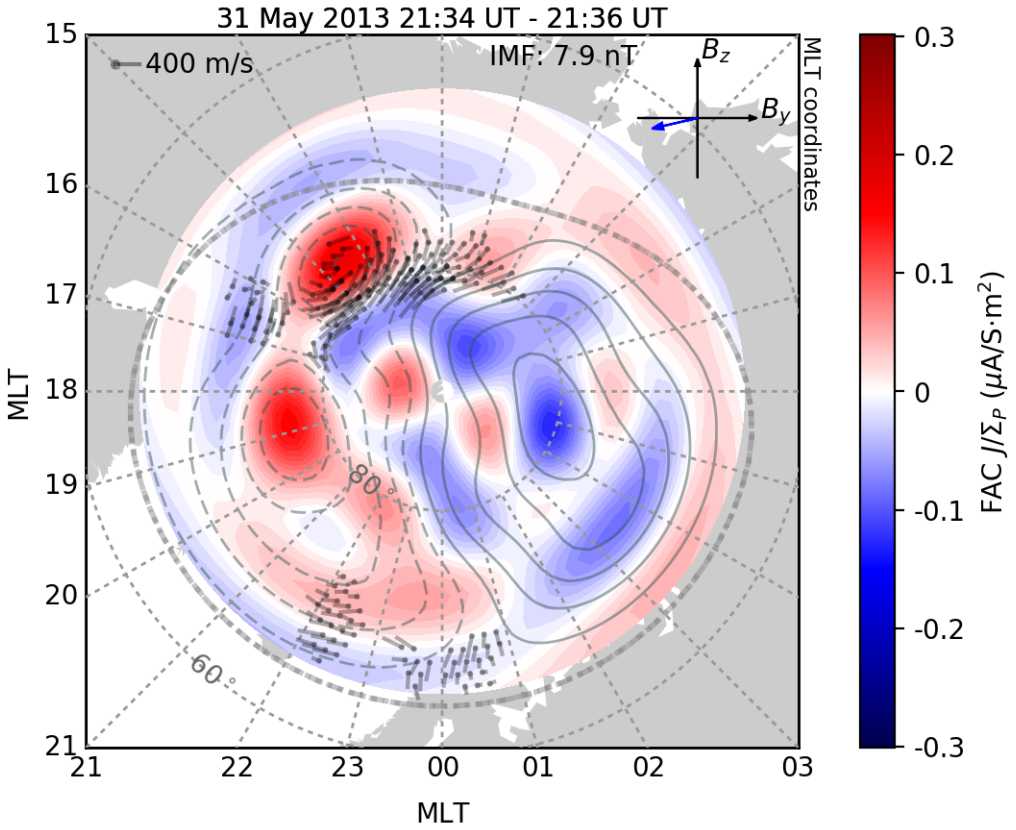

Figure 5.3: SuperDARN $J_{\parallel}/\Sigma_P$ estimates in the 21:34 UT to 21:36 UT interval on 31 May 2013, in MLAT–MLT coordinates. $J_{\parallel}/\Sigma_P$ is shown as a heat map, with red representing upward (positive) FAC and blue representing downward (negative) FAC and the colour intensity scaling with the intensity of $J_{\parallel}/\Sigma_P$ as shown by the colour bar at the right of the figure. True vectors (of plasma velocity) are overlaid as grey barbs pointing in the direction of flow. Barb length is proportional to speed, and a scale sample barb of length 400 m/s is plotted at the upper left corner of the figure. MLT lines and MLAT curves (at 60° MLAT and 80° MLAT) are marked with short-dashed lines. The positive and negative potential contours and the HMB are plotted as solid, long-dashed, and heavy dotted curves, respectively, and the IMF projection on the GSM y–z plane is plotted in the upper right corner with the projected magnitude annotated along the top of the figure.

The $J_\parallel/\Sigma_P$ in Figure 5.3 demonstrates region 1 upward FAC (red) in the duskside cell and downward FAC (blue) in the dawnside cell, and oppositely directed region 2 FAC at the equatorward edges of the cells, upward (red) on the dawnside and downward (blue) on the duskside. The FAC estimates from SuperDARN are consistent with the expected configuration of the FAC regions shown in Figure 2.10, *Cowley*'s [2000] depiction of the region 1 and region 2 FACs, streamlines, and electric field for a directly southward IMF.

5.2.1 Comparison with Modelled Conductance

No attempt is made in this thesis to account for ionospheric conductance—whether from measurements or a model—into the calculation of FAC; that, along with the calculation of the remaining three terms of the FAC equation (2.26), is left for future work. Nevertheless, to aid in the interpretation of maps of $J_\parallel/\Sigma_P$, it is useful to have a qualitative understanding of typical Σ_P structure. To that end, the work of *Hardy et al.* [1987] is introduced. *Hardy et al.* [1987] used the empirical models of *Robinson and Vondrak* [1984] to calculate expected Pedersen and Hall conductance produced by solar photoionisation, and also empirically determined conductance produced by particle precipitation.

By fitting curves to vertical conductivity profiles that were calculated from Chatanika incoherent scatter radar electron density data, *Robinson and Vondrak* [1984] found a representation for photo-induced Σ_P and Σ_H:

$$\Sigma_P = 0.88\sqrt{S_a \cos\chi} \tag{5.1}$$

$$\Sigma_H = 1.5\sqrt{S_a \cos\chi}, \tag{5.2}$$

where S_a is the daily 10.7 cm solar radio flux in units of 10^{-22} W/m^2·Hz, measured at Ottawa and adjusted to 1 astronomical unit (AU), and χ is the solar zenith angle. The 10.7 cm flux obtained from Natural Resources Canada via the NASA OMNIWeb (URL: https://omniweb.gsfc.nasa.gov) was 104.7×10^{-22} W/m^2·Hz on 31 May 2013 and 108.8×10^{-22} W/m^2·Hz on 1 June 2013. The Pedersen conductance due to photoionisation at the time of Figure 5.3 is plotted in Figure 5.4, along with the day–night terminator.

Hardy et al. [1987] created statistical models of the Pedersen and Hall conductance induced by particle precipitation by fitting Epstein functions to conductance calculated from Defense Met-

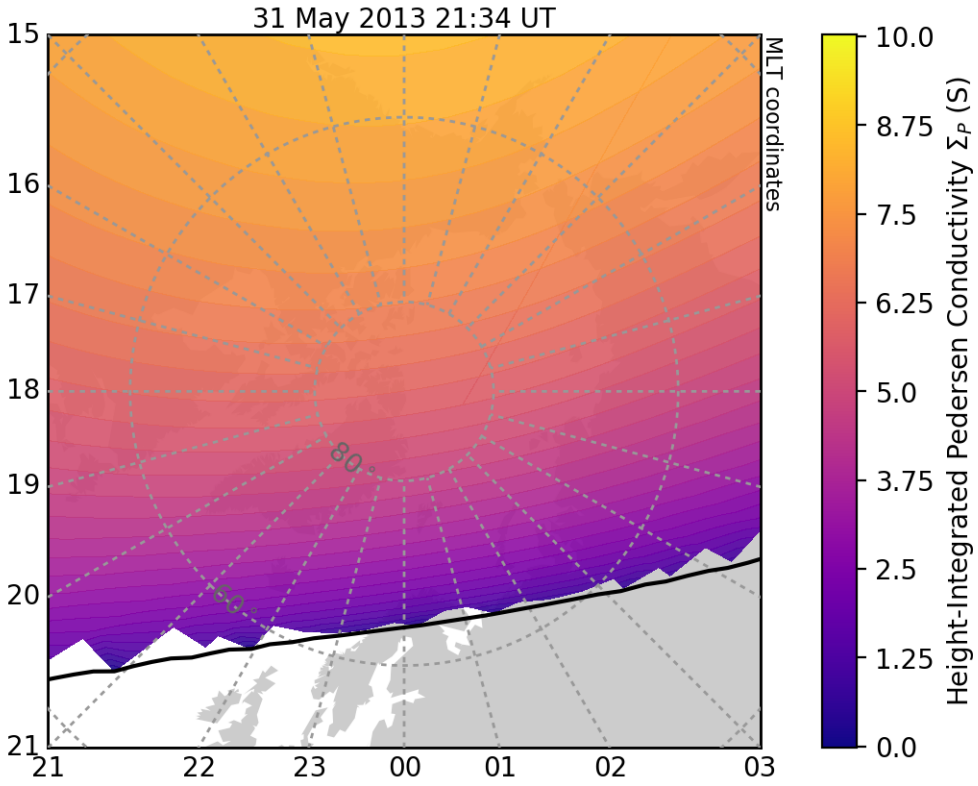

Figure 5.4: Pedersen conductance induced by photoionisation at 21:34 UT on 31 May 2013, calculated from the *Robinson and Vondrak* [1984] model. The day–night terminator is shown as a black line. Latitude circles mark 80° MLAT, 60° MLAT, and (in the corners of the figure) 40° MLAT.

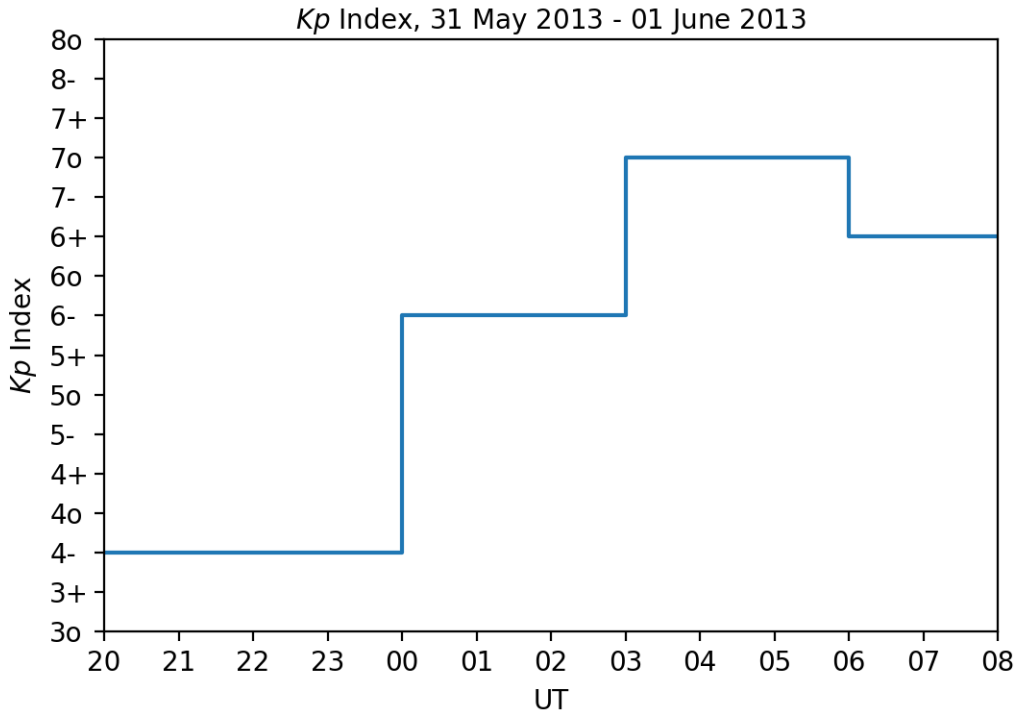

Figure 5.5: The *Kp* index from 20 UT on 31 May 2013 to 08 UT on 1 June 2013.

eorological Satellite Program (DMSP) and P78-1 satellite electron spectrometer measurements. The models are dependent upon the *Kp* (*planetarische Kennziffer*, or planetary index [Helmholtz-Zentrum Potsdam - Deutsches GeoForschungsZentrum GFZ]) geomagnetic activity index, which measures "irregular" variations in the geomagnetic field [*Bartels et al.*, 1939] and is produced for three-hour blocks of time from measurements at 13 magnetometer stations worldwide [*Menveille and Berthelier*, 1991]. The values of the *Kp* index throughout the period of study are shown in Figure 5.5. The *Kp* index data were obtained from the Helmholtz-Zentrum Potsdam - Deutsches GeoForschungsZentrum GFZ via the NASA OMNIWeb (URL: https://omniweb.gsfc.nasa.gov).

The *Hardy et al.* [1987] map of Pedersen conductance Σ_P for $Kp = 4$, to which the conditions at the time of Figure 5.3 most closely correspond, is reproduced here in Figure 5.6. For comparison, the *Hardy et al.* [1987] map of Σ_H at $Kp = 4$ is also shown.

When the SuperDARN $J_\parallel/\Sigma_P$ estimates in Figure 5.3 are compared to the modelled Pedersen conductance presented in Figures 5.4 and 5.6, it becomes apparent that $J_\parallel/\Sigma_P$ must overestimate $J_\parallel$ in large regions of the map where conductance is small, particularly in the polar cap. (This is without regard to the gradient terms of the FAC equation (2.26)). In regions of high conduct-

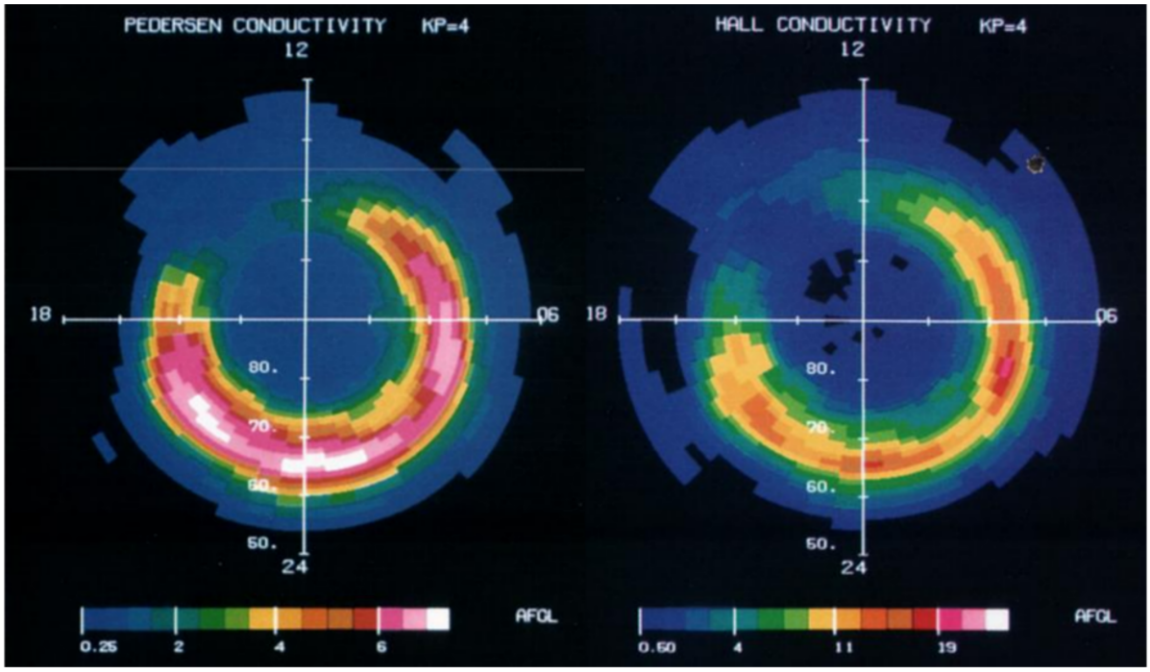

Figure 5.6: Statistically modelled height-integrated Pedersen (left) and Hall (right) conductivity induced by electron precipitation at $Kp = 4$, shown in MLT and MLAT coordinates. From *Hardy et al.* [1987], wherein it is noted of the Pedersen conductivity map, "The 16 color levels correspond to conductivities of 0.25, 0.50, 1.0, 1.5, 2.0, 2.5, 3.0, 3.5, 4.0, 4.5, 5.0, 5.5, 6.0, 7.0, 8.0, > 9.0 mhos [p. 12281]," and of the Hall conductivity map, "The 15 color levels correspond to conductivities of 0.5, 1.0, 2.0, 3.0, 4.0, 5.0, 7.0, 9.0, 11.0, 13.0, 15.0, 17.0, 19.0, 21.0, > 23.0mhos [*sic*] [p. 12279]." (The unit mho is 1/ohm, or siemens.)

ance, such as near noon (where photo-induced conductance is high), $J_\parallel/\Sigma_P$ must underestimate $J_\parallel$. The higher photo-induced conductance toward the dayside indicates that the most sunward FAC estimates are expected to be substantially more intense than those nearer the 06 MLT–18 MLT line, despite the appearance given by the $J_\parallel/\Sigma_P$ map of their being similar in magnitude. Even more notably, although the $J_\parallel/\Sigma_P$ in the midnight sector equatorward of 70° MLAT is shown as weak, when viewed in light of the modelled precipitation-induced conductance, the FAC in that region—particularly close to 65° MLAT and magnetic midnight—is expected to have magnitude comparable to the strongest dayside FAC.

The general structure of the modelled conductance is consistent with the location of measured SuperDARN data on the sunward portion of Figure 5.3, the area corresponding to the highest expected photo-induced conductance, and in the lower-latitude midnight sector, where precipitation-induced conductance should be at its largest. The location of the SuperDARN data is significant because the presence of plasma irregularities and the propagation conditions necessary to detect radar echoes from the ionosphere depend on sufficiently large electron density, which corresponds with high conductance (as shown in equation 2.10).

The Pedersen and Hall conductance plots can easily be applied to a qualitative analysis of the remaining three terms of the FAC equation (2.26) as well. The photo-induced Hall conductance is modelled simply as $\Sigma_H = 1.7\Sigma_P$, as can be seen in equation 5.1 and equation 5.2, so Figure 5.4 can be interpreted for the qualitative aspects of the Hall conductance the same as for the Pedersen conductance. The precipitation-induced Hall and Pedersen conductance also share similar structure, with the Hall again being larger.

The second term of the FAC equation (2.26) is

$$\Sigma_H \mathbf{v}_\perp \cdot \nabla_\perp B. \tag{5.3}$$

According to equation 2.28, the equation of the gradient of a dipole field, the azimuthal component of $\nabla_\perp B$ points equatorward, meaning that the largest contributions of this term to the overall FAC are in regions of meridional plasma flow with large Hall conductance. Examples of this include the antisunward plasma flow near noon where the photo-induced Hall conductance is large (for a downward contribution), and the antisunward flow near midnight where the precipitation-induced Hall conductance is large (for an upward contribution).

The third term of the FAC equation (2.26) is

$$-\mathbf{E} \cdot \nabla_{\perp} \Sigma_P \tag{5.4}$$

and the fourth term is

$$B\mathbf{v}_{\perp} \cdot \nabla_{\perp} \Sigma_H. \tag{5.5}$$

Both of these latter terms depend on conductance gradients. Gradients are found in similar locations for both Pedersen and Hall conductance, most notably at the edges of the crescent-shaped regions of particle-induced conductance, but also pointing sunward because of the photo-induced conductance. The largest contributions of the third term to the overall FAC occur where the electric field is parallel to the Pedersen conductance gradient. According to the expected electric field configuration (such as in Figure 2.10), this occurs near the edges of the photo-induced conductance in Figure 5.6. (The contribution is downward on the poleward edge and upward on the equatorward edge in the postmidnight sector, and the opposite in the premidnight sector.) The largest contributions of the fourth term are where the plasma velocity is parallel to the Hall conductance gradient, which occurs in the polar cap antisunward flow (downward contribution) and in the equatorward return flow (upward contribution), but most notably near midnight at the edges of the precipitation-induced conductance (upward on the poleward side and downward on the equatorward side).

5.3 The Transition from Northward to Southward IMF

At approximately 01:18 UT on 1 June 2013, the IMF changed quickly from strongly northward to strongly southward. Estimates of $J_{\parallel}/\Sigma_P$ from SuperDARN are presented in Figures 5.7 to 5.9, covering the two-minute intervals between 01:16 UT and 01:22 UT.

The estimates of $J_{\parallel}/\Sigma_P$ from SuperDARN over the 01:16 UT to 01:18 UT interval are shown in Figure 5.7. Northward IMF dominates at this time, as it has for approximately the past two hours. There are two FAC regions of note in the noon sector: a postnoon region of down FAC (blue) and a prenoon region of up FAC (red). Both regions extend from the pole to 80° MLAT and from 08 MLT to 16 MLT, with the meridional boundary between the two FAC regions situated just prior to magnetic local noon. Although only the duskward edge of the down FAC region is well supported by measured SuperDARN velocity data (showing antisunward flow in the dusk cell),

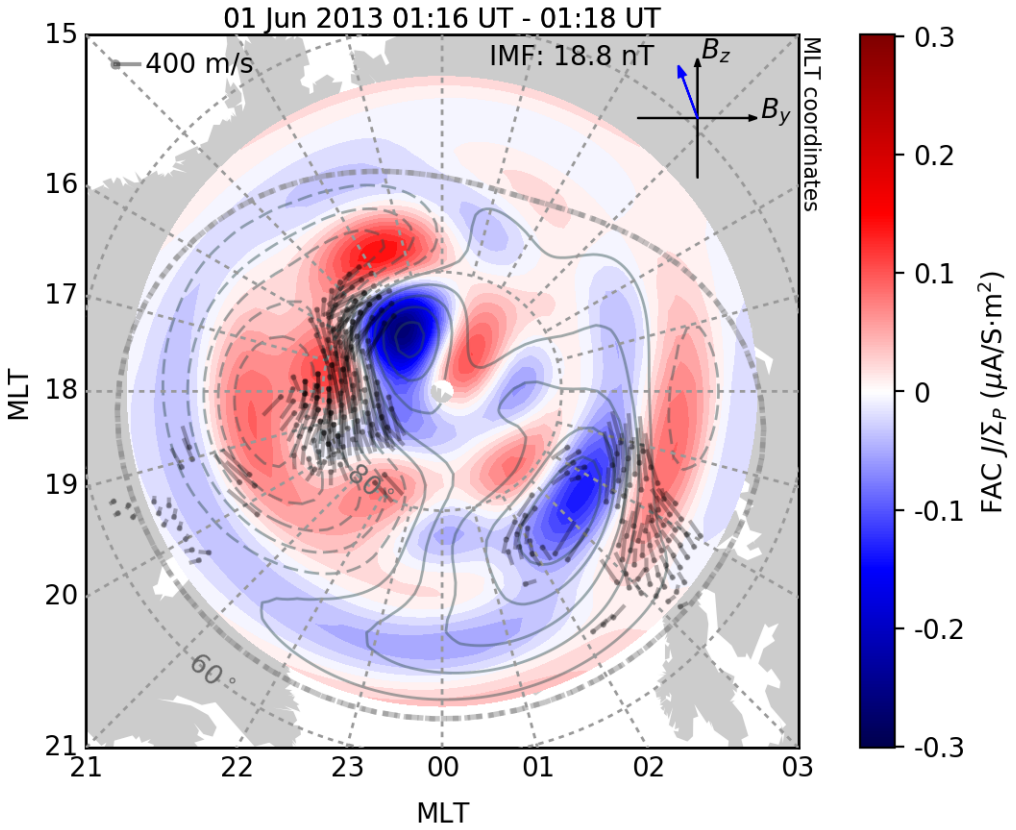

Figure 5.7: SuperDARN $J_{\parallel}/\Sigma_P$ estimates in the 01:16 UT to 01:18 UT interval on 1 June 2013, in MLAT–MLT coordinates. $J_{\parallel}/\Sigma_P$ is shown as a heat map, with red representing upward (positive) FAC and blue representing downward (negative) FAC and the colour intensity scaling with the intensity of $J_{\parallel}/\Sigma_P$ as shown by the colour bar at the right of the figure. True vectors (of plasma velocity) are overlaid as grey barbs pointing in the direction of flow. Barb length is proportional to speed, and a scale sample barb of length 400 m/s is plotted at the upper left corner of the figure. MLT lines and MLAT curves (at 60° MLAT and 80° MLAT) are marked with short-dashed lines. The positive and negative potential contours and the HMB are plotted as solid, long-dashed, and heavy dotted curves, respectively, and the IMF projection on the GSM y–z plane is plotted in the upper right corner with the projected magnitude annotated along the top of the figure.

the two regions are consistent with a pair of plasma circulation cells featuring sunward flow at magnetic noon and antisunward flow around the outer edges. This so-called reverse convection in the polar cap is typical for persistent northward IMF conditions. An example of reverse convection cells observed by *Huang et al.* [2000] using SuperDARN is shown in Figure 5.10.

Northward IMF conditions produce reverse convection cells in the dayside polar cap ionosphere, while the nightside ionosphere is controlled by the dynamics of the magnetotail to which it is connected. Because of this, the nightside ionosphere in Figure 5.7 shows a behaviour not unlike the nightside portion of the two-cell convection pattern in Figure 5.3, which is expected when reconnection is occurring in the magnetotail. A region of downward FAC appears in the postmidnight sector, from 02 MLT to 06 MLT and from approximately 70° MLAT to 80° MLAT. This FAC corresponds to a counter-clockwise circulation in the plasma flow that is well-supported by SuperDARN data. Equatorward of this FAC region is a broad sunward flow channel, dividing the downward FAC from an upward FAC region that extends from 03 MLT to 08 MLT between approximately 65° MLAT and 70° MLAT. This FAC pair relates well to the region 1 and region 2 FACs and resembles the FAC pair in a similar location shown in Figure 5.3.

The dusk ionosphere contains an FAC pair that corresponds to the region 1 and region 2 FACs, with a large upward FAC region above 70° MLAT that extends from magnetic noon to 23 MLT and reaches the equatorward boundary of the polar cap reverse-convection FAC cell at approximately 82° MLAT. This upward FAC region is expected because of SuperDARN's clockwise circulation. The region 1 FAC is paired on the equatorward side with a downward region 2 FAC that extends from 10 MLT around the duskside until joining with the intense downward $J_{\parallel}/\Sigma_P$ centred at 03 MLT, and reaches as far down in latitude as 65° MLAT.

The IMF was midway through its change from northward to southward IMF at 01:18 UT, and $J_{\parallel}/\Sigma_P$ estimated from SuperDARN data over the following two-minute interval is presented in Figure 5.8. The projection of the IMF on the GSM y-z plane, pointing almost directly in the dawnward ($-y$) direction, is shown in the upper right corner of the figure. The large region 1 FAC on the duskside of Figure 5.7 is still present, extending from 11 MLT to 0 MLT and from 82° MLAT to 72° MLAT. Between the dusk region 1 FAC and the pole, the downward FAC remains, centred at 15 MLT and 84 MLAT, but the prenoon reverse convection upward FAC previously paired with it has all but disappeared. Instead, a large downward region of FAC (the development of dayside

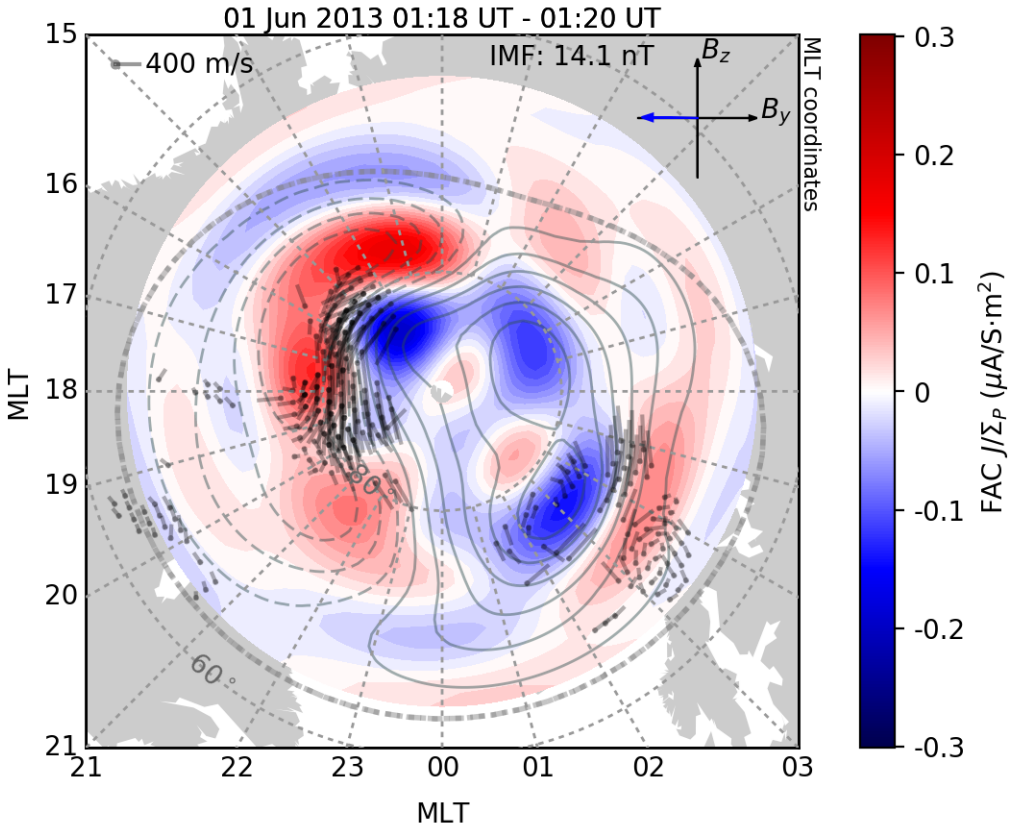

Figure 5.8: SuperDARN $J_{\parallel}/\Sigma_P$ estimates in the 01:18 UT to 01:20 UT interval on 1 June 2013, in MLAT–MLT coordinates. $J_{\parallel}/\Sigma_P$ is shown as a heat map, with red representing upward (positive) FAC and blue representing downward (negative) FAC and the colour intensity scaling with the intensity of $J_{\parallel}/\Sigma_P$ as shown by the colour bar at the right of the figure. True vectors (of plasma velocity) are overlaid as grey barbs pointing in the direction of flow. Barb length is proportional to speed, and a scale sample barb of length 400 m/s is plotted at the upper left corner of the figure. MLT lines and MLAT curves (at 60° MLAT and 80° MLAT) are marked with short-dashed lines. The positive and negative potential contours and the HMB are plotted as solid, long-dashed, and heavy dotted curves, respectively, and the IMF projection on the GSM y–z plane is plotted in the upper right corner with the projected magnitude annotated along the top of the figure.

prenoon region 1 FAC) has appeared, centred at 08 MLT and 82° MLAT and extending across four hours of the dawnside. The change in the sense of the prenoon region 1 FAC, although not supported by measured SuperDARN data in the area, is nevertheless consistent with the beginning of an ionospheric reconfiguration in response to the change in IMF conditions. Early in the process there is still significant influence from the northward IMF on the appearance of the FAC and on the convection pattern of the ionosphere. Information about the change propagates at the plasma flow speed across the polar cap (in this case, typically 200 m/s to 400 m/s). The effects of the change have not yet had time to travel far into the polar cap.

As in Figure 5.7, a large region of downward region 1 FAC (well supported by measured velocity data) is present in the postmidnight sector, centred at 03:30 MLT and 75° MLAT, and its upward region 2 counterpart is also present at lower latitudes, as expected.

The IMF was strongly southward by 01:20 UT. $J_{\parallel}/\Sigma_P$ estimated from SuperDARN data over the following two-minute interval is presented in Figure 5.9. The upward region 1 FAC on the duskside has changed little, but the downward FAC of the former reverse convection cell has moved antisunward and is now centred at 17 MLT and 85° MLAT. The dawn convection cell, centred at 05 MLT and 85° MLAT, is making a transition to a round shape. The dawn cell includes the well-established postmidnight sector region 1 downward FAC (which has not moved, and is still well supported by measured SuperDARN data) and a prenoon downward region 1 FAC centred at 08:30 MLT and 80° MLAT. The round cell still contains some weak upward FAC in parts of the polar cap between the three main intense downward FAC regions, similar to the case in Figure 5.3. In the 01:20 UT map, however, there is measured data support for clockwise circulation at 06 MLT and 80° MLAT, which may be a relic of the former northward IMF conditions. Significant reconfiguration has already taken place in response to the southward turning of the IMF, but the ionosphere still takes time to respond completely. The polar cap displays a time-history of the IMF orientation as the open lobe flux transits the polar cap to the nightside.

Eight minutes later, in the 01:28 UT to 01:30 UT interval, the ionosphere has reconfigured to a two-cell convection pattern, as shown in Figure 5.11. The potential contours reveal the two-cell pattern well, and the plasma flow data show a large region of clockwise circulation covering the duskside as far as the pole, centred at 17 MLT and 77° MLAT, and a large region of counterclockwise circulation covering the dawnside, centred near 04:30 MLT and 73° MLAT. The SuperDARN

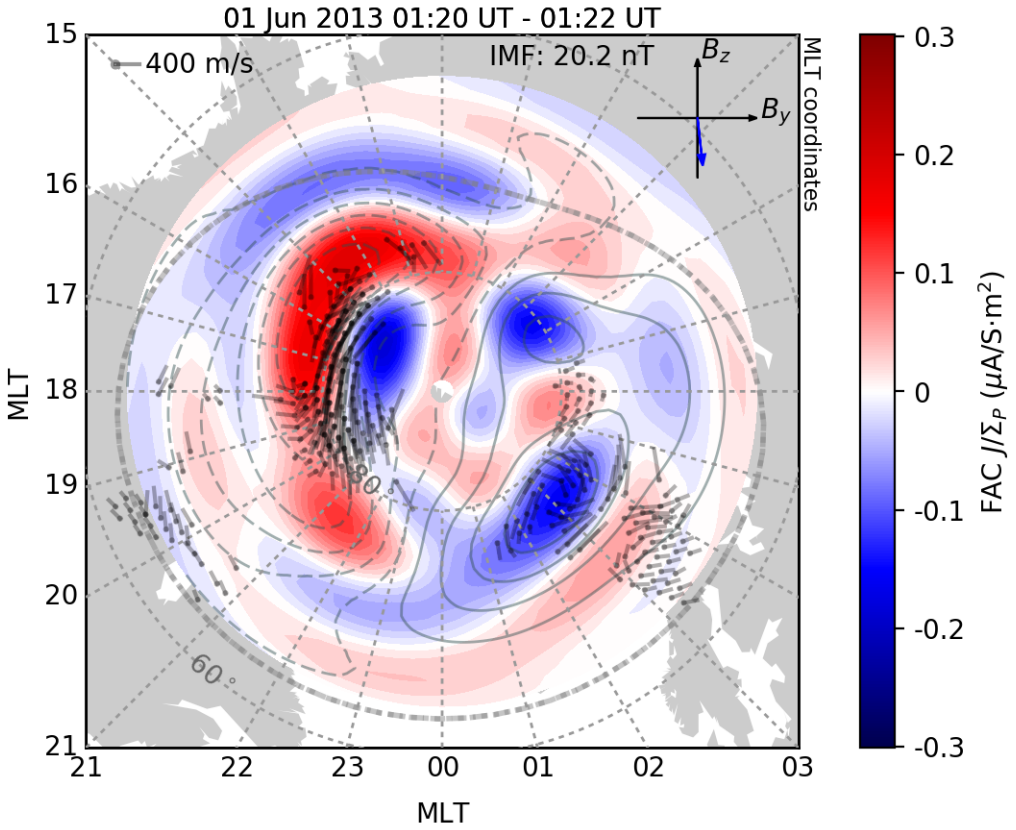

Figure 5.9: SuperDARN $J_{\parallel}/\Sigma_P$ estimates in the 01:20 UT to 01:22 UT interval on 1 June 2013, in MLAT–MLT coordinates. $J_{\parallel}/\Sigma_P$ is shown as a heat map, with red representing upward (positive) FAC and blue representing downward (negative) FAC and the colour intensity scaling with the intensity of $J_{\parallel}/\Sigma_P$ as shown by the colour bar at the right of the figure. True vectors (of plasma velocity) are overlaid as grey barbs pointing in the direction of flow. Barb length is proportional to speed, and a scale sample barb of length 400 m/s is plotted at the upper left corner of the figure. MLT lines and MLAT curves (at 60° MLAT and 80° MLAT) are marked with short-dashed lines. The positive and negative potential contours and the HMB are plotted as solid, long-dashed, and heavy dotted curves, respectively, and the IMF projection on the GSM y–z plane is plotted in the upper right corner with the projected magnitude annotated along the top of the figure.

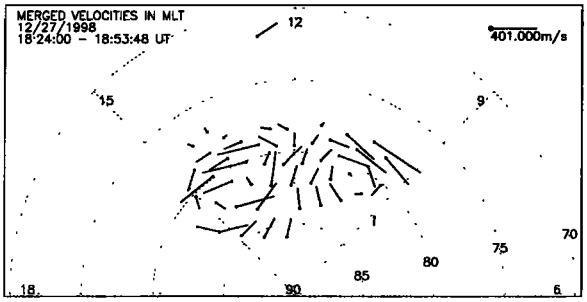

Figure 5.10: Reverse convection cells observed by SuperDARN near noon during northward IMF conditions. From *Huang et al.* [2000].

FAC pattern has an intense upward region 1 FAC centred on the dusk convection cell, as expected, and a moderately intense downward region 1 FAC centred on the dawn convection cell, also as expected. In the centre of the polar cap, near the pole, smaller regions of upward and downward FAC appear in areas of velocity shear, but when the low conductance in this region is considered the actual FAC intensity is expected to be smaller.

Equatorward of the region 1 FACs in Figure 5.11 are the oppositely-directed region 2 FACs, upward on the dawnside and downward on the duskside, as expected. These regions extend from approximately 70° MLAT to the edge of the convection map (where velocity is set to zero and the FAC pattern is thereby cut off). The upward and downward region 2 FACs exist latitudinally side-by-side near magnetic noon, with the upward region 2 FAC from the dawnside situated at lower latitudes. A similar overlap is seen near 22 MLT, with the downward region 2 FAC from the duskside located at lower latitudes. Closer to 23 MLT is the region 1 FAC pattern of the duskside convection reversal, where the antisunward plasma flow turns to begin sunward flow at approximately 65° MLAT. The upward region 1 FAC centred on the dusk convection reversal is bracketed at higher and lower latitudes by downward FAC regions.

In conclusion, this case study shows that maps of FAC estimates computed using the Super-DARN potential function method are useful in studies of the magnetosphere and ionosphere. With a demonstration of the interpretation of the maps, it has been shown that the results are readily compared with other ionospheric measurements and with the predictions of models and theory.

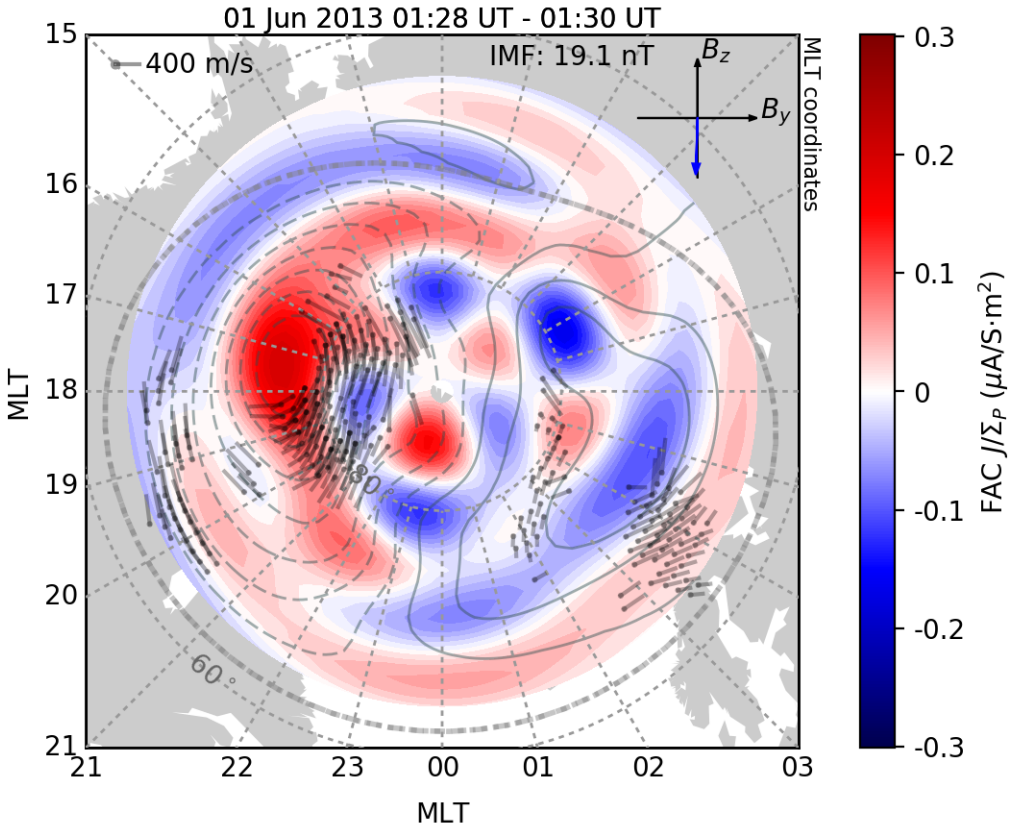

Figure 5.11: SuperDARN $J_{\parallel}/\Sigma_P$ estimates in the 01:28 UT to 01:30 UT interval on 1 June 2013, in MLAT–MLT coordinates. $J_{\parallel}/\Sigma_P$ is shown as a heat map, with red representing upward (positive) FAC and blue representing downward (negative) FAC and the colour intensity scaling with the intensity of $J_{\parallel}/\Sigma_P$ as shown by the colour bar at the right of the figure. True vectors (of plasma velocity) are overlaid as grey barbs pointing in the direction of flow. Barb length is proportional to speed, and a scale sample barb of length 400 m/s is plotted at the upper left corner of the figure. MLT lines and MLAT curves (at 60° MLAT and 80° MLAT) are marked with short-dashed lines. The positive and negative potential contours and the HMB are plotted as solid, long-dashed, and heavy dotted curves, respectively, and the IMF projection on the GSM y–z plane is plotted in the upper right corner with the projected magnitude annotated along the top of the figure.

CHAPTER 6

CONCLUSION

A new technique is presented for estimating the ionospheric FAC pattern directly from SuperDARN fitted electrostatic potential functions. At its core, the technique uses an equation that has been derived to calculate estimates of FAC $J_{\parallel}$ per unit of ionospheric Pedersen conductance Σ_P using the potential function Φ obtained from SuperDARN:

$$\frac{J_{\parallel}}{\Sigma_P} \approx \frac{1}{r^2 \sin\vartheta} \left(\cos\vartheta \frac{\partial}{\partial\vartheta}\Phi + \sin\vartheta \frac{\partial^2}{\partial\vartheta^2}\Phi + \frac{1}{\sin\vartheta} \frac{\partial^2}{\partial\varphi^2}\Phi \right). \tag{4.16}$$

The derivatives of the potential function have also been derived based on the expression of the potential presently used in SuperDARN potential function fitting.

A comparison with FAC measured by the AMPERE experiment has found that, even without knowledge of the ionospheric conductivity distribution, there was reasonable agreement between the radar-based $J_{\parallel}/\Sigma_P$ and the satellite-based $J_{\parallel}$ in location and sense, but with some differences in magnitude. Having demonstrated the basic applicability of the concept through comparisons with accepted methods of $J_{\parallel}/\Sigma_P$ estimation from SuperDARN data and from AMPERE satellite data, the potential calculation technique was applied to a case study of a dynamic geomagnetic event that occurred from 31 May to 1 June 2013. The technique was generally accurate in that it determined FAC location and sense consistent with what was expected for the prevailing solar wind conditions based on existing observations and models.

An important consequence of this work is to show the utility of SuperDARN for the study of magnetospheric dynamics. SuperDARN is capable of discerning the ionospheric electric field, ionospheric plasma convection, and estimating FAC on a hemispheric scale. These are indicators of magnetospheric activity that are measurable at ionospheric altitudes. What is more, with its

short time resolution and broad spatial coverage, SuperDARN provides a wide "view" of magnetospheric dynamics. For example, near substorm onset in the midnight sector, the convection patterns measured by SuperDARN have enough similarity that *Bristow and Jensen* [2007] were able to perform a superposed epoch study including 10 unrelated substorm events. However, as the focus of this thesis is to discuss the new SuperDARN $J_{\parallel}/\Sigma_P$ estimation technique, not magnetospheric physics, the technique is highlighted while the physics discussed is limited. Detailed study of parameters (such as ionospheric conductivity) or dynamics (such as the development of FAC patterns in response to changing IMF conditions) is left for future studies, although preliminary, qualitative comparisons are made with established results in such areas to show that the SuperDARN method is sufficiently consistent to warrant further study.

The technique of estimating $J_{\parallel}/\Sigma_P$ directly from SuperDARN electrostatic potential functions has its main strengths in its fast cadence and in its broad spatial coverage that has spatial resolution as fine as 100 km. The technique is also versatile. Should the underlying mathematical basis set for the expression of the electrostatic potential be changed with improvements to the SuperDARN fitting procedure or for individual studies, the technique presented in this thesis may be applied directly to the new potential formulations.

The main weaknesses of the SuperDARN approach to FAC estimation are its lack of conductivity information, which limits the estimates of FAC to $J_{\parallel}/\Sigma_P$ rather than $J_{\parallel}$, and its dependence on the SuperDARN statistical convection model for data in regions that have poor radar scattering conditions or have no radar coverage. Ways in which both of these limitations may be addressed are described in Section 6.1.

The SuperDARN $J_{\parallel}/\Sigma_P$ estimation technique presented in this thesis is well-suited to examination of FACs for studies of particle dynamics, substorms and storms, and other phenomena. It is easily applied to standard SuperDARN data products and, with its adaptability, should prove useful for space physics research for years to come.

6.1 Future Work

As described in Section 4.2, the method of stretching the potential basis functions used in the SuperDARN fitting process introduces error in the fitted potential. An earlier, more complicated

spherical cap harmonics fitting method [*Haines*, 1985, 1988] is available for sparse data that are not spread across a hemisphere, such as that encountered in SuperDARN fitting. *Green et al.* [2006] used this method to analyse Iridium satellite magnetometer data (that is, AMPERE data), noting that spherical cap harmonics fitting does not have the shortcomings of the stretching method of *De Santis* [1992] and *Ruohoniemi and Baker* [1998]. Spherical cap harmonics have already been used by *Fiori* [2011], for example, to analyse SuperDARN data, and provide a promising alternative to the standard SuperDARN fitting method with the advent of less costly and more capable computers since 1998. Data processing, such as for FACs, could be done straightforwardly using spherical cap harmonics fitting without the reservations expressed by *Green et al.* [2006].

The study of FACs could be advanced by building on the methods described in this thesis and by adding new methods and other instruments. Further studies could include:

- Data from other instruments such as optical aurora cameras, magnetometers, incoherent scatter radars, and satellites could be incorporated along with $J_{\parallel}/\Sigma_P$ patterns. Optical and incoherent scatter radar measurements, in particular, can be used to estimate conductance [e.g., *Sears and Vondrak*, 1981] in order to obtain estimates of the full FAC from SuperDARN observations of the electrostatic potential Φ and ionospheric bulk plasma convection velocity $\mathbf{v}_{cnv}$.

- Combining theoretical or empirical conductivity profiles with SuperDARN $J_{\parallel}/\Sigma_P$ estimates for comparison with AMPERE and other FAC measurements could also be profitable. Long integration periods would likely provide the best results when using conductance models.

- SuperDARN $J_{\parallel}/\Sigma_P$ estimates could be combined with other sources of FAC or flow vorticity estimates, such as AMPERE, to estimate conductance. For example, *Green et al.* [2007] used SuperDARN, various satellites, and ground magnetometers to perform such a task, but methods using the new SuperDARN $J_{\parallel}/\Sigma_P$ method based on potential functions could prove simpler.

REFERENCES

Akasofu, S.-I. (1964), The development of the auroral substorm, *Planet. Space Sci.*, *12*(4), 273–282.

Anderson, B. J., K. Takahashi, and B. A. Toth (2000), Sensing global Birkeland currents with Iridium® engineering magnetometer data, *Geophys. Res. Lett.*, *27*(24), 4045–4048.

Anderson, B. J., H. Korth, C. L. Waters, D. L. Green, and P. Stauning (2008), Statistical Birkeland current distributions from magnetic field observations by the Iridium constellation, *Ann. Geophys.*, *26*(3), 671–687, doi:10.5194/angeo-26-671-2008.

Appleton, E. V. (1925), Geophysical influences on the transmission of wireless waves, *Proc. Phys. Soc.*, *37*, 16D–22D.

Baker, K. B., and S. Wing (1989), A new magnetic coordinate system for conjugate studies at high latitudes, *J. Geophys. Res.*, *94*(A7), 9139–9143, doi:10.1029/JA094iA07p09139.

Bartels, J., N. H. Heck, and H. F. Johnston (1939), The three-hour-range index measuring geomagnetic activity, *Terr. Magn. Atmos. Electr.*, *44*(4), 411–454, doi:10.1029/TE044i004p00411.

Baumjohann, W., and R. A. Treumann (1997), *Basic Space Plasma Physics*, Imperial College Press, London.

Birn, J. (2007), Earth's magnetosphere, in *Reconnection of Magnetic Fields: Magnetohydrodynamics and Collisionless Theory and Observations*, edited by J. Birn and E. R. Priest, pp. 8–15, Cambridge University Press, Cambridge.

Boström, R. (1973), Electrodynamics of the ionosphere, in *Cosmical Geophysics*, pp. 181–192, Universitetsforlaget, Oslo.

Boström, R. (1974), Ionosphere-magnetosphere coupling, in *Magnetospheric Physics*, *Astrophysics and Space Science Library*, vol. 44, edited by B. M. McCormac, pp. 45–59, Reidel, Dordrecht; Boston.

Bristow, W. A., and P. Jensen (2007), A superposed epoch study of SuperDARN convection observations during substorms, *J. Geophys. Res.*, *112*(A6), A06232, doi:10.1029/2006JA012049.

Carlson, H. C., Jr., and A. Egeland (1995), The aurora and the auroral ionosphere, in *Introduction to Space Physics*, edited by M. G. Kivelson and C. T. Russell, pp. 459–502, Cambridge University Press, New York.

Chapman, S. (1931), The absorption and dissociative or ionizing effect of monochromatic radiation in an atmosphere on a rotating earth, *Proc. Phys. Soc.*, *43*, 26–45.

Chapman, S. (1935), The electric current-systems of magnetic storms, *Terr. Magn. Atmos. Electr.*, *40*(4), 349–370.

Chapman, S., and V. C. A. Ferraro (1930), A new theory of magnetic storms, *Nature*, *126*(3169), 129–130.

Chisham, G., M. Lester, S. E. Milan, M. P. Freeman, W. A. Bristow, A. Grocott, K. A. McWilliams, J. M. Ruohoniemi, T. K. Yeoman, P. L. Dyson, R. A. Greenwald, T. Kikuchi, M. Pinnock, J. P. S. Rash, N. Sato, G. J. Sofko, J.-P. Villain, and A. D. M. Walker (2007), A decade of the Super Dual Auroral Radar Network (SuperDARN): Scientific achievements, new techniques and future directions, *Surv. Geophys.*, *28*(1), 33–109, doi:10.1007/s10712-007-9017-8.

Cowley, S. W. H. (1986), Magnetic reconnection, in *Solar System Magnetic Fields*, edited by E. R. Priest, p. 121, Reidel, Dodrecht.

Cowley, S. W. H. (2000), Magnetosphere–ionosphere interactions: A tutorial review, in *Magnetospheric Current Systems*, *Geophys. Monogr. Ser.*, vol. 118, edited by S.-I. Ohtani, R. Fujii, M. Hesse, and R. L. Lysak, pp. 91–106, American Geophysical Union, doi: 10.1029/GM118p0091.

De Santis, A. (1992), Conventional spherical harmonic analysis for regional modelling of the geomagnetic field, *Geophys. Res. Lett.*, *19*(10), 1065–1067.

deBlank, H. J. (2006), Guiding center motion, *Fusion Science and Technology*, *49*(2T), 59–66.

Dungey, J. W. (1961), Interplanetary magnetic field and the auroral zones, *Phys. Rev. Lett.*, *6*(2), 47–48, doi:10.1103/PhysRevLett.6.47.

Eriksson, S., J. W. Bonnell, L. G. Blomberg, R. E. Ergun, G. T. Marklund, and C. W. Carlson (2002), Lobe cell convection and field-aligned currents poleward of the region 1 current system, *J. Geophys. Res.*, *107*(A8), 1185, doi:10.1029/2001JA005041.

Fiori, R. A. D. (2011), Application of spherical cap harmonic analysis to plasma convection mapping at high latitudes, Ph.D. thesis, University of Saskatchewan.

Green, D. L., C. L. Waters, B. J. Anderson, H. Korth, and R. J. Barnes (2006), Comparison of large-scale Birkeland currents determined from Iridium and SuperDARN data, *Ann. Geophys.*, *24*(3), 941–959, doi:10.5194/angeo-24-941-2006.

Green, D. L., C. L. Waters, H. Korth, B. J. Anderson, A. J. Ridley, and R. J. Barnes (2007), Technique: Large-scale ionospheric conductance estimated from combined satellite and ground-based electromagnetic data, *J. Geophys. Res.*, *112*, A05343, doi:10.1029/2006JA012069.

Greenwald, R. A., K. B. Baker, J. R. Dudeney, M. Pinnock, T. B. Jones, E. C. Thomas, J.-P. Villain, J.-C. Cerisier, C. Senior, C. Hanuise, R. D. Hunsucker, G. Sofko, J. Koehler, E. Nielsen, R. Pellinen, A. D. M. Walker, N. Sato, and H. Yamagishi (1995), DARN/SuperDARN: A

global view of the dynamics of high-latitude convection, *Space Sci. Rev.*, *71*(1-4), 761–796, doi:10.1007/BF00751350.

Haines, G. V. (1985), Spherical cap harmonic analysis, *J. Geophys. Res. Solid Earth*, *90*(B3), 2583–2591.

Haines, G. V. (1988), Computer programs for spherical cap harmonic analysis of potential and general fields, *Computers and Geosciences*, *14*(4), 413–447.

Hardy, D. A., M. S. Gussenhoven, R. Raistrick, and W. J. McNeil (1987), Statistical and functional representations of the pattern of auroral energy flux, number flux, and conductivity, *J. Geophys. Res.*, *92*(A11), 12,275–12,294.

Hartree, D. R. (1931), The propagation of electromagnetic waves in a refracting medium in a magnetic field, *Proc. Camb. Phil. Soc.*, *27*(1), 143–162.

Helmholtz-Zentrum Potsdam - Deutsches GeoForschungsZentrum GFZ (2015), Geomagnetic Kp index, URL: http://www.gfz-potsdam.de/en/section/earths-magnetic-field/data-products-services/kp-index/explanation, retrieved 07 May 2017.

Heppner, J. P., and N. C. Maynard (1987), Empirical high-latitude electric field models, *J. Geophys. Res.*, *92*(A5), 4467–4489.

Huang, C.-S., D. A. Andre, G. J. Sofko, and A. V. Kustov (2000), Super Dual Auroral Radar Network observations of ionospheric multicell convection during northward interplanetary magnetic field, *J. Geophys. Res.*, *105*(A4), 7419–7428, doi:10.1029/1999JA000364.

Hughes, W. J. (1995), The magnetopause, magnetotail, and magnetic reconnection, in *Introduction to Space Physics*, edited by M. G. Kivelson and C. T. Russell, pp. 227–287, Cambridge University Press, New York.

Hunter, J. D. (2007), Matplotlib: A 2D graphics environment, *Computing In Science & Engineering*, *9*(3), 90–95, doi:10.1109/MCSE.2007.55.

Iijima, T., and T. A. Potemra (1976a), Field-aligned currents in the dayside cusp observed by Triad, *J. Geophys. Res.*, *81*(34), 5971–5979.

Iijima, T., and T. A. Potemra (1976b), The amplitude distribution of field-aligned currents at northern high latitudes observed by Triad, *J. Geophys. Res.*, *81*(13).

Jackson, J. D. (1975), *Classical Electrodynamics*, 2nd ed., John Wiley & Sons, Inc., New York.

Kamide, Y., A. D. Richmond, and S. Matsushita (1981), Estimation of ionospheric electric fields, ionospheric currents, and field-aligned currents from ground magnetic records, *J. Geophys. Res.*, *86*(A2), 801–813.

King, J., and N. Papitashvili (n.d.), One min and 5-min solar wind data sets at the earth's bow shock nose, URL: https://omniweb.gsfc.nasa.gov/html/HROdocum.html, retrieved 22 April 2017.

Kivelson, M. G. (1995), Physics of space plasmas, in *Introduction to Space Physics*, edited by M. G. Kivelson and C. T. Russell, pp. 27–57, Cambridge University Press, New York.

Lennartsson, W., and R. D. Sharp (1982), A comparison of the 0.1–17 keV/e ion composition in the near equatorial magnetosphere between quiet and disturbed conditions, *J. Geophys. Res.*, *87*(A8), 6109–6120.

Luhmann, J. G. (1995), Ionospheres, in *Introduction to Space Physics*, edited by M. G. Kivelson and C. T. Russell, pp. 183–202, Cambridge University Press, New York.

McPherron, R. L. (1970), Growth phase of magnetospheric substorms, *J. Geophys. Res.*, *75*(28), 5592–5599.

McPherron, R. L. (1995), Magnetospheric dynamics, in *Introduction to Space Physics*, edited by M. G. Kivelson and C. T. Russell, pp. 400–458, Cambridge University Press, New York.

McWilliams, K. A. (1997), A SuperDARN study of dayside field-aligned current regions, Master's thesis, University of Saskatchewan.

McWilliams, K. A. (2001), Ionospheric signatures of dayside reconnection processes, Ph.D. thesis, University of Leicester.

Menveille, M., and A. Berthelier (1991), The *K*-derived planetary indices: Description and availability, *Rev. Geophys.*, *29*(3), 415–432.

Nosé, M., T. Iyemori, Y. Odagi, M. Takeda, H. Toh, Y. Koyama, and N. Takeuchi (2012), *High-Time Resolution Geomagnetic Indices: AE, ASY, Wp, and SYM, No. 1: 2009*, Data Analysis Center for Geomagnetism and Space Magnetism, Graduate School of Science, Kyoto University, Kyoto, Japan.

Parker, E. N. (1958), Dynamics of the interplanetary gas and magnetic fields, *Astryphys. J.*, *128*(3), 664–676.

Parker, E. N. (1965), Dynamical theory of the solar wind, *Space Sci. Rev.*, *4*(5–6), 666–708.

Petschek, H. E. (1964), Magnetic field annihilation, in *The Physics of Solar Flares*, vol. NASA SP-50, edited by W. N. Hess, p. 425, NASA, Washington, DC.

Press, W. H., S. A. Teukolsky, W. T. Vetterling, and B. P. Flannery (1992), *Numerical Recipes in C*, 2nd ed., Cambridge Univ. Press, New York.

Robinson, R. M., and R. R. Vondrak (1984), Measurements of *E* region ionization and conductivity produced by solar illumination at high latitudes, *J. Geophys. Res.*, *89*(A6), 3951–3956.

Ruohoniemi, J. M., and K. B. Baker (1998), Large-scale imaging of high-latitude convection with Super Dual Auroral Radar Network HF radar observations, *J. Geophys. Res.*, *103*(A9), 20,797–20,811.

Ruohoniemi, J. M., R. A. Greenwald, K. B. Baker, J.-P. Villain, C. Hanuise, and J. Kelly (1989), Mapping high-latitude plasma convection with coherent HF radars, *J. Geophys. Res.*, *94*(A10), 13,463–13,477.

Russell, C. T. (1995), A brief history of solar–terrestrial physics, in *Introduction to Space Physics*, edited by M. G. Kivelson and C. T. Russell, pp. 1–26, Cambridge University Press, New York.

Schunk, R. W., and A. F. Nagy (1999), *Ionospheres: Physics, Plasma Physics, and Chemistry*, Cambridge Atmospheric and Space Science Series, 2nd ed., Cambridge University Press, Cambridge.

Sears, R. D., and R. R. Vondrak (1981), Optical emissions and ionization profiles during an intense pulsating aurora, *J. Geophys. Res.*, *86*(A8), 6853–6858.

Shepherd, S. G., and J. M. Ruohoniemi (2000), Electrostatic potential patterns in the high-latitude ionosphere constrained by SuperDARN measurements, *J. Geophys. Res.*, *105*(A10), 23,005–23,014.

Siscoe, G. L. (1983), Solar system magnetohydrodynamics, in *Solar-Terrestrial Physics: Principles and Theoretical Foundations*, *Astrophysics and Space Science Library*, vol. 104, edited by R. L. Carovillano and J. M. Forbes, pp. 11–100, D. Reidel Publishing Company, Dordrecht.

Sofko, G. J., R. Greenwald, and W. Bristow (1995), Direct determination of large-scale magnetospheric field-aligned currents with SuperDARN, *Geophys. Res. Lett.*, *22*(15), 2041–2044.

Speiser, T. W. (1971), The Dungey model of the magnetosphere, and astro-geophysical current sheets, *Radio Sci.*, *6*(2), 315–319.

Villain, J. P., R. André, C. Hanuise, and D. Grésillon (1996), Observation of the high-latitude ionosphere by HF radars: interpretation in terms of collective wave scattering and characterization of turbulence, *J. Atmos. Terr. Phys.*, *58*(8/9), 943–958.

Walker, A. D. M., and G. J. Sofko (2016), Mapping of steady-state electric fields and convective drifts in geomagnetic fields – Part 1: Elementary models, *Ann. Geophys.*, *34*(1), 55–65, doi: 10.5194/angeo-34-55-2016.

Watanabe, M., and G. J. Sofko (2009), Role of interchange reconnection in convection at small interplanetary magnetic field clock angles and in transpolar arc motion, *J. Geophys. Res.*, *114*(A1), A01209, doi:10.1029/2008JA013426.

Wehner, D. R. (1987), *High Resolution Radar*, Artech House, Norwood, MA.

Wolf, R. A. (1995), Magnetospheric configuration, in *Introduction to Space Physics*, edited by M. G. Kivelson and C. T. Russell, pp. 288–329, Cambridge University Press, New York.

Woodman, R. F., and T. Hagfors (1969), Methods for the measurement of vertical ionospheric motions near the magnetic equator by incoherent scattering, *J. Geophys. Res.*, *74*(5), 1205–1212.

APPENDIX A

GEOCENTRIC SOLAR MAGNETOSPHERIC COORDINATES

In magnetospheric studies it is convenient to use Geocentric Solar Magnetospheric coordinates. This is a system centred on the Earth where the $\hat{x}$ basis vector points toward the Sun, the $\hat{y}$ basis vector is defined by $\hat{y} = \hat{x} \times \vec{\mu} / |\vec{\mu}|$ (where $\vec{\mu}$ is the magnetic dipole vector of the Earth), and the $\hat{z}$ basis vector is defined by $\hat{z} = \hat{x} \times \hat{y}$. Therefore, the z direction points generally northward and the x-z plane contains the magnetic dipole axis. A sketch is shown in Figure A.1.

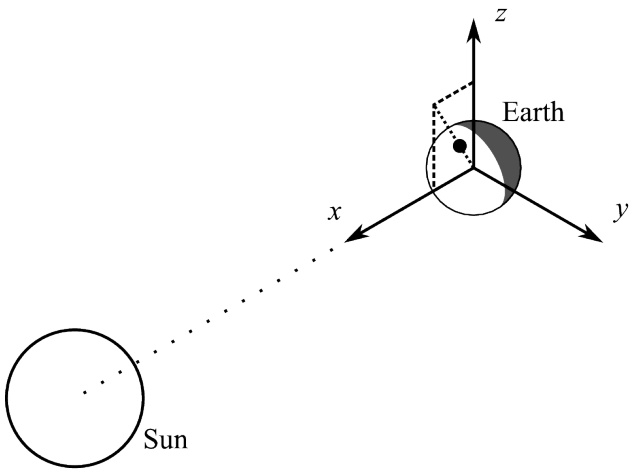

Figure A.1: The Geocentric Solar Magnetospheric coordinate system. (Not to scale.) The large black dot marks the magnetic north pole.

APPENDIX B

DERIVATIONS

B.1 Plasma Drift for a General External Force

A particle that has mass m, charge q, and velocity $\mathbf{v}$ and is subject to a magnetic field $\mathbf{B}$ and a general force $\mathbf{F}$ will have the equation of motion

$$m\dot{\mathbf{v}} = \mathbf{F} + q\mathbf{v} \times \mathbf{B}. \tag{B.1}$$

Following *deBlank* [2006], this can be broken down into components:

$$m\dot{v}_{\|} = F_{\|} \tag{B.2}$$

$$m\dot{\mathbf{v}}_{\perp} = \mathbf{F}_{\perp} + q\mathbf{v}_{\perp} \times \mathbf{B}. \tag{B.3}$$

Because the parallel component is affected only by the general force it can be ignored. The cross product in the perpendicular component involves only $\mathbf{v}_{\perp}$ because $\mathbf{v} = \mathbf{v}_{\|} + \mathbf{v}_{\perp}$ and $\mathbf{v}_{\|} \times \mathbf{B} = 0$. It is possible to further break down the perpendicular velocity as

$$\mathbf{v}_{\perp} = \mathbf{v}_d + \mathbf{v}_{gyr}, \tag{B.4}$$

where $\mathbf{v}_d$ is the drift velocity and $\mathbf{v}_{gyr}$ is the gyration velocity. In a frame moving with the drift velocity, only $\mathbf{v}_{gyr}$. is present. The equation of motion in the drifting frame is

$$m\dot{\mathbf{v}}_d = q\mathbf{v}_d \times \mathbf{B} \tag{B.5}$$

$$m\frac{d}{dt}(\mathbf{v}_{\perp} - \mathbf{v}_d) = q(\mathbf{v}_{\perp} - \mathbf{v}_d) \times \mathbf{B}, \tag{B.6}$$

and when this is combined with equation B.3 the result is

$$\mathbf{F}_{\perp} = -q\mathbf{v}_d \times \mathbf{B} + m\dot{\mathbf{v}}_d. \tag{B.7}$$

If the drift velocity (which is itself an average of a modified gyrating motion) does not vary with time, the last term can be ignored. Taking the cross product with $\mathbf{B}$ of the remaining term on the right hand side results in

$$\begin{aligned} \mathbf{F}_{\perp} \times \mathbf{B} &= q\mathbf{B} \times (\mathbf{v}_d \times \mathbf{B}) \\ &= q\left(\mathbf{v}_d(\mathbf{B} \cdot \mathbf{B}) - \mathbf{B}(\mathbf{B} \cdot \mathbf{v}_d)\right), \end{aligned} \tag{B.8}$$

and the last term is zero because $\mathbf{v}_d \perp \mathbf{B}$. Rearranging and changing back to $\mathbf{F}$ (because of the cross product), the general force drift velocity is

$$\mathbf{v}_d = \frac{\mathbf{F} \times \mathbf{B}}{qB^2}. \tag{B.9}$$

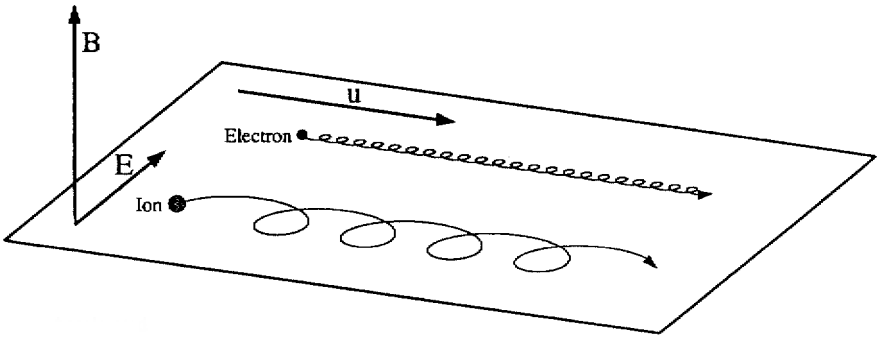

Figure B.1: Drift motion u of a charged particle subject to a magnetic field B and electric field E. From *Kivelson* [1995].

Figure B.1 shows the application of equation B.9 where the force is the Coulomb force, caused by an electric field **E**, so that $\mathbf{F} = q\mathbf{E}$. The resulting drift is the convective drift of equation 2.4, $\mathbf{v}_{cnv} = \mathbf{E} \times \mathbf{B}/B^2$. The force **F** accelerates the particle, which travels on a curved path because of the Lorentz force $\mathbf{F}_L$:

$$\mathbf{F}_L = q\mathbf{v} \times \mathbf{B}, \tag{B.10}$$

where **v** is the velocity of the particle. The curve has a radius of curvature ρ defined by

$$\rho = \frac{mv_\perp}{|q|B}, \tag{B.11}$$

the particle's gyroradius. As the particle accelerates, its radius increases. When the particle turns enough to travel in the opposite direction to the force **F**, it decelerates and its radius decreases. The particle stops (or turns farther) and begins to accelerate in the direction of **F** once again, and its radius increases. From this cyclical motion a net velocity arises that is perpendicular to both **F** and **B**.

B.2 The Curvature–Gradient Drift and the Ring Current

Non-uniform magnetic fields lead to other drift-producing forces, and can be expressed in terms of the curvature and gradient of the magnetic field. These are the forces responsible for the ring current that flows westward around the Earth at equatorial latitudes, approximately between one and six Earth radii [*Wolf*, 1995].

B.2.1 The Curvature Drift

The curvature drift has a straightforward derivation using equation B.9. A particle travelling along a curved magnetic field with parallel velocity $\mathbf{v}_\parallel$ will be subject to the centripetal force $\mathbf{F}_{curv}$, which depends on the radius of curvature ρ and is in the radial direction $\hat{\mathbf{r}}$:

$$\mathbf{F}_{curv} = \frac{mv_\parallel^2}{\rho}\hat{\mathbf{r}}. \tag{B.12}$$

The curvature vector $\vec{\kappa}$ points in the direction of curving and is given by

$$\vec{\kappa} = \frac{-\hat{\mathbf{r}}}{\rho}. \tag{B.13}$$

Substituting $\mathbf{F}_{curv}$ into equation B.9 and noting that

$$mv_{\parallel}^2 = 2W_{\parallel}, \tag{B.14}$$

for the parallel kinetic energy $W_{\parallel}$, gives the curvature drift:

$$\mathbf{v}_{\text{crv}} = \frac{2W_{\parallel}}{qB^2}\mathbf{B} \times \vec{\kappa}. \tag{B.15}$$

B.2.2 The Gradient Drift

Again following *deBlank* [2006], the gradient drift can be found from the force acting on a magnetic dipole in a magnetic field gradient. The magnetic moment μ of the dipole is

$$\mu = \frac{W_{\perp}}{B}, \tag{B.16}$$

where $W_{\perp}$ is the perpendicular kinetic energy, and the force $\mathbf{F}$ on the dipole is

$$\mathbf{F} = -\mu \nabla B, \tag{B.17}$$

meaning that from equation B.9, the gradient drift $\mathbf{v}_{\text{grd}}$ is

$$\mathbf{v}_{\text{grd}} = \frac{W_{\perp}}{qB^3}\mathbf{B} \times \nabla B. \tag{B.18}$$

B.2.3 Mapping of the Curvature–Gradient Drift

It is notable that the effects of the curvature–gradient drift do not extend significantly beyond 50° MLAT in either direction.

The quasi-dipolar magnetic field $\mathbf{B}$ of the Earth can be approximated as a dipolar field $\mathbf{B}_{dip}$ given by

$$\mathbf{B}_{dip} = \frac{B_{eq,s}R_E^3}{r^3}\left(-2\sin\Lambda\hat{\mathbf{r}} + \cos\Lambda\hat{\Lambda}\right), \tag{B.19}$$

where $B_{eq,s} = 0.310 \times 10^{-4}$ T is the magnetic field at the equator at the Earth's surface, $R_E = 6371$ km is the radius of the Earth, and $\mathbf{r}$ is the radial vector and Λ is the latitude along with their associated unit vectors, $\hat{\mathbf{r}}$ and $\hat{\Lambda}$ respectively. Substituting this dipolar magnetic field into the gradient drift equation (B.18) and curvature drift equation (B.15), it can be shown that the combined curvature and gradient drift varies with Λ as:

$$\frac{\cos^5\Lambda\left(1+\sin^2\Lambda\right)}{\left(1+3\sin^2\Lambda\right)^2}, \tag{B.20}$$

which drops off rapidly away from the equator so that above 50° magnetic latitude the curvature–gradient drift is negligible.

The high-latitude geomagnetic field is not affected by the curvature and gradient drifts, so its dynamics can be interpreted as being driven only by the convective drift. Because the high-latitude field is also the part of the geomagnetic field involved in magnetospheric dynamics, the magnetospheric effects on the ionosphere are clearly seen in the measured convective drift.

B.2.4 The Ring Current

Magnetospheric plasma particles that are frozen into the Earth's magnetic field are still subject to large parallel (field-aligned) conductivity, and so may move parallel to the magnetic field with comparative ease. The particles maintain their gyration during this parallel, meridional motion. Because of the quasi-dipolar shape of the geomagnetic field, as a particle travels along the field toward higher latitudes its distance from the Earth decreases, and the geomagnetic field strength B increases according to

$$B = \frac{B_{eq,s} R_E^3}{r^3} \sqrt{3 \sin^2 \Lambda + 1}, \tag{B.21}$$

where $B_{eq,s} = 0.310 \times 10^{-4}$ T is the geomagnetic field strength at the surface of the Earth at the equator, $R_E = 6371$ km is the radius of the Earth, r is the radius from the centre of the Earth, and Λ is the latitude. If the field strength varies slowly compared to the gyroperiod of the particle, the particle's magnetic moment μ, given by

$$\mu = \frac{W_\perp}{B}, \tag{B.22}$$

is constant, so the perpendicular energy must also increase. Energy being conserved, the parallel kinetic energy of the particle is transferred to the perpendicular kinetic energy of its gyration. At a certain altitude only perpendicular energy will remain. At that so-called mirror point, the particle is "reflected" and begins to travel in the opposite direction along the field.

Within a few Earth radii of the Earth's surface the geomagnetic field is quasi-dipolar and the effects of the curvature and gradient drifts can be seen on particles travelling back and forth between their mirror points in the northern and southern hemispheres. Because of the charge dependence of both curvature and gradient drift, ions and electrons drift in opposite directions and a westward current is set up perpendicular to the geomagnetic field. The current established by the curvature and gradient drifts circles the entire globe and is called the ring current. It is shown in Figure 1.1.

B.3 The Convection–Diffusion Equation

The equations governing frozen-in flow in a plasma arise from Ohm's law, which can be written

$$\mathbf{J} = \sigma \left(\mathbf{E} + \mathbf{v} \times \mathbf{B} \right), \tag{B.23}$$

where $\mathbf{J}$ is the current density, σ is the conductivity, $\mathbf{E}$ is the electric field, $\mathbf{B}$ is the magnetic field, and $\mathbf{v}$ is the velocity of the plasma. Ampère's law is

$$\nabla \times \mathbf{B} = \mu_0 \mathbf{J} + \mu_0 \varepsilon_0 \frac{\partial \mathbf{E}}{\partial t}, \tag{B.24}$$

where t is time and ε_0 and μ_0 are the permittivity and permeability of free space, respectively. Under steady-state conditions in the solar wind, the final term can be neglected. Rearranging and taking the curl of equation B.24 gives

$$\nabla \times \mathbf{J} = \frac{1}{\mu_0} \nabla \times (\nabla \times \mathbf{B}) = \frac{1}{\mu_0} \left(\nabla (\nabla \cdot \mathbf{B}) - \nabla^2 \mathbf{B} \right), \tag{B.25}$$

which can be simplified by noting Gauss's law for magnetism:

$$\nabla \cdot \mathbf{B} = 0. \tag{B.26}$$

Meanwhile, taking the curl of equation B.23 gives

$$\nabla \times \mathbf{J} = \sigma \left(\nabla \times \mathbf{E} + \nabla \times (\mathbf{v} \times \mathbf{B}) \right), \tag{B.27}$$

which can be simplified itself with Faraday's law:

$$\nabla \times \mathbf{E} = -\frac{\partial \mathbf{B}}{\partial t}. \tag{B.28}$$

The two simplified expressions for the curl of current density can then be combined and rearranged to give

$$\frac{\partial \mathbf{B}}{\partial t} = \nabla \times (\mathbf{v} \times \mathbf{B}) + \frac{1}{\mu_0 \sigma} \nabla^2 \mathbf{B}, \tag{B.29}$$

Because $\sigma \to \infty$ in the collisionless plasma of the solar wind, the final term of equation B.29 (representing diffusion) is negligible and

$$\frac{\partial \mathbf{B}}{\partial t} = \nabla \times (\mathbf{v} \times \mathbf{B}). \tag{B.30}$$

Changing the left-hand side back to $-\nabla \times \mathbf{E}$ by way of equation B.28 results in the equation describing frozen-in flux:

$$\mathbf{E} = -\mathbf{v} \times \mathbf{B}. \tag{B.31}$$

B.4 Frozen-In Flow

Consider a flux tube, an imaginary volume created by propagating a surface parallel to the magnetic field in a magnetised plasma, as shown in Figure B.2. The surface shown began at time t at the left end of the figure and moved at velocity $\mathbf{v}$, along with the plasma, to the right end of the figure by time $t + dt$. Following *Siscoe* [1983], the flux Φ through the surface changes with time as

$$\frac{d\Phi}{dt} = \oint d\mathbf{a} \cdot \frac{d\mathbf{B}}{dt} + \oint \mathbf{B} \cdot (\mathbf{v} \times d\mathbf{l}). \tag{B.32}$$

The first term represents a change in flux due to a change in the magnetic field and uses infinitesimal area vector $d\mathbf{a}$. The second term represents a change in flux due to the movement of the surface. The grey stripe along the side of the flux tube in Figure B.2 has length $v\,dt$ and width dl, so its area has magnitude $v\,dt\,dl$ and can be represented as an outward-pointing vector $d\mathbf{A}$ defined by

$$d\mathbf{A} = \mathbf{v} dt \times d\mathbf{l}. \tag{B.33}$$

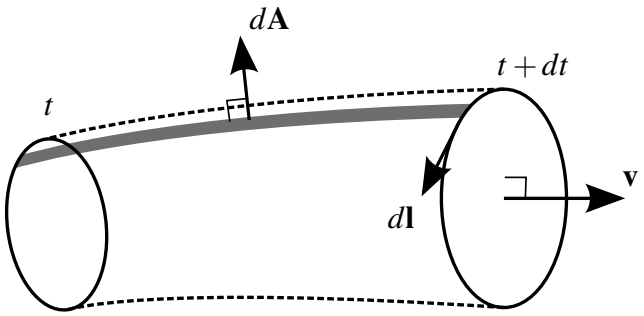

Figure B.2: A plasma flux tube. The cross-sectional surface shown as a solid oval has propagated at velocity **v**, along with the plasma, beginning at time t and ending at time $t+dt$ after an infinitesimal time dt. The "walls" of the flux tube are shown with dashed lines. The $d\mathbf{l}$ vector shows an infinitesimal length element for integration around the boundary of the surface. For simplicity **v** is shown as normal to the surface. The grey stripe shows the infinitesimal area $d\mathbf{A}$ along the side of the flux tube. After *Siscoe* [1983].

Integrating the magnetic flux through the infinitesimal area $d\mathbf{A}$ over the outer "wall" of the flux tube gives the flux added by the surface's motion in the time dt in the form of a path integral over the boundary of the surface:

$$\int \mathbf{B}\cdot d\mathbf{A} = dt \oint \mathbf{B}\cdot(\mathbf{v}\times d\mathbf{l})\,. \tag{B.34}$$

Removing the time factor, the second term of equation B.32 is obtained.

Using vector identities, the triple product in the second term can be rearranged:

$$\mathbf{B}\cdot(\mathbf{v}\times d\mathbf{l}) = d\mathbf{l}\cdot(\mathbf{B}\times\mathbf{v}) = -d\mathbf{l}\cdot(\mathbf{v}\times\mathbf{B})\,. \tag{B.35}$$

Using Stokes' theorem, the path integral over the boundary of the surface in the second term can be converted to an area integral over the surface:

$$-\oint d\mathbf{l}\cdot(\mathbf{v}\times\mathbf{B}) = -\int d\mathbf{a}\cdot\nabla\times(\mathbf{v}\times\mathbf{B})\,. \tag{B.36}$$

Then equation B.32 can be rewritten as

$$\frac{d\Phi}{dt} = \oint d\mathbf{a}\cdot\left(\frac{d\mathbf{B}}{dt} - \nabla\times(\mathbf{v}\times\mathbf{B})\right). \tag{B.37}$$

From equation B.30, the difference inside the integral must be zero. Therefore, the flux through the surface does not change, regardless of changes in the magnetic field or in the boundary of the surface.